STRESS DRIVEN PHYSIOLOGICAL DAMAGE AFTER TRAUMATIC BRAIN INJURIES

Submitted in partial fulfillment of the requirements
of the degree of
Doctor of Philosophy
of the
Indian Institute of Technology Bombay, India
and
Monash University, Australia
by

AAYUSH KANT

Supervisors:
Prof. Tanmay K. Bhandakkar (IIT Bombay)
Prof. Nikhil V. Medhekar (Monash University)

The course of study for this award was developed jointly by
Monash University, Australia and the Indian Institute of Technology Bombay, India
and was given academic recognition by each of them.
The programme was administrated by The IITB-Monash Research Academy

November 2019

DON'T PANIC

DECLARATION

I declare that this written submission represents my ideas in my own words and where others' ideas or words have been included, I have adequately cited and referenced the original sources. I also declare that I have adhered to all principles of academic honesty and integrity and have not misrepresented or fabricated or falsified any idea/data/fact/source in my submission. I understand that any violation of the above will be cause for disciplinary action by the Institute and can also evoke penal action from the sources which have thus not been properly cited or from whom proper permission has not been taken when needed.

Date: November 15, 2019 **Aayush Kant**

ACKNOWLEDGEMENT

At the outset, I am extremely grateful to my supervisors, Prof Tanmay K Bhandakkar at IIT Bombay and Prof Nikhil Medhekar at Monash University. Their patience, ever present support and confidence in me is what has propelled me to this point. They have led me through the process of scientific inquiry. Their tutelage enabled me to understand the interdisciplinary nature of my research. Conversations with them throughout the course of my PhD have been a source of intellectual nourishment for which I am eternally thankful.

The thesis has shaped up because of the continued feedback from my research progress committee members Prof M. P. Gururajan from IIT Bombay and Prof Laurence Brassart from Monash University. The efforts taken by them to evaluate my research annually has undoubtedly helped to calibrate my progress. I am also very thankful for the inputs given by Prof John Forsythe and Prof Laurence Meagher from Monash University which helped lay a foundation for the research questions explored. I am obliged to my thesis reviewers Prof Namrata Gundiah and Prof Ricardo Ruiz Baier whose comments have helped in a giving fruitful finishing touch to the text.

I am grateful to the IITB-Monash research academy for giving me an opportunity to pursue a PhD jointly across two continents at IIT Bombay and Monash University. I cannot appreciate enough the invaluable learning experiences gained. I am grateful to Dr Murali Sastry, CEO of our academy, for taking out time for me on innumerable occasions for pertinent academic advice. Many thanks to the academic and administrative support from Mrs. Beena Pillai, Mrs. Nancy Sowho, Mrs. Laya Vijayan, Mrs. Jayashree T, and Mr Kiran More. Their cheerful and unconditional help kept the joy alive through the otherwise mundane administrative procedures.

My sincerest and warmest gratitude to the friends I made during this course. The camaraderie, banter and vacations with Ashwin and Pratik have been a constant source of escapades. Unforgettable they are! I am indebted to Gaurav, Nipal, Sagar and Dinesh for gladly being an ever present support and a source of stimulating discussions and joy in the lab. There was never a dull moment with them around.

Lastly, back at home, I am grateful to my parents for getting me this far. Immeasurable thanks are due to Ashika for her patience, kindness, and endless and selfless support through the highs and the trying times during the thesis preparation. I am fortunate to have her by my side.

Abstract

Development of predictive capability to model physiological damage owing to the biochemical disturbances involved in the secondary insult phase of a traumatic brain injury constitutes an important step in its prevention and clinical treatment. Initiated by an accumulation of excess intracellular calcium, secondary insults in the axonal region of the neuron are associated with a disruption of microtubule assembly due to dysfunction of tubulin binding tau proteins. We first present a stress history dependent non spatial kinetic model to predict the microscale phenomena of secondary insults due to accumulation of excess calcium ions (Ca^{2+}) induced by the macroscale primary injuries. The model is able to capture the experimentally observed increase and subsequent partial recovery of intracellular Ca^{2+} concentration in response to various types of mechanical impulses. By considering the brain tissue as a solid continuum with the Ca^{2+} activity occurring at every material point we spatialise our model. The spatial calcium kinetics model faithfully captures the experimental observations concerning the Ca^{2+} concentration, load rate, magnitude and duration and most importantly shows that the critical location for primary injury may not be the most important location as far as secondary injury is concerned. Finally, we focus on the secondary insult in the axonal region of neuron in the form of disruption of microtubule assembly due to dysfunction of tubulin binding tau proteins. Specifically we propose a non-spatial kinetics model to predict phosphorylation of tau proteins because of calpain enzyme mediated activation of the intracellular kinase which in turn is caused by excess intracellular calcium ion accumulation catalyzed by external mechanical stress. We demonstrate the accuracy and validity of our model by comparing our predictions with the available clinical and experimental observations from literature.

Chapter 2 of the thesis has been published in the journal ”Biomechanics and Modeling in Mechanobiology”. Chapter 3 and 4 are being prepared for submission in appropriate journals.

Contents

1 Introduction **1**

1.1 Traumatic Brain Injury 1

1.2 Calcium Kinetics in Neurons 3

1.3 Neurochemical Origin of Secondary Insults 5

1.4 Numerical Modelling 11

1.5 Motivation 14

2 Non-Spatial Calcium Kinetics **17**

2.1 Compartmental Model 17

2.2 Linear Stability Analysis 19

2.3 Incorporating Mechanical Stress 20

2.4 Results and Discussion 23

2.4.1 Constant Mechanical Loading 23

2.4.2 Impulse Loads 24

2.4.3 Repeated Impulses 31

2.5 Conclusion 33

3 Applying a Continuum Treatment **35**

3.1 Continuum Framework Based Spatialization 35

3.2 Results and Discussion 37

3.2.1 Analytical Solution 37

3.2.2 Uniaxial Pressure Impulse – Geometry Effects 40

3.2.3 Uniaxial Pressure Impulse – Impulse Effects 43

3.2.4 Equibiaxial Pressure Impulse 47

3.2.5 Kinematic loading 50

3.2.6 2D Brain Geometry 54
3.3 Conclusion 59

4 Stress Dependent Tau Phosphorylation 61
4.1 Calpain-I Activation 61
4.2 Calpain Mediated Kinase Truncation 62
4.3 Tau Phosphorylation/Dephosphorylation 64
4.4 Estimation of parameters 66
4.5 Results And Discussion 72
4.5.1 Homeostatic Behavior 72
4.5.2 Behavior Under Mechanical Loading 73
4.5.3 Effects of PP2A Dephosphorylation 78
4.5.4 A Speculative Interpretation for Future Scope 79
4.6 Conclusion 81

5 Summary and Future Plans 83
5.1 Summary 83
5.2 Future Scope 87

Appendices 89

A System Under Homeostasis 91
A.1 Linear Stability 91
A.2 Initial Value Problem 92

B System Under Presence of External Loads 95

C Analytical Solution for 1D Uniaxial Constant Load 97

D Parametric Analysis 101

Bibliography 105

List of Figures

1.1 A schematic of ion transport pathways inside a neuron. 4
1.2 Schematic of tau hyperphosphorylation 8
1.3 Secondary injury pathways leading to microtubule rupture. 12

2.1 Intracellular concentration evolution under homeostasis after initial perturbation 21
2.2 Intracellular concentration evolution under constant stress measure $\hat{s}$ . . . 23
2.3 Intracellular concentration evolution under various impulse loads 25
2.4 Calibration of calcium kinetics model 27
2.5 A comparison of the predicted intracellular concentration evolution with experiments 28
2.6 Variation of peak intracellular concentration with magnitude and duration of impulse 29
2.7 Effect of loading rate on calcium evolution 30
2.8 Intracellular concentration evolution under repeated impulse loading . . . 31
2.9 Variation in the intracellular concentration due to varying time interval between repeated impulses 33

3.1 Uniaxial extension of 1D tissue 37
3.2 Normalised stress evolution in 1D tissue for constant load 39
3.3 Normalised stress evolution in 1D tissue for impulse load 42
3.4 Evolution of stress and Ca^{2+} concentration in 1D tissue for impulse load . 43
3.5 Variation of peak and residual Ca^{2+} concentration with impulse magnitude or duration 45
3.6 Typical ramped impulses to study the effect of load rate 46

3.7 Variation of peak and residual Ca^{2+} concentration with ramping duration of impulse 47
3.8 Evolution of stress and Ca^{2+} concentration in 2D tissues of varying dimensions for equibiaxial impulse load 49
3.9 Evolution of stress and Ca^{2+} concentration for kinematic loading 51
3.10 Development of a 2D brain geometry 56
3.11 Evolution of stress and Ca^{2+} concentration in a 2D brain under kinematic loading 58

4.1 Estimation of kinetic parameters 72
4.2 Kinase truncation and Tau phosphorylation under repeated impulse load . 74
4.3 PP2A activity reduction effects on tau phosphorylation 78

C.1 Uniaxial extension of 1D tissue 97

D.1 Variation in the tau phosphorylation levels $\mathcal{N}$ as each of the parameter is varied by ±30%. 102
D.2 Evolution of secondary insult output parameters under various cases of kinematic loads 103
D.3 Variation in the peak Ca^{2+} levels c_i^{peak} as each of the parameter is varied by ±30%. 104

List of Tables

2.1 Value of Ca^{2+} Kinetics Parameters 19

3.1 Material Properties of Brain Tissue 37
3.2 Peak stress and Ca^{2+} concentrations in a 1D tissue of varying lengths under impulse load 41
3.3 Peak stress and Ca^{2+} concentration under varying kinematic loading parameters 52

4.1 Value of Parameters 67
4.2 Value of kinematic parameters for the applied impulse 75
4.3 Calpain Activation and Tau phosphorylation at points of interest 76

Chapter 1

Introduction

1.1 Traumatic Brain Injury

Traumatic Brain Injury (TBI) is defined as an impact, penetration or rapid movement of the brain within the skull that results in an altered mental state (Prins *et al.*, 2013). TBIs are one of the most commonly occurring injuries to the human brain. In the USA, around 5.3 million people are living with a TBI-related disability, while in the European Union, the number is approximately 7.7 million (Roozenbeek *et al.*, 2013). TBI can be fatal and accounts for 30.5% of all injury related deaths in USA (Faul *et al.*, 2010). The availability of statistics in India is comparatively less. An epidemiological study, during 2007-09, set in a rural district of Wardha, in Maharashtra, India, with a population of approximately 1.2 million, shows that 1,926 patients were admitted to the district's neurosurgery service, diagnosed with TBI. Motor vehicle accidents account for 46.8% of these cases. Out of all the patients admitted, 58% were diagnosed with mild, 21.5% moderate and 15% severe cases of TBI. In all, 123 patients either did not survive or endured a persistent vegetative state (Agrawal *et al.*, 2012). A study performed in the urban setting of Bangalore, noted at least 1.6 million TBI incidences, of which 200,000 are fatal. Different studies attribute traffic accidents to cause around 45-–60% of all TBI incidences. 70% of TBIs were mild, 14% moderate and 16% severe. Of severe TBI 38% were fatal, while only 1.5% of mild TBI resulted in mortality. More than 50% of the patients discharged after treatment continued to have post traumatic sequelae and disabilities of varying types and severity (Gururaj, 2013). A study in Australia and New Zealand, performed over a period of one year, 2000-01, classified 24.7% of studied TBIs as mild, 18.1% as moderate and 57.2%

as severe. 61.4% of TBIs were caused by motor accidents, 24.9% due to falls, especially in elderly patients, 8% due to interpersonal violence and 0.8% due to gunshot wounds (Myburgh *et al.*, 2008).

The cerebral pathophysiology of a TBI is extremely complex due to a large number of physical and neurochemical changes that are involved (Nilsson *et al.*, 1993; Giza and Hovda, 2001; Weber, 2012). Any TBI has two main stages, a primary insult, which is a mechanical damage that occurs at the time of impact, and secondary insults, which comprise a series of neurochemical responses to the initial insult, often occurring at a much delayed stage (Werner and Engelhard, 2007). It takes around 2 to 8 minutes for the neurochemical changes accompanying TBI to set in (Williams *et al.*, 2014). The chemical reactions which follow have corresponding physiological effects which begin around 30 minutes after the occurrence of the injury. These may continue to occur for days (Gaetz, 2004).

A TBI may occur due to either a sudden acceleration or deceleration of the head, or due to a high velocity impact, which in turn induces linear and rotational acceleration on the brain tissue within the skull, resulting in development of high pressure gradients and mechanical stresses (Meaney and Smith, 2011; Namjoshi *et al.*, 2013). In case of impact to brain, the rate of application of force determines the extent of injury while the location of impact, called the coup site and its diametrically opposite location, called the contre-coup site, are identified as susceptible regions for injury (Smith and Meaney, 2000; Meaney and Smith, 2011). Such impacts to the head result in focal brain injuries, which are localized in nature (Smith and Meaney, 2000). Contusions, which occur in the gray matter nearest to the brain surface, are an example of a focal brain injury (Zink, 2001). On the other hand, inertial loading which occurs due to sudden acceleration or deceleration, produces diffused brain injuries, which occur in the deeper white matter of the brain over a relatively larger area. Concussions are a mild form of diffused injuries (Smith and Meaney, 2000; Zink, 2001). Mild TBIs commonly exhibit a pathological feature called diffuse axonal injury (DAI), the severity of which has been clinically correlated to the extent of disability following the injury (Smith and Meaney, 2000; Browne *et al.*, 2011; Tang-Schomer *et al.*, 2012; Blennow *et al.*, 2016). DAI are commonly characterized by a damage to the neuronal cytoskeletal structure, which comprises of neurofilament (NF) proteins and axonal microtubules (MT), resulting in disrupted axonal transport mechanism (Smith and Meaney, 2000; Tang-Schomer *et al.*, 2012; Blennow *et al.*, 2016). The

NF network contributes to the axon tensile strength (Hill *et al.*, 2016). Post TBI, a reduced interfilament spacing is seen in the NF network, termed as NF compaction, due to its posttransational modifications such as phosphorylation and glycosylation (Siedler *et al.*, 2014; Hill *et al.*, 2016). MTs are elongated polymers forming a fast transport conduit along the length of the axon. They are assembled into a stabilized bundle formation via a cross linking done by microtubule-associated protein (MAP) tau (Dehmelt and Halpain, 2005; Peter and Mofrad, 2012). A mechanical failure in the microtubules under a dynamic tensile stretch is observed in-vitro (Tang-Schomer *et al.*, 2010, 2012). It is hypothesized that a brittle failure of the cross linking tau proteins may result in loss of the MT bundle integrity (Peter and Mofrad, 2012; Ahmadzadeh *et al.*, 2014, 2015). In conjunction with such primary damage of mechanical nature, secondary insults involving a calcium ion (Ca^{2+}) influx mediated modifications of the cytoskeletal proteins post TBI are also known to debilitate the structural and functional integrity of the axons (Smith and Meaney, 2000; Siedler *et al.*, 2014; Hill *et al.*, 2016).

1.2 Calcium Kinetics in Neurons

The physiological state and the functions of neurons are governed by the intracellular calcium ion (Ca^{2+}) concentration (Berridge *et al.*, 2003; Wojda *et al.*, 2008). To offer increased sensitivity of the functional responses to changes in Ca^{2+} concentration, the background concentration of Ca^{2+} must be maintained at a very low level (Brini *et al.*, 2014). All the cells, including neurons, can regulate their intracellular Ca^{2+} concentration at a stable level through a mechanism called homeostasis. The intracellular Ca^{2+} concentration is reported to be approximately $1 \times 10^{-4}\,mM$, and is almost four orders of magnitude lower than the typical extracellular Ca^{2+} concentration (Kowalewski *et al.*, 2006; Kilinc, 2008; Gleichmann and Mattson, 2011; Brini *et al.*, 2014). The intracellular concentration changes due to an influx of Ca^{2+} ions from outside the cell which may occur through various channels present in the plasma membrane (PM) as shown in Fig. 1.1. One of the most prominent among these is the N-methyl-D-aspartate (NMDA) receptor pathway. The NMDA receptors are conventionally considered as glutamate-gated cation channels with a high calcium permeability (Blanke and VanDongen, 2009). New evidence (Maneshi *et al.*, 2017) however suggests that glutamate may not activate the NMDA gating mechanisms — the stress dependent activation of these channels may be attributed to

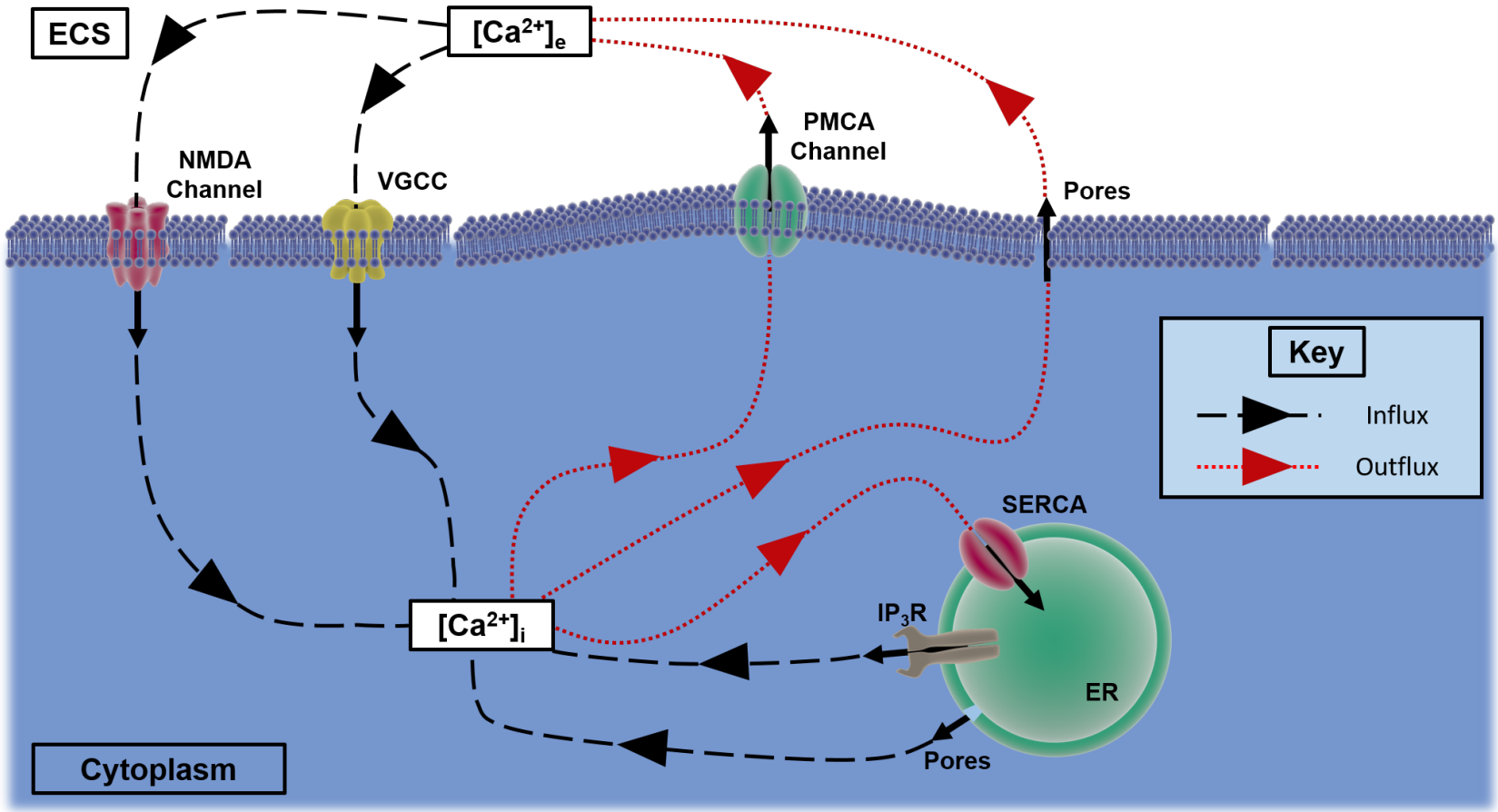

Figure 1.1: A schematic of ion transport pathways inside a neuron. Only a few important pathways are shown for representative purpose. The pathways in black dashed lines (red dotted lines) increase (decrease) the intracellular concentration of Ca^{2+} ions.

cytoskeletal coupling or direct stretch activation due to bilayer tension (Kloda *et al.*, 2007; Maneshi *et al.*, 2017). Irrespective of the activating agents, the activation of NMDA receptors results in the opening of associated Receptor Operated Channels (ROCs) in the cell membranes allowing the entry of Ca^{2+} into the cell (Zink, 2001; Weber, 2012). Resulting ionic imbalances open other channels especially the Voltage-Gated Calcium Channels (VGCCs), which further increase influx of the calcium ions (Weber, 2012). Mechanisms which compensate for the increase in intracellular Ca^{2+} concentration by expelling the excess ions from the cytoplasm, involve active pumps present in the PM such as the plasma membrane Ca^{2+}-ATPases (PMCA), or ion exchanging channels such as the Na^{2+}/Ca^{2+} exchanger (Kristián and Siesjö, 1998; Berridge *et al.*, 2003; Weber, 2012). Inward or outward movement of Ca^{2+} can also happen through pores in PM as shown in Fig. 1.1 (Farkas *et al.*, 2006; Kowalewski *et al.*, 2006; Kilinc, 2008; Williams *et al.*, 2014). Thus the influx of ions through channels and pores is dynamically balanced by outflux through the PMCA.

In addition to the transport across the PM, an exchange of ions also occurs between the cytoplasm and the intracellular organelles like the endoplasmic reticulum (ER) through channels, pumps and leak through pores (Berridge *et al.*, 2003; Kowalewski *et al.*, 2006; Wojda *et al.*, 2008; Weber, 2012). The inositol 1,4,5-triphosphate receptors (IP3-R) and ryanodine receptors (RyR) are examples of channels that move the calcium ions from inside of the ER to the cytoplasm. Since the Ca^{2+} concentration is higher inside the ER than in the cytoplasm, the pores in the ER membrane also transport ions into the cytoplasm (Baker *et al.*, 2002; Kowalewski *et al.*, 2006). Sarcoplasmic and endoplasmic reticulum Ca^{2+} ATPase, or SERCA, is a pump that tries to balance the outflow by pumping ions back into the ER from the cytoplasm (Berridge *et al.*, 2003; Falcke, 2004; Wojda *et al.*, 2008; Weber, 2012). There are various other mechanisms that allow the transport of Ca^{2+} across the plasma membrane including second-messenger-operated channels (SMOCs), store-operated channels (SOCs) and stretch operated channels (Berridge *et al.*, 2003; Brini *et al.*, 2014)

1.3 Neurochemical Origin of Secondary Insults

Various components of Ca^{2+} homeostasis mechanism, as shown in figure 1.1 and their contributions are drastically affected in a neuron during a TBI Wojda *et al.* (2008). As a

first step of secondary insult due to TBI a massive amount of glutamate is released in the extracellular space (ECS) of the brain following the mechanical damage (Palmer *et al.*, 1994; Zink, 2001; Weber, 2004). Activation of the NMDA receptors due to presence of glutamate results in the opening of other channels such as ROCs and VGCCs in the cell membranes thereby allowing entry of the calcium ions (Ca^{2+}) into the cell (Zink, 2001; Weber, 2012). In addition, the presence of excess calcium inside the cell results in a loss of functionality, thus limiting the availability of ATP which is required for the PMCA and SERCA pumps (Weber, 2012). Consequently the PMCA and SERCA activities are also reduced, thereby reducing the rate of removal of Ca^{2+} from the cell. In vitro experiments have examined the effects of external mechanical loads on the neuronal behaviour (Rzigalinski *et al.*, 1997, 1998; Geddes and Cargill, 2001; Lusardi *et al.*, 2004). These studies report an immediate elevation of intracellular Ca^{2+}, followed by a gradual recovery. These investigations have attempted to identify the relative importance of various Ca^{2+} transport mechanisms, thereby trying to establish the exact mechanical etiology involved in a TBI. Further, an additional mechanism through which local stress may change the influx of Ca^{2+} is mechanoporation, wherein presence of stress results in either direct or indirect increase of PM permeability (Farkas *et al.*, 2006; Kilinc, 2008). These disturbances in the homeostatic calcium transport mechanisms result in an over-accumulation of Ca^{2+} inside the neurons (reviewed in (Wojda *et al.*, 2008; Weber, 2012; Prins *et al.*, 2013; Siedler *et al.*, 2014)). High levels of intracellular Ca^{2+} initiate a multitude of neurochemical reactions which result in production of free radicals, mitochondrial overload and disruption of essential cellular functions like glucose metabolism (Zink, 2001; Weber, 2012; Prins *et al.*, 2013; Hill *et al.*, 2017). Intracellular Ca^{2+} also activates various degenerative proteases which act on readily available protein substrates throughout the neuron, compromising its structural and/or functional integrity, leading to fatal downstream effects.

Calpain is a family of cysteine proteases activated by Ca^{2+}. Of the various known members of calpain family, calpain-I and calpain-II are ubiquitously present in human and animal tissues (Goll *et al.*, 2003; Ono and Sorimachi, 2012; Curcio *et al.*, 2016). Calpain-I, which is more abundant in neurons, typically requires $3 - 50$ μM Ca^{2+} concentration for half-maximal activity and hence is also called μ-calpain. Calpain-II, also called m-calpain, on the other hand, is more expressed in glial cells and has a much higher half-maximal activity Ca^{2+} requirement ($0.4 - 0.8$ mM) (Goll *et al.*, 2003). The Ca^{2+} re-

quirement for calpain activation observed through experiments is however much higher than the physiological intracellular Ca^{2+} concentration, indicating a reduced in-vivo Ca^{2+} requirement, the exact reason for which is yet unresolved. It is hypothesised that in response to Ca^{2+} influx, calpain relocates to the cell periphery, where phospholipids present in the plasma membrane (PM) reduce the Ca^{2+} requirement for calpain activation (Goll *et al.*, 2003; Ono and Sorimachi, 2012; Curcio *et al.*, 2016). It is also possible that limited activation of calpain at the locations of higher Ca^{2+} concentration is sufficient for downstream proteolysis of calpain substrates (Ono and Sorimachi, 2012). Notwithstanding the origin of calpain activation, intraneuronal breakdown of structurally and functionally essential proteins mediated by calpain is widely implicated in secondary insult. Calpain-I is known to cleave αII-spectrin, a well characterized cytoskeletal protein of the PM. αII-spectrin breakdown products (SBDP) are used as biomarkers of axonal injuries (Goll *et al.*, 2003; Hill *et al.*, 2016; Kulbe and Hall, 2017). Experimental models of TBI report that calpain-mediated SBDP are observed as early as 15 minutes post-injury, and may continue to increase up to 72 hours later (Büki *et al.*, 1999; Pike *et al.*, 2001; Farkas *et al.*, 2005; Serbest *et al.*, 2007; Hill *et al.*, 2017). Calpain-mediated SBDP usually results in formation of two breakdown products, αII-BDP 150, and αII-BDP 145 indicating a sequential degradation (Glantz *et al.*, 2007; Pineda *et al.*, 2007; Chen *et al.*, 2016). Additionally degradation of βII-spectrin by calpain has also been reported in vitro, thereby resulting in variable pathologies depending on the pathway chosen (Glantz *et al.*, 2007; Kobeissy *et al.*, 2015). While calpain SBDP is hypothesised to coincide with decrease in membrane permeability (Pike *et al.*, 2000), there is a contention in the literature for evidence of a causation (Wolf *et al.*, 2001; Gaetz, 2004; Farkas *et al.*, 2006). Other cytoskeletal components of the PM such as ankyrin, are also proteolyzed by calpain in vitro and possibly in vivo (Harada *et al.*, 1997; Reeves *et al.*, 2010).

Within the axonal cytoskeleton, calpain is involved in the destabilization of MT bundles. The MAP tau proteins which stabilize the MTs into an organised bundle can undergo various forms of posttranslational modifications after a TBI, therefore losing their MT binding capabilities (Baudry and Bi, 2016; Blennow *et al.*, 2016; Corrigan *et al.*, 2017; Kulbe and Hall, 2017). Among these posttranslational modifications, the phosphorylation performed by kinases and dephosphorylation performed by phosphatases are relevant to tau dysfunction. A delicate balance between tau phosphorylation and dephosphorylation is maintained in a normal brain so as to optimise the promotion of MT as-

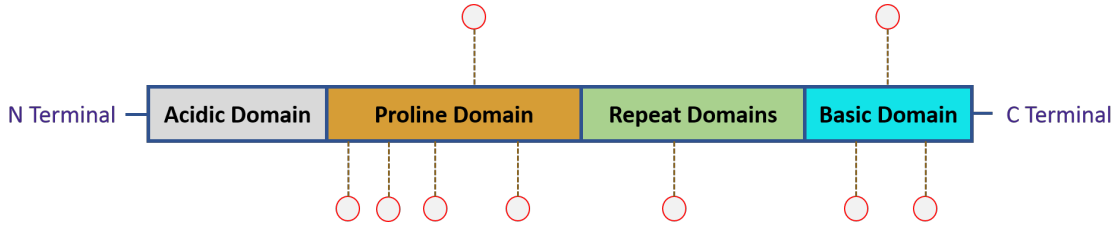

(a)

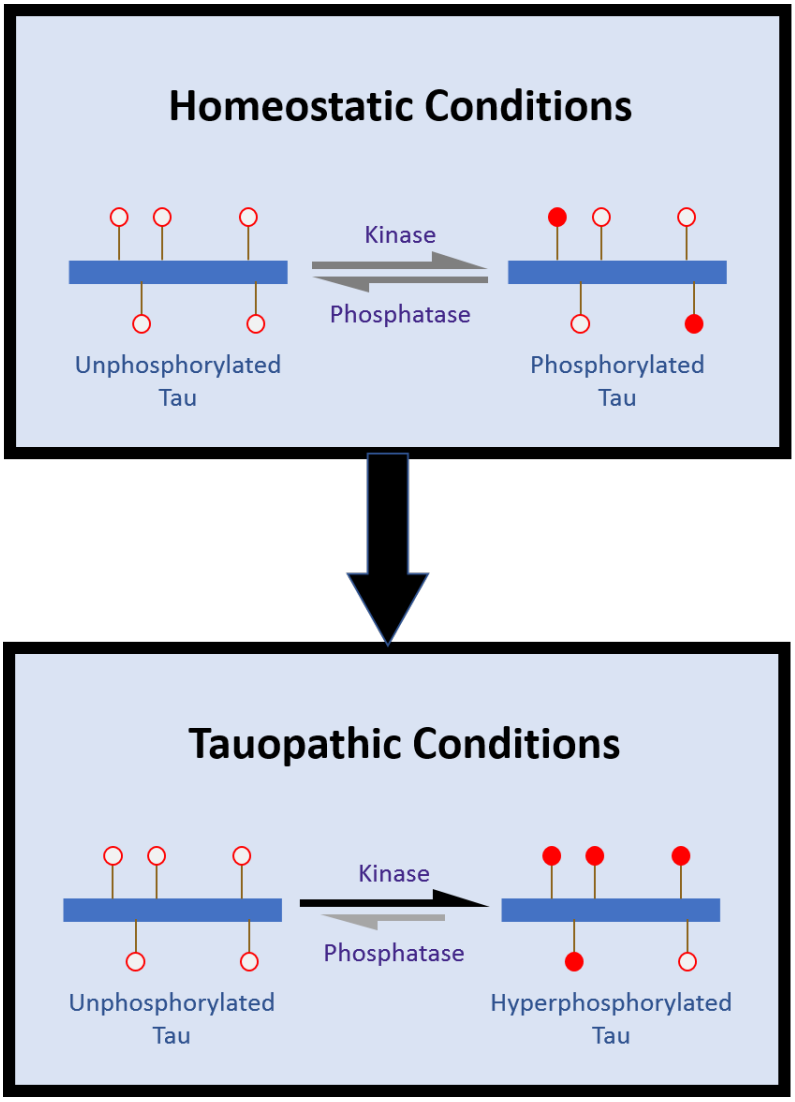

(b)

Figure 1.2: (a) A schematic representation of the structure of tau proteins showing multiple phosphorylation sites. (b) Under homeostatic conditions, the tau phosphorylation carried out by kinases and dephosphorylation carried out by phosphatases balance each other, so as to maintain a constant tau phosphorylation level in the neuron. When a tauopathy occurs the kinase activity increases, while that of the phosphatase may reduce, resulting in hyperphosphorylation of tau proteins.

sembly. Schematic in figure 1.2a shows the structure of the tau protein and the major phosphorylation sites, along with their locations in the different domains of the protein. There are several kinases which phosphorylate tau in-vitro as well as in-vivo. These include glycogen synthase kinase-3β (GSK-3β), cyclin-dependent-like kinase 5 (CDK5), etc. Some kinases like protein kinase A (PKA) are known to prime the tau proteins for further phosphorylation by other kinase. A detailed discussion on the action of calpain on kinase truncation is entailed in Section 4.2. There are several phosphatases which dephosphorylate Tau, though protein phosphatase PP2A alone accounts for $\sim$ 70% of total phosphatase activity (Liu *et al.*, 2006). A calpain mediated disturbance in the signaling pathways cause a phosphorylation/dephosphorylation imbalance, by increasing the kinase activity while simultaneously decreasing the phosphatase activity, resulting in formation of hyperphosphorylated tau (P-Tau). Figure 1.2b shows a schematic representation of such an imbalance occurring due to a tauopathy leading to P-tau formation. P-Tau in such a state is unable to bind to tubulin, thereby losing its ability to promote MT assembly. It has been observed that P-Tau further disrupts the MT assembly by sequestering normal tau from it (Alonso *et al.*, 1996). Sequestered P-Tau nucleate the aggregation of more P-Tau into neurofibrillary tangles (NFT).

NFT are commonly observed in multiple mild TBIs involving concussive or sub concussive impacts sustained over a period of years results in a long term neurodegenerative tau dysfunction called Chronic Traumatic Encephalopathy (CTE). CTE is most often observed amongst contact sport athletes and military veterans because of a high risk of purposeful, repetitive hits to the head (McKee *et al.*, 2009; Blennow *et al.*, 2016). A similar tau protein dysfunction, via its hyperphosphorylation, is characteristically observed in a range of neurodegenerative disorders such as Alzheimers' disease (AD), frontotemporal dementia, etc., together categorized as "tauopathies" (Ferreira and Bigio, 2011; Blennow *et al.*, 2016; Iqbal *et al.*, 2016; Kulbe and Hall, 2017). Repetitive mild TBI presents a major risk for development of CTE and similar neurodegenerative tauopathies such as AD and dementia(Blennow *et al.*, 2016). Tauopathies are characterized by abnormal hyperphosphorylation of tau protiens forming NFT aggregates. A human tau protein has upto 37 phosphorylation sites, though in a normal brain on an average only 2 - 3 moles of phosphates are present per mole of tau (Köpke *et al.*, 1993; Gong *et al.*, 2005; Liu *et al.*, 2006; Iqbal *et al.*, 2009). Hyperphosphorylated tau (P-Tau) in an AD affected brain has 3 - 4 fold more phosphates per mole of tau (Ksiezak-Reding *et al.*, 1992; Iqbal *et al.*,

2009). The role of tau pathology in TBIs are further evidenced by experiments using MT stabilising agents such as Paclitaxel. Use of paclitaxel treatment on mice with controlled cortical impact injuries had an improved neurological outcome (Cross *et al.*, 2015). Another study found short term improvements in neuronal response to administration of MT stabilising agent taxol in vivo (Adlard *et al.*, 2000). In vitro, axons pre-treated with taxol prior to stretch injuries have a better survival as compared to untreated axons (Tang-Schomer *et al.*, 2010). A similar improvement in neurological outcome is seen with use of MT stabilizing agents such as paclitaxel in several tauopathies like AD (Ballatore *et al.*, 2016).

The mechanisms leading to MT disruption following a primary injury, as discussed in this section, are shown in a schematic form in figure 1.3. Tau proteins (shown in red) are schematically shown to bind the microtubule assemblies in an axon. The secondary insults are shown to be initiated due to imbalances in Ca^{2+} homeostasis mechanisms, leading to its over-accumulation. Excess intracellular Ca^{2+} activates calpain which proteolyzes kinases like GSK, and can reduce the activity of phosphatase PP2A. The disturbed kinase-phosphatase activity balance leads to hyperphosphorylation of tau proteins (shown in red), which can no longer bind MT assemblies. As shown in the figure 1.3, hyperphosphorylated tau oligomerize and aggregate, while the MT assembly disintegrates.

In addition to the secondary pathologies discussed in the preceding paragraphs there are numerous other pathways that are known to lead to neuronal dysfunction. Immediately after the primary TBI, the mechanical strain in the glial cells such as microglia and astrocytes results in the synthesis and release of pro-inflammatory cytokines (Weber, 2004). The neurochemical mechanisms for the relationship between mechanical strain and upregulation of cytokines has not been completely explored till date (Lu *et al.*, 2017). The roles played by various cytokines have been elaborately discussed by Woodcock and Morganti-Kossmann (2013). It is hypothesised that the accumulation of immune cells in response to pro-inflammatory agents such as tumour necrosis factor and interleukins, further compounds the brain swelling and decreases the cerebral blood flow. Additionally, the massive calcium influx into the cytosol following trauma results in the mitochondria attempting to sequester the excess Ca^{2+}. The mitochondria are however quickly overwhelmed resulting in mitochondrial pathologies in the form of swellings or membrane fragmentations (Smith and Meaney, 2000). Such pathologies have been observed in vivo after TBI (Maxwell *et al.*, 2003; Lifshitz *et al.*, 2004). Ruptures in the mitochondrial

membranes release apoptotic proteins into the cell (Lifshitz *et al.*, 2004; Hiebert *et al.*, 2015). Damage to mitochondria also results in the formation of reactive oxygen species (ROS), such as superoxide and hydroxide radicals, which in turn damage cellular membrane, mitochondrial membrane, and further can cause breaks in the DNA strand (Weber, 2012). Damage to mitochondria additionally results in metabolism changes which is observed in the form of fall in blood oxygenation, extracellular glucose and rise in extracellular glutamate (Lifshitz *et al.*, 2004; Weber, 2012). These pathologies further exacerbate neuronal necrosis. Severe damage to the neurons can result in a primary axotomy, which in-vitro is seen to be accompanied by axonal retraction (Gallo, 2004). Axonal retraction and many similar cytoskeletal dynamics such as neuronal migration, axonal and dendritic growth, regeneration and synaptic plasticity have in turn been shown to be regulated by Ca^{2+} signaling (Zheng and Poo, 2007; Yamada *et al.*, 2008). Mechanical stretch has been shown to affect the structural arrangement of cytoskeletal members such as actin-myosin network and also microtubules and neurofilaments (Chetta *et al.*, 2010). A review by Hemphill *et al.* (2015) discusses in detail the role of subcellular mechanotransduction in the neuronal microenvironment during a TBI. While such mechanisms have been suggested to play a salient role on the biomechanical evolution of neuronal pathophysiology, we consider it to be beyond the scope of the current work.

1.4 Numerical Modelling

Numerical models have been used to study the distribution of stresses and strains throughout the brain after a TBI. The after-effects of primary insult of TBI at macro-level has been modeled numerically, using detailed three-dimensional (3D) and two-dimensional (2D) finite element (FE) based models of brain (reviewed by (Giudice *et al.*, 2018; Madhukar and Ostoja-Starzewski, 2019)). Some researchers have worked on developing a simplified model including only the major anatomical features, allowing for a quick assessment (Anderson, 2000; Pena *et al.*, 2005; Levchakov *et al.*, 2006). The second approach is development of more detailed 3D model, so as to be able to produce a detailed prediction of local and global response to different loads (Zhang *et al.*, 2001; Mao *et al.*, 2006; Takhounts *et al.*, 2008). The simpler of these models simulate the overall geometry of the brain, without concerning themselves with distinguishing the different regions. On the other hand, the detailed models simulate the geometry and the interactions between the

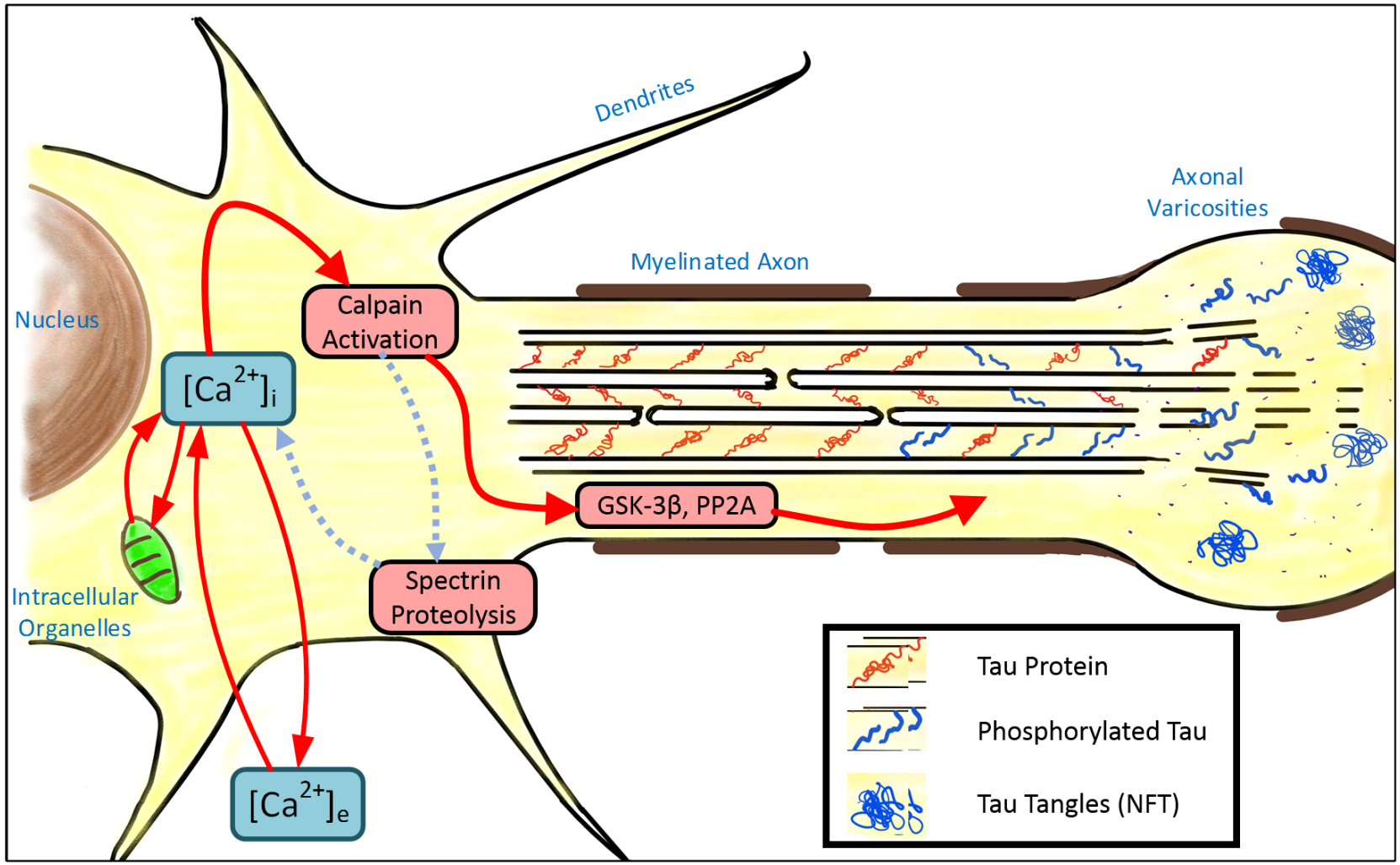

Figure 1.3: A schematic of pathway leading to rupture in microtubule assembly. Ca^{2+} accumulation due to Ca^{2+} homeostasis imbalance leads to calpain activation which disturbs the kinase - phosphatase (GSK-3β - PP2A) balance resulting in hyperphosphorylation of tau proteins. The hyperphosphorylated tau proteins thus lose their MT binding abilities, resulting in tau aggregation into NFT, and rupture of MT assembly. Additionally, calpain mediated spectrin proteolysis and its effect on subsequent increase in intracellular Ca^{2+} is shown. This pathway is shown in dotted lines as it is not explicitly modelled by us.

different anatomical parts of the brain. Efforts have been made to simulate actual impact through application of realistic linear and angular acceleration as initial conditions for the FE model of brain, based on the data obtained from experiments on cadaveric and crash test dummy heads, and live capture through accelerometers fixed on the helmets of football players in action (Bandak *et al.*, 2001; Zhang *et al.*, 2001, 2004). The output of finite element analysis in the form of principal strain, principal stress, shear strain, pressure and acceleration distribution in the brain is used to correlate with the occurrence of TBIs in the real world situation, thereby obtaining threshold values of these measures over which TBIs can be expected (Bandak *et al.*, 2001; Franklyn *et al.*, 2005; Takhounts *et al.*, 2003, 2008).

Accurate modeling of intracellular calcium ion (Ca^{2+}) concentration evolution is valuable as it is known to rapidly increase during a Traumatic Brain Injury. The transport of Ca^{2+} at the cellular level under homeostatic condition has been simulated in the literature using non-spatial compartmental model which defines a rate dependence through ordinary differential equations (Baker *et al.*, 2002; Falcke, 2004). Such models are valuable in predicting the outcomes of hypothetical propositions, and thus designing appropriate experiments towards understanding relevant phenomena, such as calcium signaling or the neurochemistry involved in neurodegenerative diseases (Slepchenko *et al.*, 2002). The compartmental models, in particular, consider that ions are exchanged between three kinetically homogeneous compartments, viz. the extracellular space (ECS), the cytoplasm, and the intracellular organelles such as ER (Kass and Lipton, 1986; Kowalewski *et al.*, 2006). Some studies assume the concentration in ECS to be unchanging, e.g. Kowalewski *et al.* (2006), while in some it is altogether neglected, e.g. Baker *et al.* (2002). Effects of external injuries or diseases on the homeostasis have not been widely modeled. Kass and Lipton (1986) accounted for the effect of anoxia by abruptly changing the parameter values in their model. Such an approach, however, is unable to account for the severity of the injury in the model. Kilinc (2008) studied the post TBI Ca^{2+} evolution due to mechanoporation by explicitly varying the PM permeability using a traffic based model to simulate ion transport mechanisms. In the same work, the activation of calpain and its activity on a general substrate was also simulated.

From a more mechanical perspective, Peter and Mofrad (2012) simulated the collapse of MT bundles due to mechanical failure of cross linking tau proteins using a discrete bead-spring model. Ahmadzadeh *et al.* (2014) modeled the tau protein as a viscoelastic

spring, enabling a strain rate dependence. This work was then extended by incorporating a separation of the tau-tau dimers involved in the MT bundle formation (Ahmadzadeh *et al.*, 2015). Sendek *et al.* (2014) simulated a random removal of tau proteins and the resulting MT bundle collapse in a two-dimensional (2D) space by equilibriating through steepest descent relaxation. Stepanov *et al.* (2018) developed a probability theory based model to simulate the multisite phosphorylation and dephosphorylation of tau protein, and concluded that kinase inhibition can prevent site specific tau hyperphosphorylation. Yet there is no deterministic mathematical link between the occurrence of a TBI and the resulting axonal rupture. While the work done by Peter and Mofrad (2012) and Ahmadzadeh *et al.* (2014) does bridge the gap to an extent, it takes into account only the mechanical failure of the tau protein links. While acknowledging the relevance of mechanical failure for severe cases of TBI, often the damage to the tau proteins and hence to MT bundles has a neurochemical origin. The Ca^{2+} influx mediated proteolytic damage via cleavage or phosphorylation of tau can account for the delayed injury seen in the axons, much after the occurrence of mechanical impact. Further the presence of phosphorylated tau in the form of filamentous bundles reported in vivo after the occurrence of a TBI, and in CTE brain samples, indicates an active presence of a neurochemical phenomenon, if not alone, working in tandem with the biomechanical phenomenon.

1.5 Motivation

Although detailed in terms of geometry and loading, the macro-scale FE models are purely mechanical in nature and do not consider any effects of the secondary insult. On the other hand, the effects of external injuries or diseases on the homeostasis of Ca^{2+} transport have also not been widely modeled. Kass and Lipton (1986) accounted for the effect of anoxia by abruptly changing the kinetic parameter values in their compartmental model of Ca^{2+} transport between neurons and ECS. Such an approach, however, is unable to account for the severity of the injury in the model. Kilinc (2008) studied the movement of calcium ions through a neuron during a mechanical trauma by applying a traffic based model to ion transport mechanisms. There is, however, still no model which incorporates the quantitative interrelation between the severity and symptoms of injury, a significant gap which we propose to fill through this work. To do so, we quantify the severity of the injury in terms of local mechanical stress, while the symptoms of injury are measured

through the intracellular calcium ion concentration. We hypothesize a definite correlation between the concentration of calcium ions and applied mechanical impulse load thereby providing the model with the capability to predict the local intracellular concentration if the local stresses being experienced are known. We then demonstrate the accuracy of the model by comparison with experimentally reported Ca^{2+} concentration evolution for different external loads (Weber, 2012; Maneshi *et al.*, 2015). We further spatialize this model by considering the brain tissue as a solid continuum with the Ca^{2+} activity occurring at every material point. Starting with one-dimensional representation, the brain tissue geometry is progressively made realistic and under the action of pressure or kinematic impulses, the effect of dimensionality and material behaviour on the correlation between the stress and concomitant Ca^{2+} concentration is investigated. The spatial calcium kinetics model faithfully captures the experimental observations concerning the Ca^{2+} concentration, load rate, magnitude and duration and most importantly shows that the critical location for primary injury may not be the most important location as far as secondary injury is concerned. Finally, we build a deterministic link between the occurrence of TBI and phosphorylation based loss of tau proteins from the MT bundles. This work also follows our previous non-spatial mathematical model for predicting intracellular Ca^{2+} in presence of a local hydrostatic stress due to a TBI. We present the mathematical formulation to capture the calpain activation, kinase truncation and tau phosphorylation. We establish a procedure for estimating the involved kinetic parameters, and finally apply realistic mechanical loads to examine the model behavior.

This report is organized in the following manner. In Chapter 2, we develop a mathematical model to create a constitutive relationship between local hydrostatic stress and intraneuronal calcium ion accumulation. In Chapter 3, we develop a mathematical framework to spatialize our previous model by coupling it with a transient structural FEM analysis performed on tissue geometries. We study the effects of stress waves and the influence of the tissue dimensions, and extend the observations to a realistic external 2D brain geometry for realistic loading conditions in the form of a pressure or kinematic impulses. In Chapter 4, we model the neuron dysfunction occurring as a result of calcium ion accumulation. We focus our attention on widely occurring mild TBIs, and the accompanying neurochemical phenomena leading to microtubule ruptures.

Chapter 2

Non-Spatial Calcium Kinetics

2.1 Compartmental Model

To understand the evolution of intracellular Ca^{2+}, we first study the Ca^{2+} kinetics in absence of any external loads to homeostatic conditions utilizing a non-spatial compartmental model. A non-spatial compartmental model renders the spatial distribution of ions through the cell and extracellular region immaterial (Baker *et al.*, 2002; Falcke, 2004; Kowalewski *et al.*, 2006; Kilinc, 2008). This simplification helps in circumventing complexities involving the intricate geometries of neurons and ECS. It homogenises the intracellular and extracellular domains offering a simpler and an elegant way to model Ca^{2+} transport. This assumption simplifies the model to a first degree of approximation without sacrificing any relevant physical details. However, due to the non-spatial description of Ca^{2+} ion transport considered here, our phenomenological model will be unable to capture the spatial distribution of ions inside the neuron and the extracellular matrix, as well as the nuances due to the distribution of the pores, pumps and channels in the plasma and ER membranes.

In our model the PM and ER membranes act as the interface between the compartments. We also include the changes in the extracellular Ca^{2+} concentration due to interactions with the cell, rather than assuming it to be a constant. The rate of change of extracellular concentration c_e and the intracellular concentration c_i with respect to time t is expressed as (Baker *et al.*, 2002; Falcke, 2004),

$$\begin{aligned} \frac{dc_e}{dt} &= -\left[J^p_{pm} + J^c_{pm}\right] \quad \text{and,} \\ \frac{dc_i}{dt} &= -\frac{dc_e}{dt} + \left[J^p_{er} + J^c_{er}\right], \end{aligned} \tag{2.1}$$

where J^p_{pm} and J^p_{er} are the rate of transport of ions through the *pores* in the PM and the ER membranes respectively. J^c_{pm} is the overall rate of transport of ions through the *channels* (e.g. VGCC, NMDA, etc.) and pumps (e.g. PMCA) of the PM and, J^c_{er} is the overall rate of transport of ions through the *channels* (such as IP3R) and pumps (such as SERCA) of the ER membrane (See Fig. 1.1).

Experimental observations suggest that the Ca^{2+} transport through the pores is diffusive in nature such that, (Falcke, 2004; Kowalewski *et al.*, 2006; Kilinc, 2008),

$$\begin{aligned} J^p_{pm} &= K_{pm}\left(c_e - c_i\right) \quad \text{and,} \\ J^p_{er} &= K_{er}\left(c_{er} - c_i\right), \end{aligned} \tag{2.2}$$

where c_{er} is the Ca^{2+} concentration inside the ER, and K_{pm} and K_{er} are the permeabilities of the PM and ER membranes respectively. The overall Ca^{2+} transport via pumps and channels is governed by a Hill type expression given as (Lytton *et al.*, 1992; Sneyd *et al.*, 1995; Baker *et al.*, 2002; Kowalewski *et al.*, 2006; Kilinc, 2008),

$$\begin{aligned} J^c_{pm} &= -V_{pm}\left(\frac{c_i^{n_{pm}}}{c_i^{n_{pm}} + k_{pm}^{n_{pm}}}\right) \quad \text{and,} \\ J^c_{er} &= -V_{er}\left(\frac{c_i^{n_{er}}}{c_i^{n_{er}} + k_{er}^{n_{er}}}\right), \end{aligned} \tag{2.3}$$

where V_{pm} (V_{er}) is the maximal overall activity of the PM (ER membrane) pumps and channels, k_{pm} (k_{er}) is the activation concentration for the PM (ER membrane), and the exponent n_{pm} (n_{er}) is the Hill coefficient representing the number of cooperative calcium sites required in the PM (ER membrane). We have used the homeostatic values of intracellular and extracellular Ca^{2+} concentration as 1×10^{-4} mM and 1 mM (Kowalewski *et al.*, 2006; Kilinc, 2008; Gleichmann and Mattson, 2011; Brini *et al.*, 2014). The values for the rest of parameters in equations Eqs. (2.1 - 2.3) are listed in Table 2.1. It must be noted that under a homeostatic condition, the flux terms J^c_{pm} and J^c_{er} counter the diffusive leakage of Ca^{2+} through the pores, J^p_{pm} and J^p_{er}, respectively. Hence, compared

Table 2.1: Value of Parameters
References – (1): Kilinc (2008) (2): Kowalewski *et al.* (2006)

Parameter	Definition	Value
c_i^*	Homeostatic value of intracellular concentration	1.00×10^{-4} mM (1),(2)
c_e^*	Homeostatic value of extracellular concentration	1.00 mM (1),(2)
c_{er}	Ca^{2+} concentration inside the ER	0.10 mM (1),(2)
K_{pm}	Porosity of the PM	2.94×10^{-6} s^{-1}
K_{er}	Porosity of the ER membrane	3.17×10^{-5} s^{-1}
k_{pm}	Activation constant of the PM	2.00×10^{-4} mM (1),(2)
k_{er}	Activation constant of the ER membrane	5.00×10^{-4} mM (1),(2)
n_{pm}	Hill Coefficient of the PM	2.00 (1),(2)
n_{er}	Hill Coefficient of the ER membrane	1.00 (1),(2)
χ_{pm}	Stress dependence parameter for V_{pm}	2.00×10^3
χ_{er}	Stress dependence parameter for V_{er}	4.00×10^3
κ	Stress dependence parameter 2	4.50×10^{-5} Pa^{-1}
α	Impulse contribution parameter	7.5×10^{-3} s^{-1}

to Eq. (2.2), the coefficients on the right-hand side of Eq. (2.3) are appended with a negative sign. The coupled differential equations, Eq. (2.1), along with Eqs. (2.2 - 2.3) can be solved for given initial conditions to obtain the evolution of the intracellular and extracellular concentrations.

2.2 Linear Stability Analysis

In order to verify that the model is inherently stable under homeostatic conditions, we perform a linear stability analysis of the governing equations Eqs. (2.1 - 2.3). Subsequently we solve the linearized governing equations analytically to obtain the closed form solution for the evolution of Ca^{2+} concentration in the extracellular and intracellular region of the cell. Importantly, such a stability analysis also reveals the intrinsic time scale of the system of equations, which in turn can be used to predict the time required for the system to attain stability either in presence or absence of external loads.

For a detailed analysis of the linear stability refer the Section A.1 of the Appendix

A. The eigenvalues of linearized governing equations are negative, which confirms the inherent stability of the system of governing equations Eqs. (2.1 - 2.3). Solution of the linearized governing equations under infinitesimally perturbed non homeostatic initial conditions reveals the evolution of the intracellular Ca^{2+} to be of the form:

$$c_i(t) = c_i^* + \mathbb{C}_1 e^{-t/\hat{\tau}_1} + \mathbb{C}_2 e^{-t/\hat{\tau}_2} \tag{2.4}$$

where $\hat{\tau}_{1,2} = 2\left(\beta \pm \sqrt{\beta^2 - \gamma}\right)^{-1}$ are the inherent time scales of the calcium kinetics system. In these equations, $\mathbb{C}_1$, $\mathbb{C}_2$, β and γ are constants dependent on the initial conditions and the kinetic parameters listed in Table 2.1. Their explicit definitions are provided in the Eq. (A.6) and Eq. (A.12) of the Appendix A. For the numerical value of the parameters as listed in Table 2.1, the intrinsic time scale of the system relevant to the physical mechanism of Ca^{2+} ion transport, denoted by $\hat{\tau}_1$, is found to be 13.62 s.

To verify the stability of the system of governing equations in action, we solve equations Eqs. (2.1 - 2.3) analytically for different non homeostatic initial perturbations. The evolution of the normalized intracellular concentration c_i/c_i^* thus obtained is plotted in Fig. 2.1. The numerical solution for each perturbation is also plotted in the same figure. We see that in each case, the intracellular concentration c_i settles to its homeostatic value c_i^*, thus confirming the inherent stability of the system of equations. The time taken for the settling to occur depends on the initial perturbation. The analytical solution reveals that intracellular concentration takes $\sim 4.6\hat{\tau}_1 \approx 63$ s to settle to a value one-hundredth of the initial perturbation, hereafter referred to as the settling time t_s. The stability of the governing equation implies that the model successfully captures the capability of the Ca^{2+} transport mechanisms to attain or maintain homeostatic conditions.

2.3 Incorporating Mechanical Stress

The local mechanical stress due to an external injury can affect intracellular and extracellular Ca^{2+} concentrations via several ion transport mechanisms as discussed earlier. In particular, there are strong experimental evidences to suggest that the NMDA and VGCC channels are prominent ion transport pathways over mechanoporation, while the outflux through PMCA and SERCA pumps is reduced (Smith and Meaney, 2000; Farkas *et al.*, 2006; Kilinc, 2008; Hemphill *et al.*, 2015; Hill *et al.*, 2016).Therefore, we assume that stress only affects the ion flux through the pumps and channels. Equation (2.3) shows that

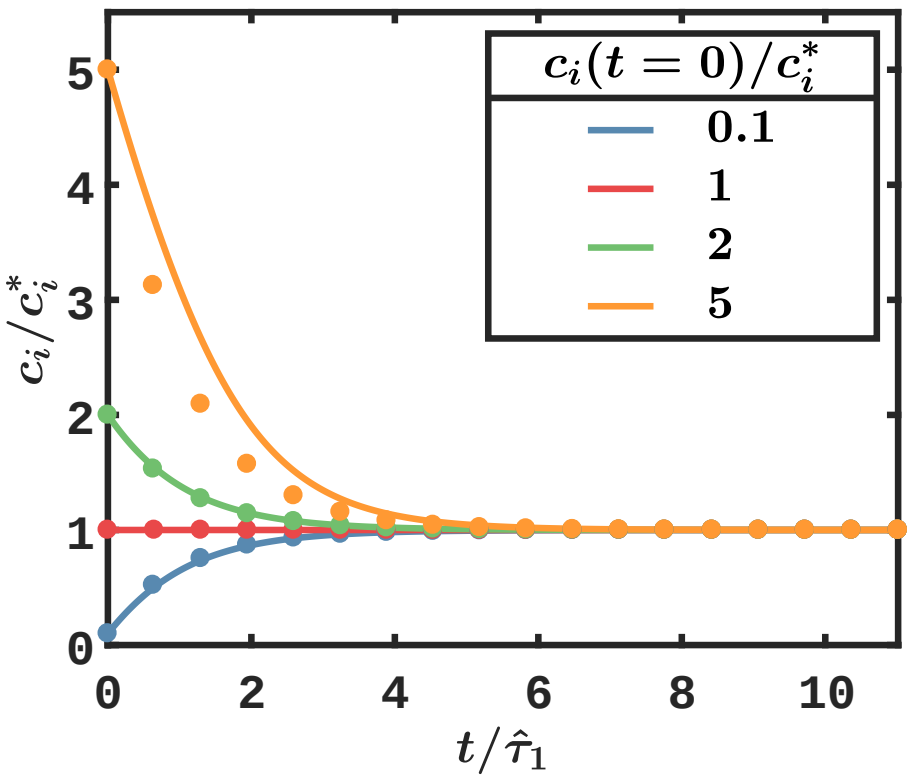

Figure 2.1: Temporal evolution of the intracellular concentration $c_i(t)$ normalized by the homeostatic concentration c_i^* under homeostatic (no loading) condition for different values of the initial intracellular concentration $c_i(t = 0)$. The solid lines denote the numerically obtained solution of the equations Eqs. (2.1-2.3) while the solid symbols indicate the analytical solution of the corresponding linearized equation (See Appendix A).

flux through pumps and channels of PM (ER) depends on three parameters, namely V_{pm} (V_{er}), k_{pm} (k_{er}) and n_{pm} (n_{er}). While it is plausible that all these parameters are affected due to a TBI, we hypothesize that the ion transport through PM and ER as a result of a TBI can be phenomenologically modelled to a first degree of approximation via the local stress dependence of V_{pm} (V_{er}), the maximum overall activity of channels and pumps. There is some experimental evidence to justify this hypothesis. It has been reported that more NMDA channels open up due to the secretion of glutamate after injury, further leading to an increased flux through other channels. The other parameters k_{pm} (k_{er})and n_{pm} (n_{er}), are generally empirically obtained from experiments, and there is much less clear evidence of their stress dependence.

The mechanical loading dependence of the kinetic parameters should: (a) account for the reversal in ion transport compared to homeostasis, due to TBI, (b) be nonlinear and convex since there cannot be an infinite increase in the rate of transfer of Ca^{2+} ions. Furthermore, experiments also indicate that the ion transport depends not only the instantaneous local stress, but also on its time history, as the intracellular concentration after an impulse loading is reported to stabilize at a much higher value than the homeostatic concentration. Considering these requirements, we model the dependence of the coefficients V_{pm} and V_{er} on the mechanical loading using an exponentially decreasing convex function as follows,

$$\begin{aligned} \frac{V_{pm}}{V_{pm0}} &= \left[-\chi_{pm} + \left(1 + \chi_{pm}\right) e^{-\kappa \hat{s}}\right], \\ \frac{V_{er}}{V_{er0}} &= \left[-\chi_{er} + (1 + \chi_{er})\, e^{-\kappa \hat{s}}\right], \end{aligned} \tag{2.5}$$

where χ and κ are constant parameters for the PM and ER membranes, and V_{pm0} and V_{er0} are the homeostatic values of the coefficients V_{pm} and V_{er}. Also, $\hat{s}$ is the measure of mechanical loading which comprises the instantaneous local stress and a time history dependent component such that,

$$\hat{s} = \sigma_h + \alpha \int_0^t \sigma_h(\bar{t}) d\bar{t}, \tag{2.6}$$

where σ_h is the local hydrostatic pressure and α is a constant parameter representative of the viscosity in the neuron.

A similar linear stability analysis as done in section 2.2, can be performed to examine the stability of the system under a non-zero constant mechanical loading (refer Appendix

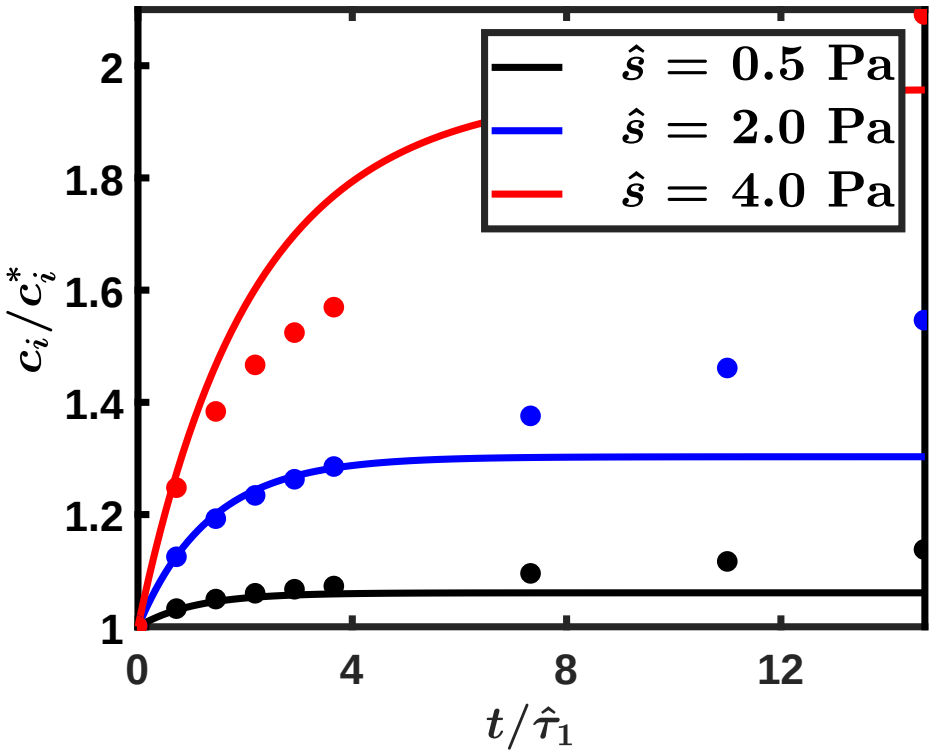

Figure 2.2: Temporal evolution of intracellular Ca^{2+} concentration, c_i, normalized by the homeostatic intracellular concentration, c_i^*, for a constant value of stress measure, $\hat{s}$. Coloured circles show the analytical solutions.

B). The linearized equations can be solved in closed form thus incorporating the effects of mechanical loading within the analytical framework (see Appendix B). The governing equations for this case also have identical eigenvalues as in the homeostatic case (refer Appendix B), confirming the stability of the system for smaller loads. Thus, for small loads the intrinsic time scale $\hat{\tau}_1$ also remains unchanged (see Appendix B).

2.4 Results and Discussion

2.4.1 Constant Mechanical Loading

We first begin with a hypothetical scenario where a constant mechanical loading $\hat{s}$ is being applied to the cells. Considering equation (2.6) this corresponds to two scenarios, (a) a neuron with a viscous parameter $\alpha = 0$ (no history dependence), experiencing a constant

hydrostatic stress, or (b) the loading state of a neuron under an impulse loading, long after the impulse has been removed. While case (a) may be hypothetical, the case (b) is commonly observed as most often a TBI occurs due to an external impact, similar to a short duration impulse (Faul *et al.*, 2010). In line with the magnitude of pressures applied in experiments reported in literature (Geddes-Klein *et al.*, 2006; Maneshi *et al.*, 2015), we assume the post-impulse mechanical loading parameter $\hat{s}$ to have a value ranging between 0.5 to 4 Pa. The numerically obtained evolution of the intracellular concentration is plotted in Fig. 2.2. Further we also show the analytical solution for each case. As expected due to linearization, for small loads and times the comparison fares well, while error increases for large loads and times. It is observed that the presence of stress in the system clearly induces an increase in the intracellular concentration. For each value of stress measure, there is a fixed concentration value c_{res} at which the intracellular concentration will settle. It is further observed that higher the loading measure, i.e. more severe the injury, higher will be the c_{res} and the time taken to settle at c_{res}.

2.4.2 Impulse Loads

A TBI generally occurs due to high magnitude impacts over a very short duration, such as in a fall, an automobile accident, or sports related incidents (Faul *et al.*, 2010). To mimic such an impact sudden short duration impulses are applied in experiments (LaPlaca *et al.*, 1997; Geddes and Cargill, 2001; Lusardi *et al.*, 2004; Geddes-Klein *et al.*, 2006; Maneshi *et al.*, 2015). Thus, in accordance with the literature on experimental studies of TBI, we considered impulse loads in the range of 10 to 50 kPa acting over a duration of 5 to 50 ms as an external stimulus. Figure 2.3 shows the numerically obtained evolution of the intracellular concentration when our model is subjected to impulses of different magnitudes (σ^*) and durations (t^*). Although we are assured of the accuracy of numerical solution by comparison with analytical solution, we do not plot the latter in this figure for clarity. A typical impulse profile is shown in the inset, where a load of magnitude σ^* is applied instantaneously at $t = 0$, and maintained for duration $t = t^*$, after which it is removed. In all cases, the evolution of Ca^{2+} concentration can be divided into two regimes: (1) $0 \leq t \leq t^*$, before the load is removed, and (2) $t > t^*$, after the load is removed. In the first regime ($0 \leq t \leq t^*$), when the applied load is constant for a very short period of time ($\sim 10\ ms$), an immediate increase in the intracellular Ca^{2+} concentration is observed. The intracellular concentration rises very rapidly to a peak value (c_i^{peak}).

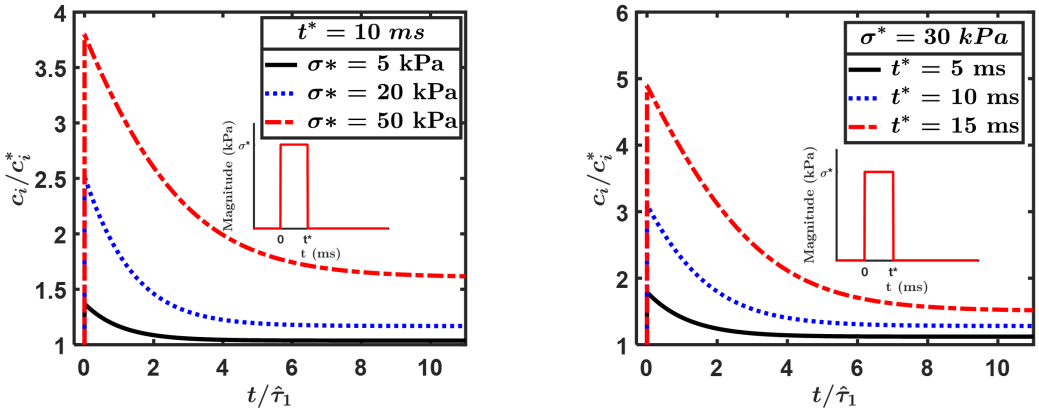

(a) **(b)**

Figure 2.3: Evolution of the intracellular concentration c_i due to an impulse load of magnitude σ^* applied at time $t = 0$ for a duration t^* (shown in the inset) when (a) the duration of impulse was fixed at $t^* = 10\ ms$, and (b) the magnitude of impulse load was fixed at $\sigma^* = 30\ kPa$. The intracellular concentration c_i is normalized with respect to the homeostatic intracellular concentration c_i^*.

Upon removal of the load ($t > t^*$), the intracellular concentration reduces gradually and settles to a residual value c_i^{res}, which is greater than the homeostatic concentration c_i^*. The settling time, $t_s = 4.6\hat{\tau}_1$, found in section 2.2 persists even for the impulse loading case and now indicates the time required for c_i to reduce to one hundredth of c_i^{peak}. As is evident from Fig. 2.3, our model is able to capture a gradual but not *total recovery* of the Ca^{2+} concentration in the cell upon removal of load, in agreement with the experiments reported in the literature (LaPlaca *et al.*, 1997; Geddes and Cargill, 2001; Lusardi *et al.*, 2004; Geddes-Klein *et al.*, 2006; Maneshi *et al.*, 2015). The non-zero value of the residual concentration indicates the presence of a permanent damage after the removal of the load. However, as seen from Fig. 2.3, for low magnitudes or smaller duration of impulse loads, the residual concentration is close to the homeostatic concentration, indicating that the lasting damage only occurs in case of severe injuries. This behaviour is also in agreement with experimental observations reported in literature (Geddes and Cargill, 2001; Maneshi *et al.*, 2015).

Next, we compare the evolution of the intracellular concentration in presence of impulse loads as predicted by our model with the calcium evolution observed experimentally. Additionally, such an exercise gives us a method to calibrate the kinetic parameters χ_{pm},

χ_{er} and κ in Eq. (2.5). Figure 2.4 shows the range (highest and lowest) of intracellular Ca^{2+} concentration in a human brian tissue sample experimentally measured by Maneshi *et al.* (2015) for a single impulse shown in the inset. By comparing our numerical results for the same impulse with the observed concentration evolution, we can obtain a range of values for the kinetic parameters, χ_{pm}, χ_{er} and κ. The values of the kinetic parameters corresponding to the numerical solution when compared with the lowest concentration evolution, as plotted in Fig. 2.4 are listed in Table 2.1. It should be noted that all the simulations reported henceforth use these calibrated values for the kinetic parameters. Figure 2.5 compares the model predictions with the observations of Geddes-Klein *et al.* (2006) where a single impulse shown in the inset of the figure is applied. As seen in Fig. 2.5, before the impulse load is applied, the model prediction of $c_i/c_i^* = 1$, is higher compared to the experiments due to the different homeostatic concentration (0.034 μM) used by Geddes-Klein *et al.* (2006) as compared to the value (0.1 μM) used here. However, we normalize both the experimental readings and the model output with respect to the homeostatic concentration of 0.1 μM assumed in this work. Post impulse, the model result (Fig. 2.5) is qualitatively same but underpredicts the concentration compared to the experiment by Geddes-Klein *et al.* (2006). This is most likely due to the different loading conditions and associated experimental uncertainties, as compared to the work of Maneshi *et al.* (2015), which were used to calibrate the kinetic parameters of the model. For completeness, Fig. 2.5 also shows the analytical solution obtained by solving Eq. (B.3) for the same initial and loading conditions.

It can be observed from Figs. 2.3-2.5 that in the presence of local mechanical stress induced by an injury, the residual (c_i^{res}) and peak (c_i^{res}) intracellular Ca^{2+} concentrations are much higher than the homeostatic value. The deviation of the Ca^{2+} concentration from the homeostatic value leads to a cascade of events which can eventually lead to the death of the neuron (Gaetz, 2004; Werner and Engelhard, 2007; Prins *et al.*, 2013). Hence, in this model, the secondary damage caused due to injury is represented in terms of the residual and peak Ca^{2+} concentration inside the cell. Figures 2.6a and 2.6b show the variation of the peak intracellular concentration, c_i^{peak}, as a function of the magnitude, σ^*, or the duration, t^*, of the impulse. Figure 2.6a also shows the experimental measurements of Maneshi *et al.* (2015) and we see that the model compares well. We further observe that c_i^{peak} initially rises with the increase in the magnitude of σ^*, but eventually stabilizes in agreement with the experiments. On the other hand from figure 2.6b, the model predicts

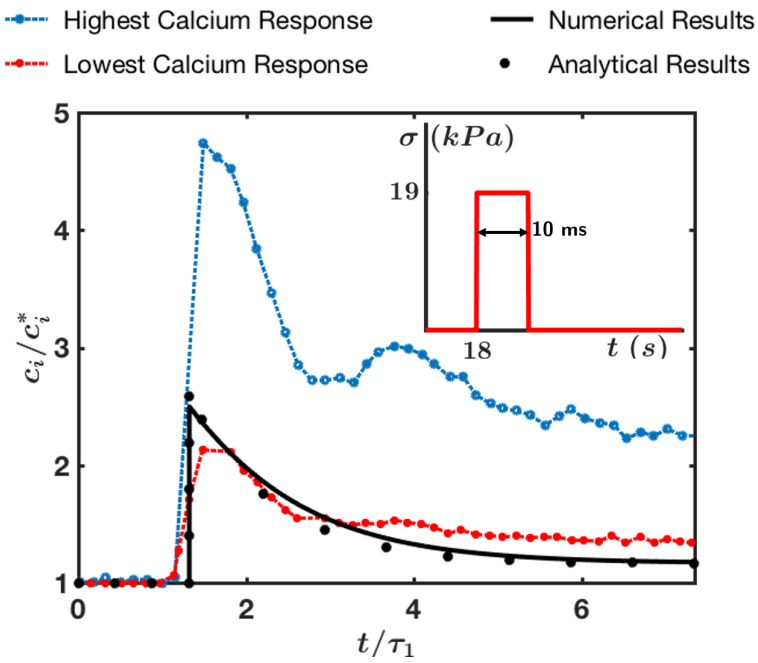

Figure 2.4: Calibrating the kinetic parameters, χ_{pm}, χ_{er}, and κ by comparing the model predictions with the experimentally measured intracellular Ca^{2+} for a single impulse load shown in the inset (Maneshi *et al.*, 2015). The analytical results for the linearised system under same loading conditions is plotted as black dots.

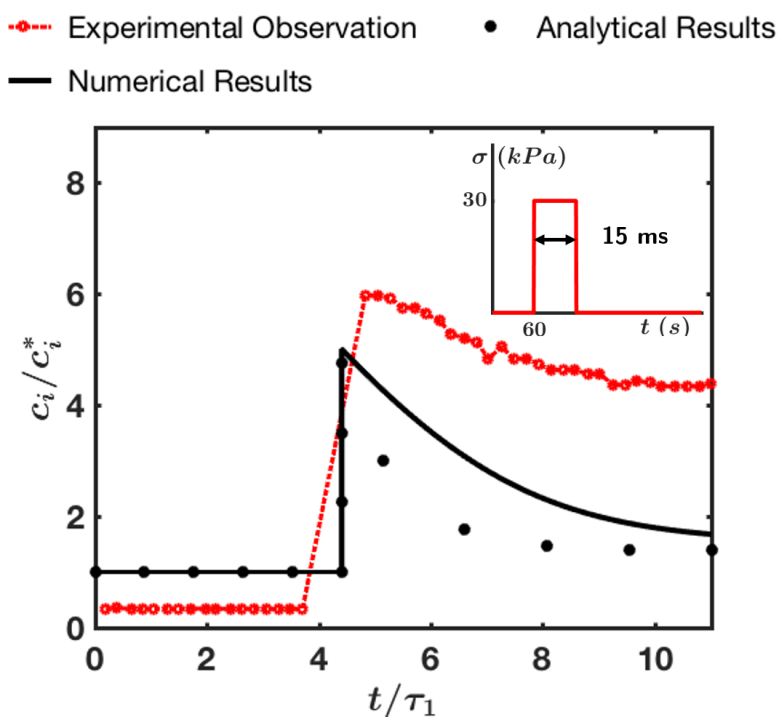

Figure 2.5: A comparison of the evolution of the intracellular concentration c_i normalised with respect to the homeostatic intracellular concentration c_i^* predicted by the model with experimental observations of Geddes-Klein *et al.* (2006) for single impulse load shown in the inset. The analytical results for the linearised system under same loading conditions is plotted as black dots.

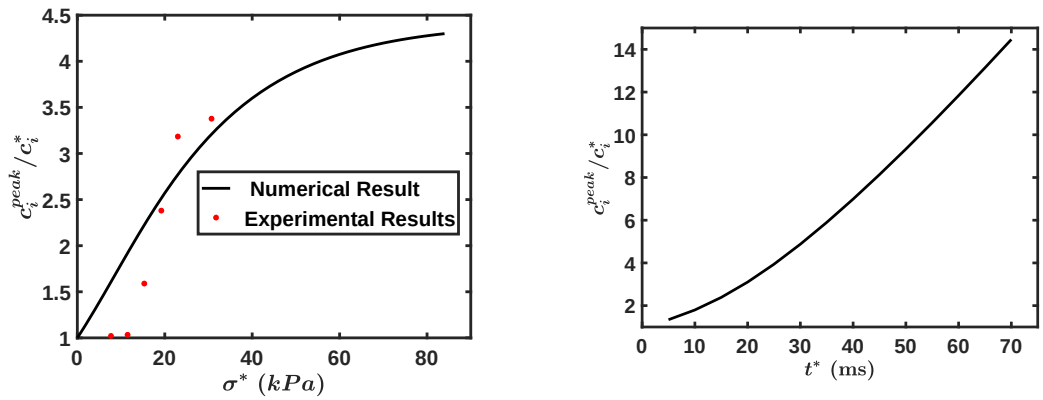

(a) (b)

Figure 2.6: The variation of peak intracellular Ca^{2+} concentration, c_i^{peak}, normalized with respect to the homeostatic intracellular concentration, c_i^*, with the severity of the injury, quantified in terms of the magnitude, σ^*, and duration, t^*, of a single impulse load, plotted in (a) and (b) respectively. Subfigure (a) also shows the experimental results reported by Maneshi *et al.* (2015), for a comparison with the model predictions. For (a) the duration of the impulse load t^* is kept constant at 10 ms, while for (b) the magnitude of the impulse is kept constant at 30 kPa.

that within the experimental time frame, the peak concentration rises monotonically with the duration of impulse, t^*, an observation which does not agree with the experiments of Maneshi *et al.* (2015), where for impulses of constant magnitudes the peak Ca^{2+} concentration begins to stabilize as durations exceed 1000 ms. In vitro, the stabilization may occur due to cell death (Gaetz, 2004; Werner and Engelhard, 2007; Prins *et al.*, 2013), a feature not explicitly simulated in our phenomenological model. Thus we are unable to predict the stabilization of the peak concentration within the experimental time frame.

Another important loading parameter which decides the severity of injury is the loading rate. Experiments have shown that faster loading can result in a more severe damage (Maneshi *et al.*, 2015). Our model takes the loading rate into consideration through the dependence of stress measure $\hat{s}$ (Equation (2.6)) on the loading history. For the same duration and same maximum value of impulse, the values of $\hat{s}$ are higher for a faster loading. As shown in Fig. 2.7, our model clearly predicts that a higher loading rate results in a higher peak and residual concentration of Ca^{2+} in qualitative agreement with experiments (Maneshi *et al.*, 2015).

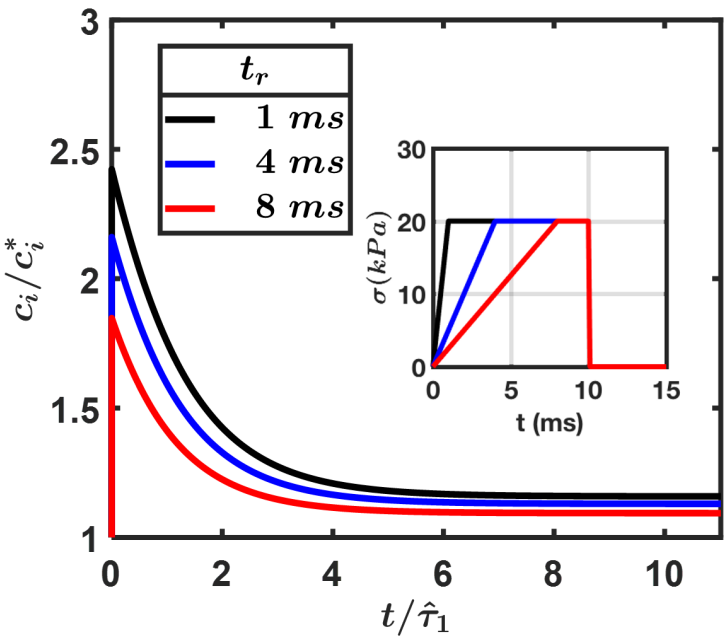

Figure 2.7: Temporal evolution of the normalized intracellular calcium concentration c_i/c_i^* for impulses of magnitude $\sigma^* = 20\ kPa$, total duration $t^* = 10\ ms$ with a gradual loading. The different loading rate is expressed in terms of the different time taken for impulse magnitude to reach its maximum value σ^*, t_r. The inset shows schematic of such impulses.

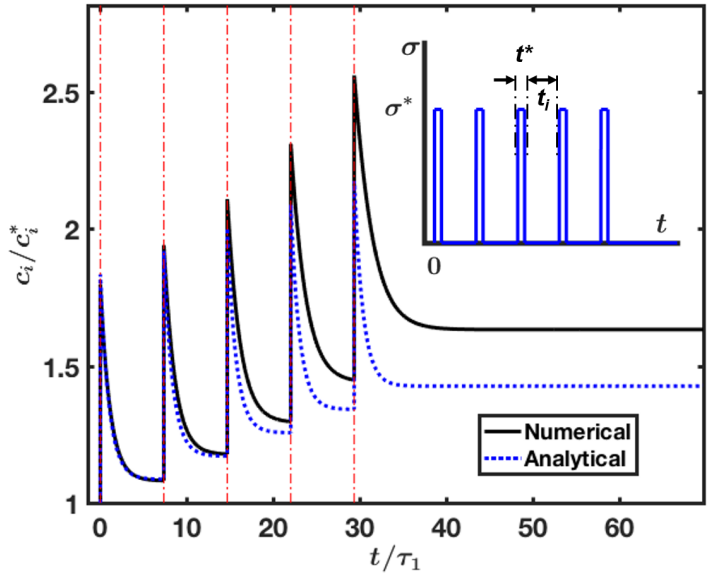

Figure 2.8: Temporal evolution of the normalized intracellular calcium concentration c_i/c_i^* for repeated impulses of magnitude $\sigma^* = 10\ kPa$, duration $t^* = 10\ ms$ each, applied with a time interval $t_i = 50\ s$ between them. The red dotted lines indicate the times at which the impulses act. The inset shows a schematic of such an impulse train.

2.4.3 Repeated Impulses

It is expected that in comparison to a single impulse, repeated impulses of the same magnitude and duration will have much more dire consequences. Experiments have reported that the rise in concentration after repeated impulses is much higher than that for a single pulse of the same duration and have attributed it to the viscoelastic/plastic behavior of the cell with regards to activation of the calcium ions (Maneshi *et al.*, 2015). In a similar manner, we applied a repeated impulse loading (schematic shown in the inset of Fig. 2.8) comprising of a series of five impulses, each of magnitude $\sigma^* = 10\ kPa$ and duration of $t^* = 10\ ms$ with a time interval of $t_i = 50\ s$ between them. Figure 2.8 shows the outcome where the times at which impulses are applied are denoted with red vertical lines. After the first impulse, the intracellular concentration begins to reduce to the residual value. However, before it can settle the second impulse acts, so that the concentration shows a second peak at a magnitude higher than the first peak. This continues to occur for each subsequent impulse. Each peak is progressively higher than the previous, thus capturing the viscoelastic/plastic behavior reported by experiments (Maneshi *et al.*, 2015). For

completeness, in FIg. 2.8, we also plot the analytical solution of the linearized governing equations. As expected, the error due to linearization builds up as the impulses progress, although all the key features are captured.

If the impulses are applied close to each other, the injury is expected to be more severe (Maneshi *et al.*, 2015). If the impulses are farther from each other, it can be expected that the cell gets some time to heal i.e. regain its homeostatic concentration c_i^* before the next impulse arrives. Extending this idea, if the impulses are sufficiently away from each other, the intracellular concentration would be as relaxed as possible before the next impulse comes in. Thus beyond a certain limit, increasing the time interval t_i between the pulses should not have any appreciable effect on the intracellular concentration. In order to verify these observations through our model, a number of impulse trains, each with a time interval varying between 0.1 to 100 s, are given as an external mechanical stimulus. For four such impulses, the temporal evolution of the normalized intracellular concentration is plotted in FIg. 2.9a. The model successfully predicts that short interval pulse trains result in a much higher peak intracellular Ca^{2+} concentration compared to the long interval pulse trains and hence a likelihood of greater injury to the cell. Further, Fig. 2.9b plots the variation of the normalized peak intracellular concentration with the time interval between the impulses normalized with respect to the intrinsic time scale $\hat{\tau}_1$. Figure 2.9b also shows that for interval between impulse greater than the settling time, $t_i > t_s(\sim 4.6\hat{\tau}_1)$, there is no significant change in the peak intracellular concentration. For the impulse train with $\sigma^* = 10\ kPa$ and $t^* = 10\ ms$, for a sufficiently large interval between the impulses, the peak concentration stabilizes to $\sim 2.5 \times 10^{-4}\ mM$ as shown in Fig. 2.9b.

It is worth noting from figure 2.9a that irrespective of the time interval between the impulses, the residual concentration does not change as long as the number, magnitude, and duration of impulses comprising the train remain same. The same observations are also obtained from the analytical solution of the linearized governing equations Eq (B.3). This indicates that the residual concentration is a cumulative result of the impulses comprising the impulse train, and is independent of when those impulses actually occurred. However, this does not mean that injury itself is a cumulative phenomenon, since the peak concentration, which determines the extent of the secondary injury is dependent on the time interval between the impulses (Fig. 2.9b). So far, no experiment has yet reported a relationship between the residual concentration and the time interval between impulses.

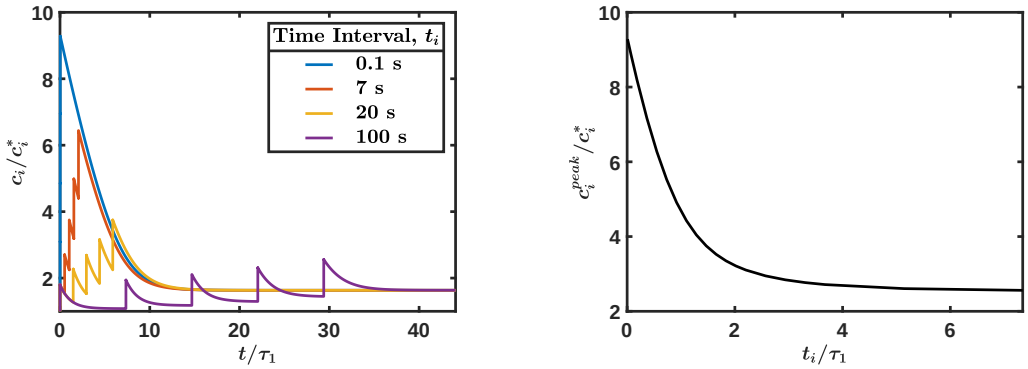

(a) (b)

Figure 2.9: The effect of varying the time interval between impulses, t_i. (a) Temporal evolution of normalised intracellular concentration c_i/c_i^* for four different impulse trains comprising of 5 impulses, each of magnitude $\sigma^* = 10\ kPa$ and duration $t^* = 10\ ms$, while the time interval t_i between the impulses is varied. (b)The variation of normalized peak intracellular concentration c_i^{peak}/c_i^* as a function of the time interval between impulses, t_i, in the impulse train. Each impulse train comprises of 5 impulses, each of magnitude $\sigma^* = 10\ kPa$ and duration $t^* = 10\ ms$.

Thus we would like to propose that further experiments could be designed to test the observation shown in Fig. 2.8.

2.5 Conclusion

In this chapter we have developed a simplified phenomenological model for the evolution of intracellular Ca^{2+} concentration, thereby predicting the damage to neurons due to external impacts such as in a TBI. We use the kinetics of Ca^{2+} ion transport mechanisms (Kass and Lipton, 1986; Baker *et al.*, 2002; Falcke, 2004; Kowalewski *et al.*, 2006; Kilinc, 2008) to describe the rate of change of intracellular and extracellular concentrations. We have incorporated the effect of mechanical loading during TBI through stress history dependent kinetic parameters governing the flux of pumps and channels in the plasma and ER membranes. The next step in development of our model would involve introducing a spatial dimension. This could be done either at neuron level, where the local stress as well as the chemical kinetics becomes dependent on the distribution of pores and channels in the membrane, or at the tissue level, where due to large difference between length scales of neuron and a tissue, non-spatial chemical kinetics could be combined with the spa-

tial distribution of local stresses. We believe that latter approach will provide interesting insights into the change of Ca^{2+} kinetics due to external injuries.

Chapter 3

Applying a Continuum Treatment

3.1 Continuum Framework Based Spatialization

2D and 3D continuum based FE models of human brain have long been used to simulate TBIs numerically and predict the locations susceptible to high principal stresses and strains (Bandak *et al.*, 2001; Zhang *et al.*, 2001; Takhounts *et al.*, 2003; Pena *et al.*, 2005). Although detailed in terms of geometry and loading, the macro-scale FE models are purely mechanical in nature and do not consider any effects of the secondary insult. In the work presented in this chapter, our older non-spatial calcium kinetics model dealing with the effect of mechanical stress upon the Ca^{2+} transportation in a neuron is spatialized by considering the brain tissue as a solid continuum with the Ca^{2+} activity occurring at every material point. In our spatial model, it is assumed that Ca^{2+} kinetics acts independently at every material point of the tissue and is influenced only by the local absolute hydrostatic stress. The accumulation of Ca^{2+} in neuron is simulated through the equations Eqs. (2.1-2.3) governing the transport of Ca^{2+} across the plasma and ER membrane as shown in the Fig. 1.1. Kinetic parameters governing the calcium flux through the channels and pumps is dependent on the local stress through equations Eqs. (2.5-2.6). The spatial dimension is introduced in the model by treating the tissue as a solid continuum satisfying the equation of motion given as (Jog, 2015),

$$\rho \frac{\partial^2 u_j}{\partial t^2} = \frac{\partial \sigma_{ij}}{\partial x_i} + \rho b_j \tag{3.1}$$

where, σ_{ij} is the ij^{th} component of the symmetric Cauchy stress tensor, u_j and b_j are the jth component of deformation and body force per unit mass respectively and ρ is the

density. The indices i and j in Eq.(2.3) takes values of $1, \ldots, N$ where N is the dimension of the domain representing the tissue. Under the assumption of small deformation, the measure of deformation is characterized through strain ε_{ij} defined as,

$$\varepsilon_{ij} = \frac{1}{2}\left(\frac{\partial u_i}{\partial x_j} + \frac{\partial u_j}{\partial x_i}\right). \tag{3.2}$$

Out of the many available constitutive models for the brain tissue in the literature (Miller and Chinzei, 1997; Galford and McElhaney, 1970; Mendis *et al.*, 1995; Prange and Margulies, 2002; Rashid *et al.*, 2013), the linear viscoelastic model is the most widely used, and is the model we follow in our study (Galford and McElhaney, 1970; Shuck and Advani, 1972; Kang *et al.*, 1997; Donnelly and Medige, 1997). The stresses and strains are decomposed into deviatoric and hydrostatic parts and related to each other as (Christensen, 1982),

$$\begin{aligned} \sigma_{ij}^{dev}(x_i, t) &= \int_0^t 2\mathbf{G}(t-\tilde{t})\frac{\partial \varepsilon_{ij}^{dev}(x_i, \tilde{t})}{\partial \tilde{t}} d\tilde{t}, \quad \textit{and} \\ \sigma_h(x_i, t) &= 3\mathbf{K}\varepsilon_h(x_i, t), \end{aligned} \tag{3.3}$$

where, σ_{ij}^{dev} (ε_{ij}^{dev}) and σ_h (ε_h) indicate respectively the deviatoric and the hydrostatic components of the Cauchy stress (strain). The hydrostatic response expressed through Eq.(3.3) is assumed to be elastic and governed by the time-independent bulk modulus $\mathbf{K}$ while the deviatoric stress is linearly related to deviatoric strain rate through time-dependent shear modulus $\mathbf{G}(t)$, as noted in Eq.(3.3). In the present work, the viscoelastic nature of the tissue is simulated through standard linear solid model (SLSM) which leads to the functional form of $\mathbf{G}(t)$ as (Christensen, 1982),

$$\mathbf{G}(t) = \mathbf{G}_\infty + \mathbf{G}_1 e^{-t/\tau} \tag{3.4}$$

where, $\mathbf{G}_\infty$ is the long term shear modulus, and $\mathbf{G}_1$ is the shear modulus corresponding to the relaxation time τ. Equations (3.1-3.4) in conjunction with variety of loading scenarios and boundary conditions over various geometries of the brain tissue are solved either analytically or numerically using commercial finite element method (FEM) software COMSOL Multiphysics. The hydrostatic stress evolution at any point of interest is then used to solve Eqs. (2.1-2.3,2.5,2.6) in MATLAB to obtain the time dependent intracellular concentration evolution $c_i(t)$ at the point. In the further sections, the coupled

Table 3.1: Material Properties of Brain Tissue (Shuck and Advani, 1972; Anderson, 2000)

Parameter	Value
$\mathbf{G}_\infty$	16.70 kPa
$\mathbf{G}_1$	32.30 kPa
$\mathbf{K}$	1.13 MPa
τ	6.89 ms
ρ	1040.00 kg/m^3

model will be applied to different loading scenarios starting with simple 1D models graduating to a realistic 2D brain geometry. The values of the material properties occurring in Eqs. (3.1-3.4) are listed in Table 3.1, and used henceforth.

3.2 Results and Discussion

3.2.1 Analytical Solution

A simplified 1D bar problem forms the basis for understanding the correlation between the geometry and viscoelastic nature of the tissue, load characteristic like magnitude, duration and resulting stress and Ca^{2+} concentration. We begin with a simplest possible case of a viscoelastic bar of length 'L' as shown in Fig. 3.1 subjected to a fixed boundary condition at one end ($u_x(0,t) = 0$) while a constant pressure is applied at the other end ($\sigma_x(L,t) = \sigma^*(t) = \sigma^*, t > 0$). Applying Eqs. (3.1-3.4), the closed form expression for the evolution of stress $\sigma_x(\xi, s)$ in the Laplace domain is analytically obtained as (refer Appendix C for derivation),

Figure 3.1: Tissue modelled as 1D viscoelastic bar of length L and thickness $L/100$, constrained at end $x = 0$, and subjected to a load $\sigma^*(t)$ at the other end. The viscoelastic behaviour of the bar is represented through Eqs.(3.3-3.4) and Table 3.1.

$$\frac{\bar{\sigma}_x(\xi, s)}{\sigma^*} = \frac{1}{s} + \frac{4}{\pi}\sum_{n=1}^{\infty}\left[\frac{(-1)^n}{(2n-1)} \times \frac{s(s+\psi)}{s^3 + \psi s^2 + \frac{(2n-1)^2\pi^2}{4M^2}s + \frac{(2n-1)^2\pi^2}{4M^2}\psi(1-\psi)} \times cos\left\{\frac{(2n-1)\pi\xi}{2M}\right\}\right] \tag{3.5}$$

where, ξ is the non dimensionalized space co-ordinate, M is the ratio of the length L of the bar to the material length scale $L_m = \eta/\sqrt{\rho \mathbf{E}_0}$, $\psi = \mathbf{E}_1/\mathbf{E}_0$ is a material constant, and $\mathbf{E}_1$, $\mathbf{E}_0$ and $\mathbf{E}_\infty$ are the constants occurring in the modified SLS relaxation law, $\mathbf{E}(t) = \mathbf{E}_\infty + \mathbf{E}_1 e^{-\mathbf{E}_1 t/\eta}$ (Eq.(C.1)), which can be derived from Eq.(3.4). The values of the material properties occurring in Eqs.(3.1-3.4) are listed in Table 3.1, and used henceforth. For the material constants, listed in Table 3.1, we note that the material length scale $L_m = 53.904$ mm. In terms of material length scale L_m, the bounding box of a typical human brain is approximately $3.5L_m \times 2.5L_m \times 2L_mC$. (Duvernoy, 1999). Thus a typical length scale representative of the human brain tissue can be taken as 50 mm and is the value adopted as the tissue length in the 1D and 2D models discussed below, unless otherwise specified.

Under the action of constant load at the free end of 1D bar (Fig. 3.1), using Laplace inversion of Eq.(3.5), Fig. 3.2a-c show the evolution of stress normalised with respect to the applied load, at the fixed end ($\xi = 0$) for varying length $L = \{5, 50, 100\}$ mm ($M = \{0.093, 0.928, 1.856\}$) of the bar. The solution clearly brings out the combined effect of bar inertia and viscoelastic effect. As opposed to a quasi-static case, the stress state is inhomogeneous in space and time owing to the multiple interaction between the original stress wave and waves generated due to reflections at the boundaries. The viscoelastic material behavior additionally induces damping and over a sufficiently long time, the stress settles to the solution corresponding to the quasi-static condition and represented through the first term in the R.H.S of Eq. (3.5). As the length L of the bar decreases (i.e. as M decreases), the time taken for the waves to reach the fixed end decreases. Consequently shorter the bar, higher will be the frequency of stress oscillations. However in each case, the time taken to attain steady quasi-static solution is almost same as it depends on the time scale embedded in the viscoelastic law rather than the bar dimensions. It is expected that these conclusions will persist even if the load pattern is varied, as will be seen in the next section where a more realistic rectangular impulse load is applied. Thus an important takeaway here is that in a mechanically loaded tissue, since the mechanical stress varies

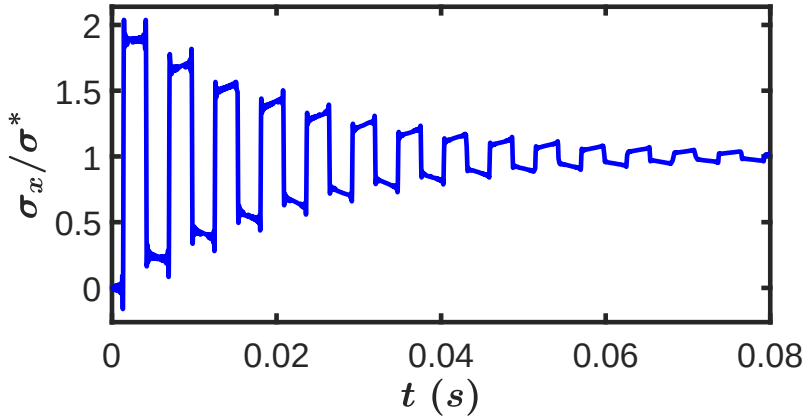

(a)

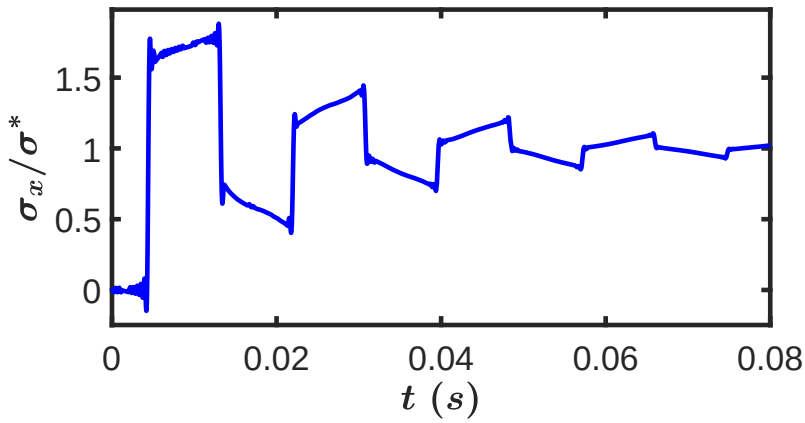

(b)

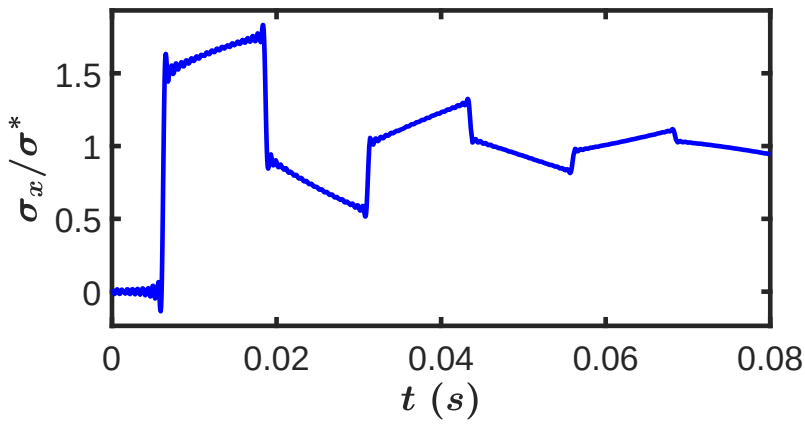

(c)

Figure 3.2: The stress evolution with time normalised with respect to applied load σ^* based on Eq.(3.5) at the fixed end ($x = 0$) of a tissue modelled as 1D viscoelastic bar (Fig. 3.1) of length (a) $L = 5\ mm$, (b) $L = 50\ mm$, and (c) $L = 100\ mm$ under application of a constant load $\sigma(t) = \sigma^*$ at the other end.

temporally and spatially in turn modifying the intracellular Ca^{2+} concentration, a continuum spatial model for the intracellular Ca^{2+} kinetics is an important step to identify the critical locations for a secondary injury.

3.2.2 Uniaxial Pressure Impulse – Geometry Effects

A TBI generally occurs due to high magnitude impacts over a very short duration, such as in a fall, an automobile accident, or sports related incidents (Faul *et al.*, 2010). To mimic such an impact, sudden short duration impulses are applied in experiments (LaPlaca *et al.*, 1997; Geddes and Cargill, 2001; Lusardi *et al.*, 2004; Geddes-Klein *et al.*, 2006; Maneshi *et al.*, 2015). In order to assess the effect of transient loading, 1D bars of length $L = \{5, 50, 100\}$ mm are subjected to a rectangular impulse of magnitude 30 kPa and duration 10 ms. For a rectangular impulse case, deriving a closed form solution analogous to Eq.(3.5) is extremely tedious due to case-specific Laplace inversion process. Hence, Eqs.(3.1-3.4) for different loading and boundary conditions are solved numerically over the tissue geometry using a commercial finite element method (FEM) software COMSOL Multiphysics. To approximate the 1D behaviour in COMSOL, we maintain the bar width as $L/100$ for all 1D simulations henceforth. Additionally, the large gradients of a rectangular impulse are smoothed over a very short duration of time $t_{smth} = 1$ ms to avoid very high loading rates and associated numerical instabilities. To allow for this numerical smoothing, the body remains at rest for a short duration of time $t_0 = 5$ ms before the impulse acts. The simulations are run till a solution time of 500 ms to make sure that all the transient stress disturbances are entirely captured. For 1D bar, we use a mapped mesh consisting of linear quadrilateral plane stress elements with element size of ≈ 1 mm. An unconditionally stable implicit 'generalized α' time integration scheme is used to avoid numerical damping of the impulse waves. To obtain a spatially smooth solution, the time stepping is restricted such that $t_{step} \leq 0.8 * x_{ele}^{min}/v_p$, where x_{ele}^{min} is the smallest element size in the mesh and $v_p = \sqrt{\mathbf{E}_0/\rho} = 11.8$ m/s ($\mathbf{E}_0$ is defined in Eq.(C.3)) is the elastic pressure wave speed. Following the SLS viscoelastic material properties listed in Table 3.1 we use a maximum time step of 0.05 ms. To obtain the intracellular Ca^{2+} evolution at any point, the hydrostatic stress σ_h from the FEM solution is used in the calcium kinetics model represented through Eqs.(2.1-2.3,2.5,2.6) and solved in MATLAB. The calcium kinetics model is run till both the intracellular and extracellular calcium concentrations settle to a constant value at all points on the bar, which occurs at approximately 200 s.

Table 3.2: The peak local hydrostatic stress (σ_h^{peak}) and peak intracellular Ca^{2+} concentration (c_i^{peak}) in tissue modelled as 1D viscoelastic bars (Fig. 3.1) of different lengths L, under an application of impulse loads of magnitude $\sigma^*(t) = 30$ kPa when $t_0 < t < t_0 + t_i$, 0 otherwise, for different impulse durations t_i.

t_i (ms)	$L = 5$ mm		$L = 50$ mm		$L = 100$ mm	
	σ_h^{peak} (kPa)	c_i^{peak} ($\times 10^{-4}$ mM)	σ_h^{peak} (kPa)	c_i^{peak} ($\times 10^{-4}$ mM)	σ_h^{peak} (kPa)	c_i^{peak} ($\times 10^{-4}$ mM)
10	19.62	3.13	17.82	7.04	16.16	5.27
30	19.62	8.52	17.82	9.64	17.36	9.96
50	19.62	13.24	17.82	13.43	17.36	13.95

This is approximately 3 times the settling time t_s analytically obtained for the homeostatic calcium kinetics model in the previous chapter, Section 2.2. It must be noted the solution of the calcium kinetics model takes at most 0.5 s for our machine as compared to the simulation time of ≈ 2500 s for the FEA solver, implying calcium kinetics solution is a computationally inexpensive addition to the FEM analysis.

Figures 3.3a, c and e show the evolution of hydrostatic stress at $x = \{0,\ L/2,\ \text{and } L\}$ for bars of length $L = \{5, 50, 100\}$ mm respectively, under the action of impulse load of magnitude 30 kPa applied for a duration of 10 ms. For completeness, the evolution of longitudinal strains in the corresponding bars are plotted in Fig. 3.3b, d and f. Similar to the analytical results for constant load shown in Figs. 3.2a-c, as the length of the rod reduces, the frequency of oscillations of stress increases. In the case of 5 mm long bar, within the duration of impulse, the stress completes multiple oscillations. The calculated stress for the impulse loading is then used to compute the Ca^{2+} evolution at the fixed end of the bar. Table 3.2 compares the peak hydrostatic stress and peak Ca^{2+} concentration for the three bar lengths {5, 10, 100} mm under the application of impulses of magnitude 30 kPa and duration 10 ms, 30 ms and 50 ms. We observe that as the length of the bar increases, the peak hydrostatic stress reduces. Similar observation can be noted through Fig. 3.3 also. But a comparison of the peak Ca^{2+} concentration reveals that it is least in the shortest bar where the peak hydrostatic stress is found to be the highest. Thus the first important result of this chapter is that the location of maximum stress and maximum peak concentration need not be the same. Hence the critical location of the primary insult predicted by FE based models through various criterion like maximum principal strain, principal

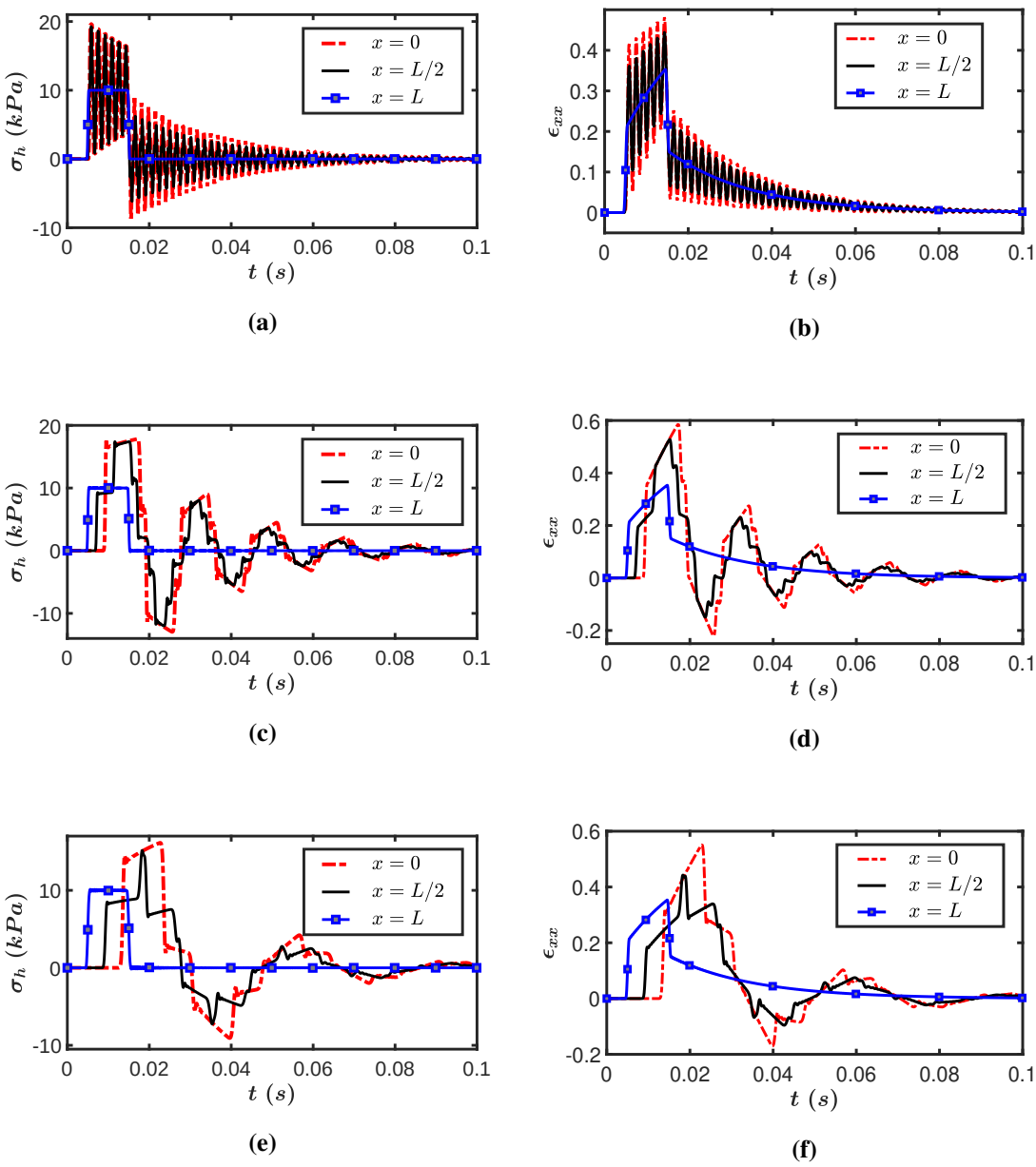

Figure 3.3: The numerically obtained evolution of hydrostatic stress σ_h is plotted at the fixed end ($x = 0$) and the mid point ($x = L/2$) of the bar of length (a) $L = 5$ *mm*, (c) $L = 50$ *mm*, and (e) $L = 100$ *mm*, for a rectangular impulse load $\sigma^*(t) = 30$ kPa when 5 ms $< t <$ 15 ms, 0 otherwise. The hydrostatic stress at $x = L$ shown using the solid line with square markers is equivalent to the applied impulse scaled by a factor of 1/3. The corresponding longitudinal strain ϵ_{xx} is plotted the bars of length (b) $L = 5$ *mm*, (d) $L = 50$ *mm*, and (f) $L = 100$ *mm*

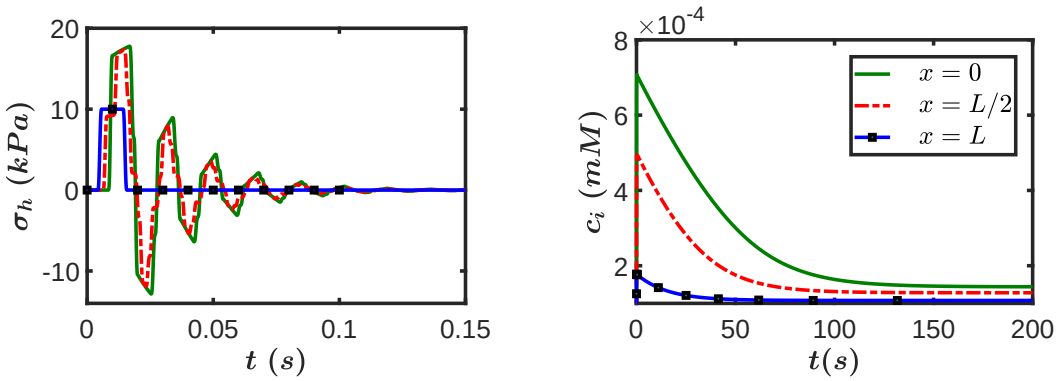

(a) **(b)**

Figure 3.4: The evolution of (a) local hydrostatic stress σ_h and (b) intracellular Ca^{2+} concentration c_i at the fixed end ($x = 0$), the mid point ($x = L/2$) and the free end ($x = L$) of a tissue modelled as 1D viscoelastic bar (Fig. 3.1) of length $L = 50$ mm, under application of an impulse load $\sigma^*(t) = 30$ kPa when 5 ms $< t <$ 15 ms, 0 otherwise. The hydrostatic stress at $x = L$ shown using the solid line with square markers is equivalent to the applied impulse scaled by a factor of 1/3.

stress, shear stress or pressure (Anderson, 2000; Bandak *et al.*, 2001; Zhang *et al.*, 2001; Levchakov *et al.*, 2006; Mao *et al.*, 2006; Takhounts *et al.*, 2008) is not necessarily the location of importance as far as damage due to secondary insult is concerned. We further see from Table 3.2 that as the duration of impulse increases, the peak hydrostatic stress remains same, but the peak Ca^{2+} concentration increases. This observation emphasizes the significance of the duration of the elevated stresses in addition to the magnitude of stress in the context of damage due to secondary injury, a factor not considered significant in prediction of primary injury by earlier FEM based models.

3.2.3 Uniaxial Pressure Impulse – Impulse Effects

In order to delve further into the effects of spatialization we study the variation in the concentration at different points on the 1D bar upon application of impulse loads. Figure 3.4 shows the evolution of hydrostatic stress and concentration corresponding to the free end of the bar of length $L = 50$ mm being subjected to an impulse of magnitude 30 kPa applied for a duration of 10 ms and then suddenly removed. Figure 3.4a shows the evolution of the hydrostatic stress with respect to time at three locations, viz. $x = 0$, $x = L/2$, and $x = L$, on the bar. The intracellular Ca^{2+} concentration is also evaluated at these points, and it's

evolution is plotted in Fig. 3.4b. The local intracellular Ca^{2+} concentration at any point initially rises very rapidly to a peak value, c_i^{peak}. Once the local stress has almost reduced to zero, we observe a slow decay in the intracellular Ca^{2+} concentration until it settles to a residual value c_i^{res}, which is greater than the homeostatic concentration, c_i^*. Although the qualitative predictions of the spatial model proposed here look similar to the non spatial model predictions in the previous chapter, Section 2.4.2, we note that the results are significantly different. We see that application of hydrostatic stress at any single point would result in a rectangular impulse shaped stress evolution, similar to the stress evolution at $x = L$, in Fig. 3.4a, which would only produce a peak concentration of 1.773×10^{-4} mM, as shown in Fig. 3.4b. However, in our new spatial model of Ca^{2+} kinetics, the transfer of force through the geometry of the tissue, via a propagating longitudinal stress wave, is taken into account, thus resulting in a much higher intracellular Ca^{2+} concentration ($\approx 7 \times 10^{-4}$ mM). The propagated and reflected stress waves interfere and result in a hydrostatic stress evolution akin to the application of repeated impulse loading in a non spatial calcium kinetics model as discussed in Section 2.4.3. Further, from Fig. 3.4, it can be seen that the more constrained region of the tissue will experience a higher mechanical stress as compared to the other regions for the same applied external load, and is thus more susceptible to not only primary, but also secondary injuries due to the higher Ca^{2+} accumulation. But this correspondence between the location of maximum stress and concentration is not always followed as seen earlier from Table 3.1, where the length of the bar was varied. Thus we would like to reiterate that depending upon the geometric details of the tissue, applied load magnitude and duration, the highest Ca^{2+} accumulation, and hence the secondary damage, may not always be seen at the exact locations where highest peak pressure is observed. For a more realistic depiction of the human brain, it is possible that at a location, a smaller peak pressure may be observed, but it may be sustained for a longer duration. While such a region may not be susceptible to a primary injury, our model predicts that such a region may still be critical due to the occurrence of secondary damage involving calcium kinetics.

Next we study the effect of the magnitude and duration of the applied impulse on the intracellular Ca^{2+} concentration evolution. In accordance with the literature on experimental studies of TBI, we vary the magnitudes of rectangular impulse loads over a range of 10 to 60 kPa acting over a duration of 5 to 200 ms as an external stimulus at the free end of the bar (Geddes and Cargill, 2001; Geddes-Klein *et al.*, 2006; Maneshi *et al.*,

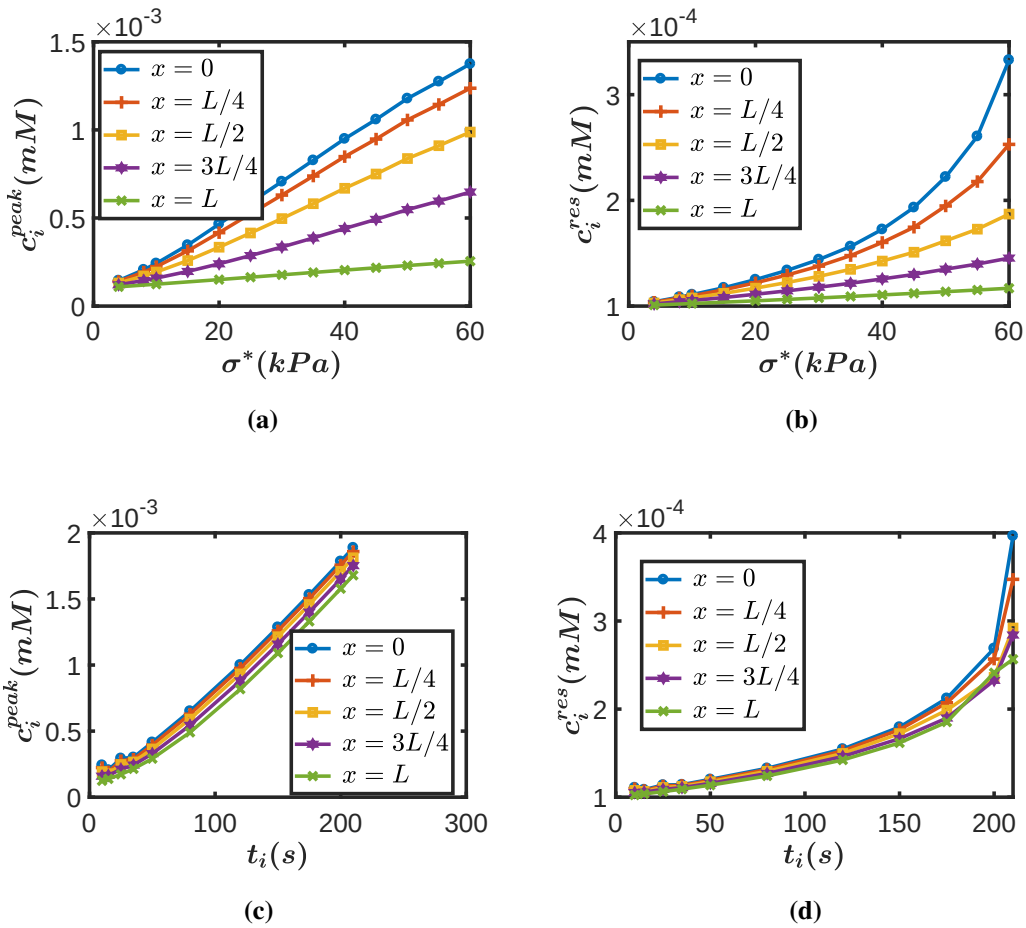

Figure 3.5: The evolution of peak c_i^{peak} and residual c_i^{res} Ca^{2+} concentration at different locations along the length of the bar if only the magnitude σ^* ((a) and (b) respectively) or the duration t_i ((c) and (d) respectively) of a rectangular impulse load $\sigma^*(t) = \sigma^*$ when $t_0 < t < t_0 + t_i$, 0 otherwise, applied at the free end of tissue modelled as 1D viscoelastic bar (Fig. 3.1) of length $L = 50$ mm are varied. In the former case ((a) and (b)), the duration $t_i = 10$ ms is kept constant, while in the latter case ((c) and (d)), the magnitude $\sigma^* = 10$ kPa is kept constant.

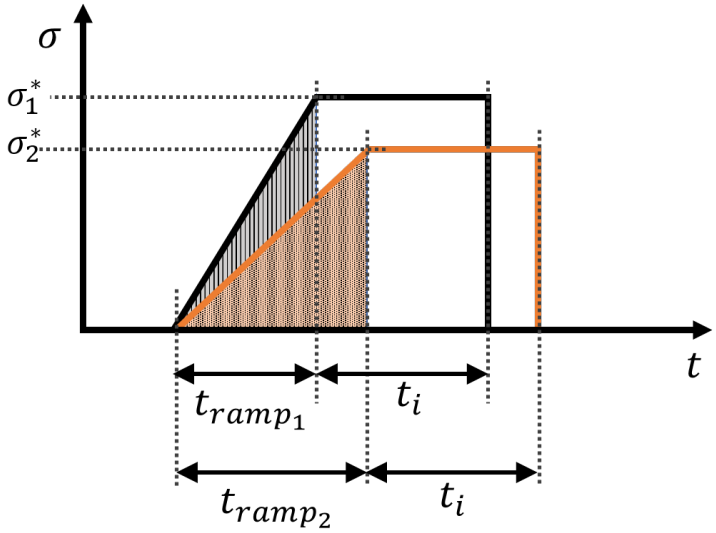

Figure 3.6: Two ramped impulses where the area under the ramped portion of the impulse shown as the shaded region is kept constant, in order to keep the severity of impulse mathematically defined as $\int \sigma dt$, constant. After the ramping portion, the impulses are held at a uniform value for a time t_i and then instantaneously brought to zero.

2015). It is expected that for a more severe external load, involving an impulse of either a higher magnitude or duration, a more severe secondary damage would be observed. We compare the peak and residual Ca^{2+} concentrations for different impulses, where either the magnitude of impulse is kept constant while the duration of impulse is varied, or vice versa. The variation of the peak and residual Ca^{2+} concentration with respect to the variation in the impulse magnitude from 10 to 60 kPa, while the impulse duration is kept a constant at 10 ms, is plotted in Fig. 3.5a and 3.5b respectively. Similarly, in Fig. 3.5c and 3.5d, we plot the variation of the peak and residual Ca^{2+} concentrations respectively, when the magnitude of the impulse is kept constant at 10 kPa, while the impulse duration is varied in the range of 5 to 20 ms. As expected, it is observed that as either the impulse magnitude or duration increases, the peak as well as the residual Ca^{2+} concentrations also monotonically increase. Experiments by Maneshi *et al.* (2015) indicate a similar pattern, which is observed to stabilize to a constant value for larger magnitudes or durations of the applied impulse. In vitro such stabilization may be due to the cell deaths at higher Ca^{2+} concentrations (Gaetz, 2004; Werner and Engelhard, 2007; Prins *et al.*, 2013), a feature that we have not explicitly simulated in our phenomenological model.

Experiments by Cullen and LaPlaca (2006); Elkin and Morrison III (2007); Maneshi

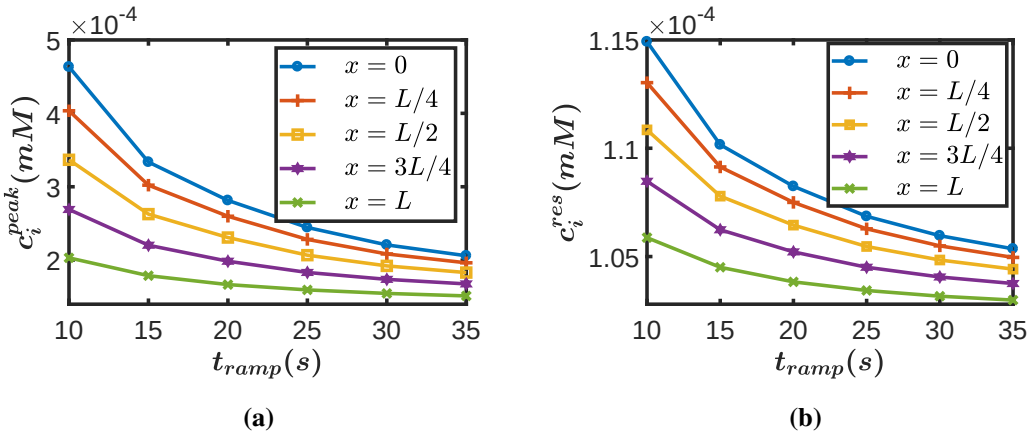

Figure 3.7: The variation of peak c_i^{peak} and residual c_i^{res} Ca^{2+} concentration at different locations along the length of the bar as a function of the duration of the ramping (t_{ramp}) of the ramped impulse having same severity of impulse (see Fig. 3.6) applied at the free end of the 1D viscoelastic bar of length L (Fig. 3.1) mimicking a tissue.

et al. (2015) indicate that the application of higher loading rates results in a greater chance of cell death. As discussed in Section 2.4.2, the calcium kinetics model takes the loading rate into consideration through the dependence of stress measure, $\hat{s}$, on the local hydrostatic stress history via Eq. (2.6). We apply ramped impulse loads increasing the load rate (slope of the $\sigma - t$ line in Fig. 3.6), while keeping the 'impulse' (mathematically given as $\int \sigma dt$, or the area under the stress-time curve shown as the shaded region in Fig. 3.6) during the ramped portion a constant. Following the ramped portion, the load is maintained constant for a specified time t_i, and then it suddenly ends as shown in Fig. 3.6. As shown in Fig. 3.7, it is observed that as the time during the ramped portion, t_{ramp}, is increased or as the loading rate of the applied impulse is deceased, both the peak and the residual Ca^{2+} concentrations reduce. Thus our model ensures that the secondary damage predicted is dependent on the rate of the applied pressure load, following the trends observed experimentally.

3.2.4 Equibiaxial Pressure Impulse

Several experiments have been conducted where an equibiaxial pressure loading is applied on brain tissue samples (Geddes and Cargill, 2001; Morrison III *et al.*, 2003; Geddes-Klein *et al.*, 2006; Cullen and LaPlaca, 2006). In line with these experiments, we apply

equibiaxial pressure impulse on a square tissue geometry. We apply roller boundary condition on two adjacent sides of the geometry, while on the other adjacent faces equal pressure impulses are applied as shown in the insets in Figs. 3.8a, 3.8c, and 3.8e. The local hydrostatic stress and the local intracellular Ca^{2+} evolution that we obtain in response to an impulse of magnitude 30 kPa suddenly dropped to zero after a duration 10 ms, are plotted in Fig. 3.8. The results are qualitatively the same as our 1D model predictions. It is observed that if an impulse of same magnitude and duration is applied in a uniaxial and equibiaxial fashion, both the stress as well as the intracellular Ca^{2+} concentration are higher for the equibiaxial loading as seen through comparison of Fig. 3.4b and Fig. 3.8b. This result agrees with the experimental observations by Geddes-Klein *et al.* (2006) where higher peak Ca^{2+} was observed for a biaxial stretch. Further, we have observed that the trends exhibited by the peak (c_i^{peak}) and residual (c_i^{res}) Ca^{2+} concentration with respect to change in impulse magnitude, duration, and the loading rate observed for the one dimensional uniaxial case, as discussed in section 3.2.3, are followed for the biaxial loading as well. These results are not shown for the sake of brevity. Lastly we would like to report that a maximum peak strain of approximately 0.3 is observed in the simulations of biaxial pressure impulse.

A much more significant observation is made when the length of the sample in the simulation is varied as shown in Fig. 3.8. As in the 1D case discussed in section 3.2.3, when the length of the geometry is reduced, the frequencies of the stress waves increase as shown in Figs. 3.8a, 3.8c, and 3.8e. In the case of a 2D geometry, the normally propagating longitudinal stress waves are coupled with each other through the Poisson's effect in the material. Further, the interactions between these waves give rise to transient shear waves. The presence of shear waves in a purely compressive biaxial loading might be counterintuitive, but their presence can be understood by appreciating that the shear waves are transient in nature, and will disappear even if the external biaxial compressive loads are not removed. Presence of shear waves is not contingent on the viscoelastic nature of tissue and are in fact observed even if the material is assumed to be linear elastic. As we transition from Figs. 3.8a,b to 3.8c,d to 3.8e,f, it is observed that smaller the size of the square shaped tissue, greater is the overlap between curves for stress and concentration evaluated at different locations. Thus with the reduction of tissue dimensions, the spatial relevance of the model vanishes and the present model converges towards the non-spatial calcium kinetics model discussed in the previous chapter. A similar observation

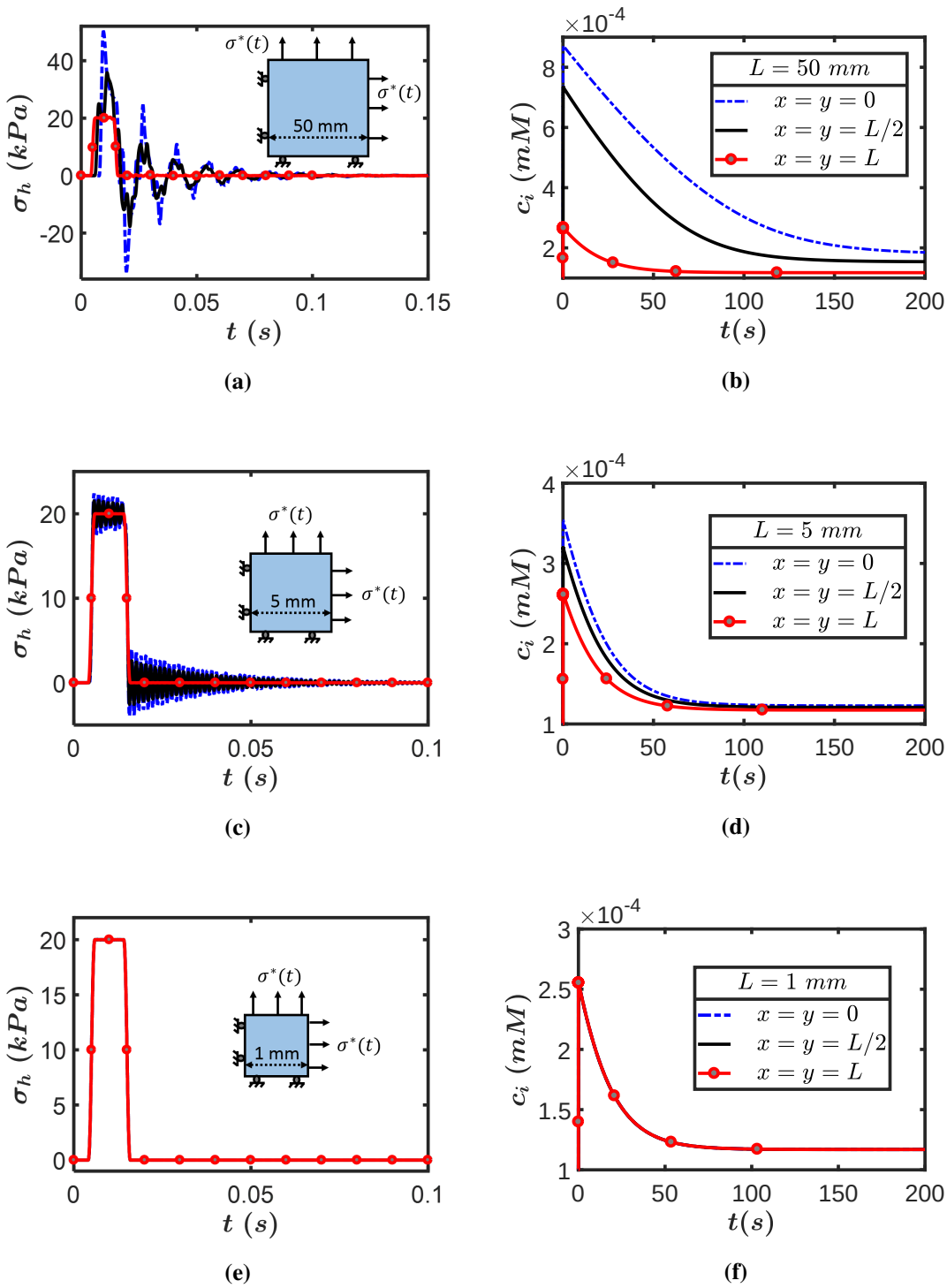

Figure 3.8: The local hydrostatic stress σ_h and the intracellular Ca^{2+} concentration c_i evolution with time t at different locations along a 2D square tissue of varying edge length, under the application of an equi-biaxal impulse load $\sigma^*(t) = 30$ kPa when 5 ms $< t <$ 15 ms, 0 otherwise. The square tissue obeys the viscoelastic material response represented through Eqs.(2.5-2.6) and Table 3.1. The hydrostatic stress at $x = y = L$ shown in (a,c and e) using the solid line with circular markers is equivalent to the applied impulse scaled by a factor of 2/3.

can be readily made from the expression of stress distribution in a 1D bar under a constant uniaxial pressure (Eq.(3.5)) whereby as the bar becomes shorter ($M \rightarrow 0$), the stress distribution and consequently the Ca^{2+} becomes independent of the spatial coordinate ξ. As the tissue length decreases, before a sufficient inertial delay or viscoelastic decay can occur, the stress waves will reflect from the opposite end of the bar. The longitudinal stress wave travels with velocity $v_p = 11.8$ m/s (Section 3.2.2), while the viscoelastic decay occurs at a time scale $\tau = 6.897$ ms (Table 3.1). The length L of the bar will be short enough to be inconsequential if the wave can travel through it and reflect back to the original point in a time $\leq 0.1 \times \tau = 0.6897$ ms, during which a negligible viscoelastic decay will occur. Thus, the longest bar in which the wave can reflect back without enough dissipation is $(\sqrt{\mathbf{E}_0/\rho}) \times 0.1\tau/2 = 4$ mm. Indeed, our simulations reveal that for tissues shorter than 4 mm in dimension the overlap between the hydrostatic stress evolution at various points is highly pronounced. In other words, we propose that the Ca^{2+} concentration predictions of the non-spatial model will match with the predictions of the spatialized model as long as the length of the tissue being modelled is less than or equal to $(\sqrt{\mathbf{E}_0/\rho}) \times 0.1\tau/2 = 4$ mm (Table 3.1).

This observation assures us that calibration of the kinetic parameters listed in Table 2.1, which was performed in Section 2.4.2 by comparing the the non-spatial model results with the experimental observations of Maneshi *et al.* (2015) and Geddes-Klein *et al.* (2006), is still held valid for the spatial calcium kinetics model. Further, this observation suggests that in an experiment if the characteristic dimension of the specimen of the tissue is longer than 4 mm, the local pressure at any point will deviate appreciably from the externally applied pressure. Thus a true hydrostatic stress condition, with zero shear, is not maintained. Therefore the Ca^{2+} accumulation will vary at different points on the specimen. To avoid unwanted error due to transient stress waves and to maintain a uniform Ca^{2+} accumulation throughout, it is proposed that the specimen dimension in experiments should not exceed 4 mm.

3.2.5 Kinematic loading

TBIs can be caused by not only external forces, but also sudden vigorous motion of the head-neck complex commonly occuring during sport incidences and blast induced shock. (Margulies and Thibault, 1992; Zink, 2001; Gaetz, 2004; Werner and Engelhard, 2007). In such situations, the whole of the head undergoes rotational and/or translational

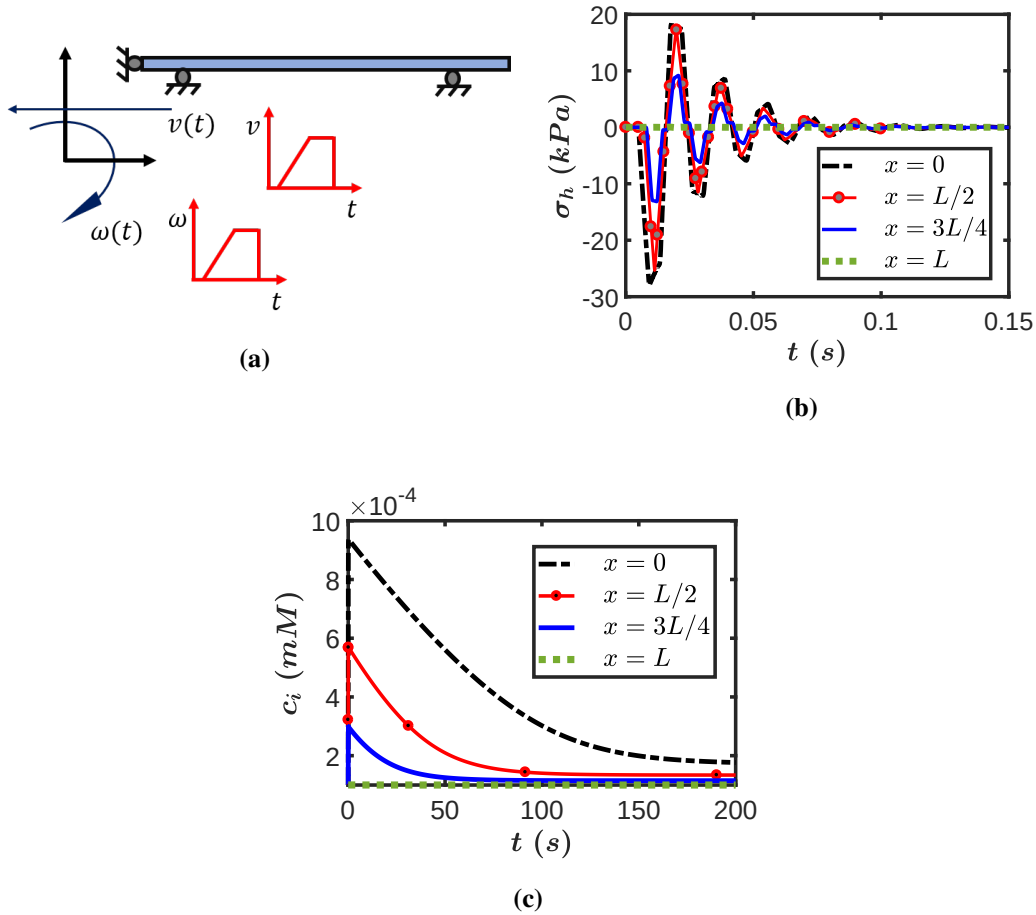

Figure 3.9: Kinematic translational and rotational impulses corresponding to the loading parameters for data set 2 listed in Table 3.3 are applied on a tissue modelled as a 1D viscoelastic bar of length L = 50 mm and width L/100, as shown in the schematic (a), resulting in the evolution of the (b) local hydrostatic stress, and (c) the intracellular Ca^{2+} concentration which are plotted at 4 different locations along the length of the bar.

Table 3.3: Kinematic loading conditions obtained from the experimental observations of Nusholtz *et al.* (1984), used for the 1D and the 2D simulations of tissue. The peak hydrostatic stress (σ_h^{peak}) and the peak Ca^{2+} intracellular concentration (c_i^{peak}) obtained from simulations are listed along with the experimentally observed peak pressures and physiological injuries.

	v_{max} (m/s)	ω_{max} (rad/s)	α_{max} (rad/s^2)	a_{max} (m/s^2)	t_i (ms)	σ_h^{peak} (kPa)			c_i^{peak} $\times 10^{-4}$ (mM)		**Observed Injury**
Cadaver Impact						**1D**	**2D**	**Expt**	**1D**	**2D**	
1	7	28	7250	1900	10	26.25	33.85	12, 51	8.89	7.01	Subarachnoid hematoma, Frontal lobe hemorrhage
2	7.5	20	8000	1800	12	27.98	33.77	38,42	9.37	7.47	Subarachnoid hematoma, Parietal lobe hemorrhage
3	4.5	30	3900	420	25	12.14	10.87	11,12	3.37	3.14	Frontal and Parietal subarachoid hemorrhage
4	3.8	30	7500	1350	12	21.06	21.06	25	3.92	3.92	No injury

acceleration-deceleration and the resulting injury is usually diffused in nature as opposed to the focal injuries due to localized impact (Smith and Meaney, 2000; Rowson *et al.*, 2012). It has often been proposed that kinematic parameters such as rotational acceleration during vigorous head motion may act as a basis for primary insults during a TBI (Ommaya and Gennarelli, 1974; Margulies and Thibault, 1992; Gaetz, 2004). Such inertial injuries can be simulated by applying rotational and/or translational acceleration all along the geometry through the body force per unit mass term $\mathbf{b} = \mathbf{a}_{lin} + \mathbf{a}_{cen} + \mathbf{a}_{cor} + \mathbf{a}_{eul}$ in Eq.(3.1), where linear acceleration $\mathbf{a}_{lin} = \frac{d\mathbf{v}}{dt}$, centripetal acceleration $\mathbf{a}_{cen} = \omega \times (\omega \times \mathbf{r}_p)$, Coriolis acceleration $\mathbf{a}_{cor} = 2\omega \times \frac{\partial \mathbf{u}}{\partial t}$, and Euler acceleration $\mathbf{a}_{eul} = \frac{d\omega}{dt} \times \mathbf{r}_p$. Here $\mathbf{r}_p$ is the position vector of the point of interest, and the kinematic inputs $\mathbf{v}(t)$ and $\omega(t)$ are input linear and angular velocity impulse functions as shown in Fig. 3.9a.

Nusholtz *et al.* (1984) have conducted experiments on Rhesus head and a human cadaver subjected to external impact and recorded the maximum linear and angular acceleration, velocities and observed injuries as noted for few cases in Table 3.3. We adopt this information as kinematic loading input and solve the equation of motion (Eq.(3.1)) along with the constitutive response (Eqs.(3.3-3.4)) and thereupon the calcium kinetics model (Eqs.(2.1-2.6)) to investigate the effect of tissue geometry and dimension on the Ca^{2+} evolution and further attempt to correlate with the observed injury in experiments. The linear velocity ($\mathbf{v}(t)$) and angular velocity ($\omega(t)$) are applied as ramp input to achieve the maximum values as listed in columns 2 and 3 of Table 3.3 respectively. The duration of ramping is selected such that the linear and angular accelerations attain the maximum values as listed in columns 4 and 5 of Table 3.3 respectively. Post ramping, the impulse is maintained for time t_i given in column 6, Table 3.3 followed by sudden drop to zero (see Fig. 3.9a). Note that the kinetic parameters and material constants mentioned in Tables 2.1 and 3.1 are persisted for the calculations in this section. Analogous to pressure-loading dealt in Section 3.2.2, we start with 1D tissue of length 50 mm (width is kept at 0.5 mm to ensure a 1D behaviour) constrained by roller support along two edges as shown in Fig. 3.9a and subject it to kinematic loading based on values taken from Table 3.3. Fig. 3.9b and Fig. 3.9c show the evolution of hydrostatic stress, and Ca^{2+} concentration corresponding to the kinematic loading represented by data set 2 from Table 3.3. Similar exercise is carried out for a 2D square tissue of side 50 mm where two adjacent edges are constrained by roller support and subjected to kinematic loading from Table 3.3. Based on the results of 1D and 2D simulations, the peak values of hydrostatic stress

σ_h^{peak} and Ca^{2+} concentration c_i^{peak} are extracted and appended in Table 3.3. The Table 3.3 also lists the experimentally observed peak pressure as reported by Nusholtz *et al.* (1984). In some of the experimental cadaver impacts, a bimodal pressure evolution (with two peaks) was observed in the cadaver brains, and for such cases both the maxima values are listed. A comparison of the numerically observed peak pressures with the peak hydrostatic stress observed in experiments reveals that inspite of the simplification of geometry, constraint assumptions, the simulation results are significantly comparable with experiments. Amongst the 1D and 2D calculations, the latter seems to show a marginally better comparison with respect to the experimental observations. A comparison of the peak Ca^{2+} concentrations with the experimentally observed injuries reported in the last column of Table 3.3 (Nusholtz *et al.*, 1984) does not reveal any significant correlation. However, subarachnoidal hematomas are noted to occur only in the case when the peak Ca^{2+} concentrations are higher. In the 1D and 2D simulations with the kinematic loading, a maximum peak principal strain of approximately 0.4 were observed.

3.2.6 2D Brain Geometry

In this section, we apply the spatial calcium kinetics model to a realistic 2D geometry of the brain tissue. Duvernoy (1999) photographed a series of 2 mm thick coronal sections of a 188 mm long specimen of the right cerebral hemisphere. As a geometric input for the simulation, we considered the section along the central coronal plane, i.e. 94 mm from the front end, as shown in Fig. 3.10a (Duvernoy, 1999). The points along the outline of the cerebral hemisphere were extracted via WebPlotDigitizer and a smooth curve was interpolated through these points and mirrored along the central sagittal plane to obtain the contour for both the hemispheres (Rohatgi, 2018). The outline is also offset by a maximum thickness of 4 mm to obtain a geometry for the meninges surrounding the upper portion of the cerebrum (See Fig. 3.10b). The meninges comprise of the falx cerebri, the Pia-Arachnoid Complex and the dura mater and its material behaviour is assumed to be a linear elastic material with Young's Modulus 31.5 kPa, Poisson's Ratio 0.45, and density 1130 kg/m^3 (Takhounts *et al.*, 2008). Fig. 3.10b shows a representative mesh of the 2D brain tissue used for analysis. We have clearly labelled the cerebrum and the meninges in the geometry. Without compromising the mesh quality, we found that 1588 triangular plane stress elements are enough to faithfully capture the geometry. Due to narrow geometries involved in the meninge domain, having a maximum thickness of 4 mm and a

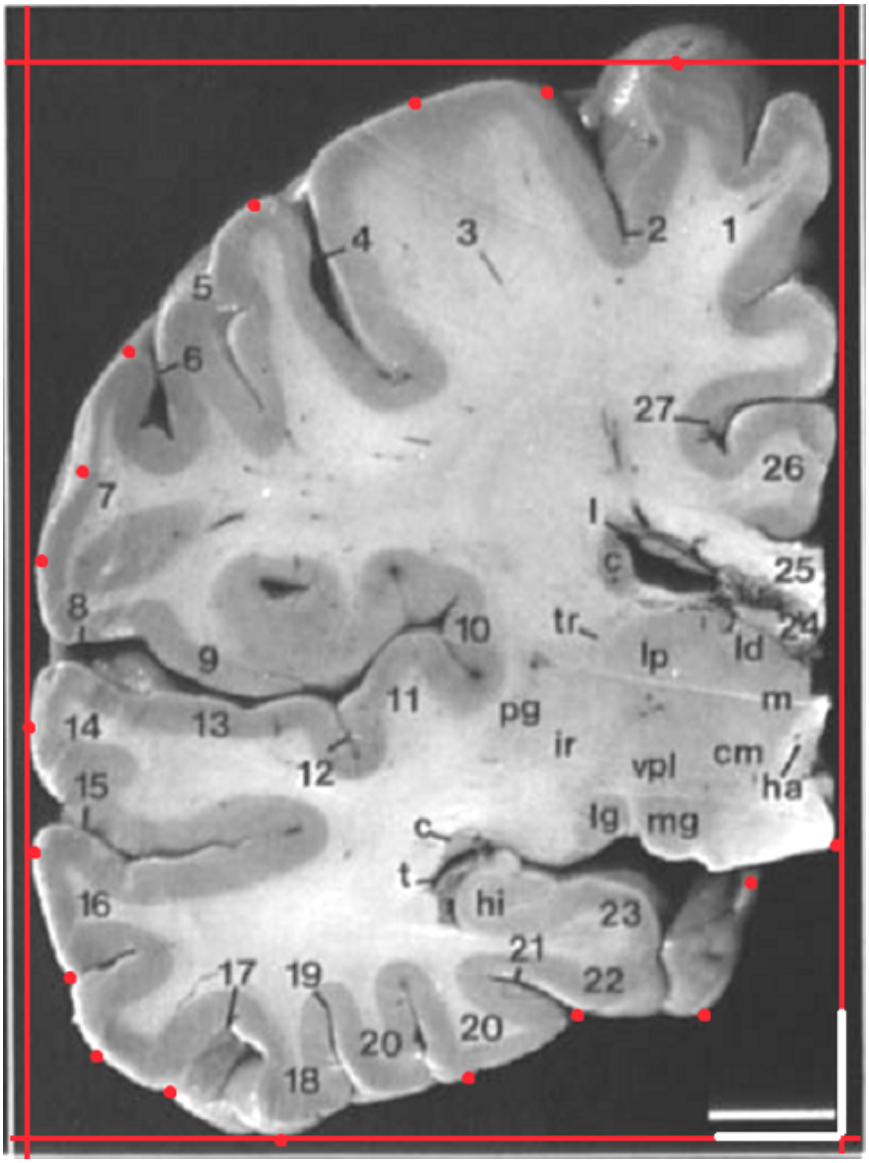
1
2
3
4
5
6
7
8
9
10
11
12
13
14
15
16
17
18
19
20
20
21
22
23
24
25
26
27
l
c
tr
lp
ld
m
pg
ir
vpl
cm
ha
lg
mg
c
t
hi

(a)

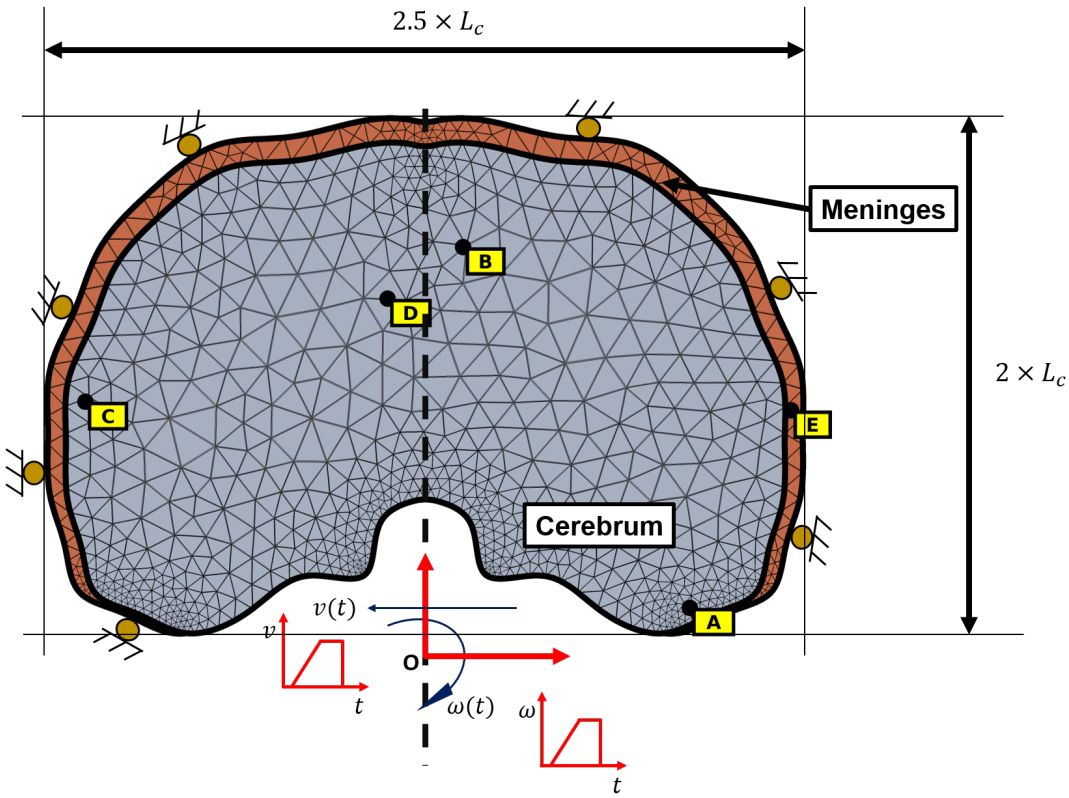

(b)

Figure 3.10: (a) A scanned central coronal section of a 188 mm long specimen of the right cerebral hemisphere of a human brain, reproduced from the study of Duvernoy (1999). The red dots in (a) indicate the data points which are used to create a 2D geometry shown in (b). The outer boundary of the cerebrum is offset by a minimum distance of 4 mm to obtain the outer domain comprising the meninges. The outer surface of the meninges is constrained by roller supports and the whole section is subjected to kinematic loading corresponding to the various kinematic loading parameters 4 listed in table 3.3. Subfigure (b) also shows the representative FE mesh comprising of 3 noded triangular plane stress elements, enclosed within the bounding box, dimensions of which are discussed in section 3.2.1. Five points of interest (A, B, ... E) are identified where the evolution of the damage parameters is studied.

minimum thickness of 1 mm, the elements are restricted to a minimum edge length of 0.08 mm. Such a measure ensures a proper mesh refinement while minimizing the computational time. An element growth rate of up to 1.3 is allowed to minimize the number of elements. Due to the use of finer elements for meshing, as shown in Fig. 3.10b, to maintain the accuracy of the solution we have reduced the maximum time step to a value of 0.01 ms. Additionally, as we do not expect as sharp gradients in the pressure evolution for a kinematic loading, as in an impulse loading, we change the time-integration scheme to an unconditionally stable implicit BDF (Backward Difference Formula) scheme, which is faster than the generalised α scheme used earlier, at the cost of introducing some numerical damping. As shown in the Fig. 3.10b, kinematic loading comprising of the translational and rotational velocities from Table 3.3 is applied on the geometry in a manner analogous to the previous sub-section. We assume that the rigid skull enclosing the brain will restrict any normal displacement, but allow a frictionless sliding at the outer layer of the meninges. Hence, we apply a sliding boundary condition throughout the outer boundary, implemented as $\mathbf{n} \cdot \mathbf{u} = 0$, where $\mathbf{n}$ is the outward normal vector at any point on the boundary. The kinematic loading parameters are the same as in case 4 listed in Table 3.3. Under these loading and boundary conditions, the equation of motion Eq.(3.1), along with the constitutive law, Eq. (3.3) is solved in COMSOL, and coupled with the calcium kinetics equations Eqs. (2.1-2.3,2.5,2.6). Since the intracellular Ca^{2+} evolution is of significance only in the cerebrum, the calcium kinetics equations are not solved for the meninges domain.

Based on the results of simulation, we identify 5 points of interest which are labelled as A, B, C, D and E in Fig. 3.10b. A is the point at which the peak intracellular Ca^{2+} concentration, c_i^{peak}, reaches the maximum value in the entire domain. At point B, c_i^{peak} is minimum. It is observed that the locations of maximum and minimum residual intracellular Ca^{2+} concentrations, c_i^{res}, coincide with that of c_i^{peak}. Points C and D are the locations where the peak local pressure attains the maximum and minimum magnitudes respectively. We have taken an additional point E, which lies in the meninges domain, where we observe the pressure evolution, but the calcium kinetics is not solved for. The local pressure evolution and the intracellular Ca^{2+} concentration evolution at these points are plotted in Fig. 3.11a and 3.11b respectively. We find that for the translational and rotational velocity values adopted from Table 3.3, the contribution of the former to the resulting stress is much higher than the latter. Hence the results wouldn't be affected much,

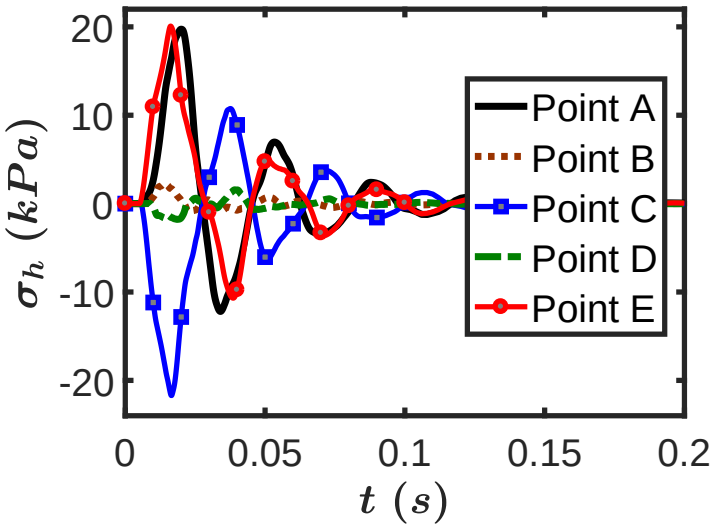

(a)

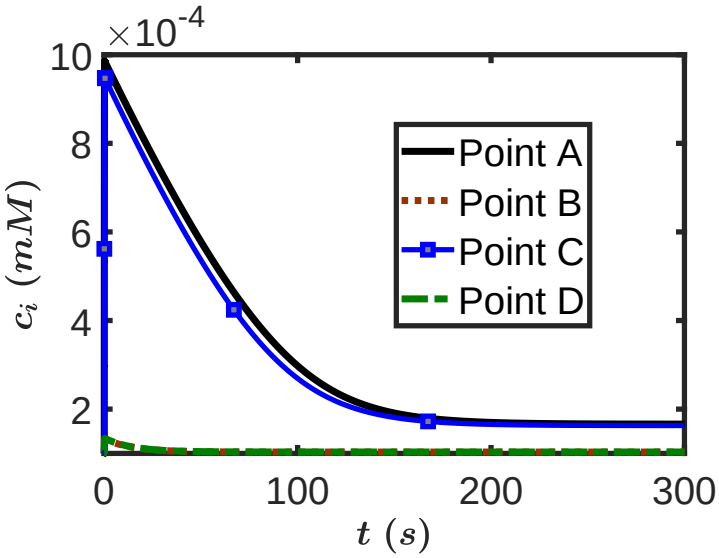

(b)

Figure 3.11: The evolution of (a) hydrostatic stress σ_h and (b) intracellular Ca^{2+} concentration c_i at the five identified points of points of interest labeled in Fig. 3.10b, under the application of kinematic loading corresponding to the loading parameters for data set 4 listed in table 4.1. Due to being located in the meninges, the Ca^{2+} evolution is not evaluated at point E.

even if only the translational velocity was used.

Reinforcing the discussion in Section 3.2.3, we again observe that the location of maximum peak pressure (point C) does not correspond to the location of maximum intracellular Ca^{2+} concentration (point A). In this case we note that the Ca^{2+} concentration evolution at the point C, the pressure reaches a magnitude of 21.3 kPa, while at point A, a peak pressure of 19.73 kPa is reached. This may indicate that point C is more critical for damage. However a higher intracellular concentration is attained at point A, indicating it to be the more probable location of secondary damage. For the point E, we note that the peak pressure reached is higher than at point A inside the cerebrum, but the Ca^{2+} concentration is irrelevant as it is located in the meninges.

3.3 Conclusion

In this chapter, we extended the calcium kinetics model by introducing a spatial dimension. We introduced the spatial dependence of the local hydrostatic stress which is evaluated by performing a transient FEM analysis on the geometry of a human brain. The non spatial calcium kinetics model is then coupled with the FEM stress results to reveal the local intracellular Ca^{2+} concentration evolution with respect to time, at any point of interest throughout the geometry. The coupled spatialised calcium kinetics model is found to be advantageous over purely FEM based mechanistic models as well as purely chemical kinetics based non-spatial model presented in Chapter 2.

The spatial Ca^{2+} kinetics model is consistent with the results of the non-spatial model, and therefore, like our previous model, reproduces qualitatively the key experimental observations (LaPlaca *et al.*, 1997; Geddes and Cargill, 2001; Geddes-Klein *et al.*, 2006; Maneshi *et al.*, 2015). As in the case of non-spatial mode, upon action of an external load the typical profile of the intracellular Ca^{2+} concentration shows an initial rapid increase. Upon removal of load, the concentration gradually settles to a residual value c_i^{res} which is higher than the homeostatic concentration. For a severe injury, i.e. for a higher magnitude or duration of the impulse load, the peak and the residual concentrations are higher. Therefore, a severe injury results in a severe secondary damage.

From the results presented in this chapter we also infer that peak kinematic or pressure measures obtained using purely mechanistic FE models may not be the precise predictors for location of secondary injuries. Unlike these, our model takes into account not only the

peak pressure values, but more significantly, the duration for which these peak pressures act. We have been able to blend both these mechanical parameters to acquire the intracellular Ca^{2+} concentration, which is directly responsible for the occurrence of secondary damage in the brain tissue. We believe that thus obtained intracellular Ca^{2+} concentration is a more definitive indicator of secondary injuries. We further assert that this significant parameter is obtained at a virtually insignificant computational cost over the FEM analysis.

Chapter 4

Stress Dependent Tau Phosphorylation

4.1 Calpain-I Activation

As discussed in the section 1.3, excessive Ca^{2+} accumulation in the neurons has been implicated in the activation of calpain enzyme. Of the two forms of calpain ubiquitously expressed in a human neuron, calpain-I has a much lower Ca^{2+} requirement for its activation as compared to calpain-II, and is hence more severely implicated in the downstream proteolysis of essential proteins during tauopathies (Ferreira and Bigio, 2011; Jin *et al.*, 2015; Kurbatskaya *et al.*, 2016). Following this observation, we explicitly base our model on activation of calpain-I only. Assuming a single step reaction for calpain activation by accumulated Ca^{2+}, we can write the corresponding mass action kinetics as,

$$\frac{d[Cal_A]}{dt} = k_f c_i^n [Calp] - k_r [Cal_A] \tag{4.1}$$

where, k_f and k_r are the forward and reverse rate constants respectively, n is the Hill's constant corresponding to number of Ca^{2+} ions binding on a single molecule of calpain, c_i is the instantaneous intracellular Ca^{2+} concentration, while $[Calp]$ and $[Cal_A]$ denote the concentrations of calpain and activated calpain respectively. Conserving the total amount of calpain molecules in the system, we can express the rate of calpain activation as,

$$\frac{d[Cal_A]}{dt} = k_f [Calp]_0 \left\{ c_i^n - \frac{[Cal_A]}{[Calp]_0} \left(c_i^n + K_{1/2}^n \right) \right\} \tag{4.2}$$

where, $[Calp]_0$ is the initial calpain concentration, and $K_{1/2}$ is the Ca^{2+} concentration required for half maximal calpain activation, defined in terms of the forward and reverse

rate constants as, $K_{1/2} = (k_r/k_f)^{1/n}$. The procedure to estimate k_f, $K_{1/2}$ and $[Calp]_0$ will be discussed in the section 4.4.

A calpain molecule comprises of a large catalytic subunit, consisting of four domains (dI-dIV) and a small regulatory subunit with two domains (dV,dVI). Domains IV and VI form the C terminal of their respective subunits, and contain five EF-hand motifs each, which provide multiple sites for Ca^{2+} to bind cooperatively (Dutt *et al.*, 2000; Khorchid and Ikura, 2002; Suzuki *et al.*, 2004; Ono and Sorimachi, 2012). Additionally, the domain II of the large subunit, the cysteine protease core domain (CysPc), itself contains two highly cooperative binding sites for Ca^{2+} (Moldoveanu *et al.*, 2002; Khorchid and Ikura, 2002; Moldoveanu *et al.*, 2004; Suzuki *et al.*, 2004; Ono and Sorimachi, 2012). A multistep process has been hypothesised for calpain activation by Ca^{2+}. As a first step Ca^{2+} binding at, at least three of the five, EF sites of dIV and dVI creates subtle conformational changes leading to opening of the circular arrangement of the domains via removal of helical anchor between dI and dVI, and the dissociation of the small subunit from the large subunit. These changes release the tension in the protease core, allowing Ca^{2+} binding to occur in dII (Moldoveanu *et al.*, 2002; Khorchid and Ikura, 2002; Moldoveanu *et al.*, 2004; Suzuki *et al.*, 2004). This mechanism indicates that atleast 6 binding sites are operational with a high degree of co-operativity during the calpain activation process. Although calpain activation is a multistep process, the lack of observation of intermediary species indicates a much lower time scale involved in the binding process compared the time scale involved in the proteolytic activity of the activated calpain. This justifies our simplification of the complex multistep process into a single step reaction given by equations (4.1 - 4.2).

Given k_f, $K_{1/2}$, $[Calp]_0$, the calpain kinetics equation (4.2) solved simultaneously with the calcium kinetics equations (2.1-2.3,2.5) allows us to predict the calpain activation following the application of an external hydrostatic stress.

4.2 Calpain Mediated Kinase Truncation

Activated calpain-I can mediate tau hyperphosphorylation via several pathways most implicated of which are the increased activities of CDK5 and GSK-3β kinases. Although CDK5 activity may increase in response to calpain activation, in vivo evidence for CDK5 being responsible for tau hyperphosphorylation in an AD affected brain is lacking (Patrick

et al., 1999; Kusakawa *et al.*, 2000; Lee *et al.*, 2000; Nath *et al.*, 2000; Engmann and Giese, 2011; Kimura *et al.*, 2014). On the other hand, the GSK-3β truncation correlates with tau hyperphosphorylation in an AD affected brain (Jin *et al.*, 2015; Baudry and Bi, 2016; Kurbatskaya *et al.*, 2016). Similarly in a human TBI, the injury severity is found to correlate with increased activity of GSK-3β (Yang *et al.*, 2017; Kulbe and Hall, 2017). Upon exposure to calcium, GSK-3β in human brain extracts is cleaved via a calpain mediation (Goñi-Oliver *et al.*, 2007, 2009; Ma *et al.*, 2012; Jin *et al.*, 2015). Ample evidence is available in literature to implicate calpain in the GSK-3β truncation (Goñi-Oliver *et al.*, 2007, 2009, 2011; Feng *et al.*, 2013; Jin *et al.*, 2015; Baudry and Bi, 2016). Goñi-Oliver *et al.* (2007, 2009) performed a quantitative kinetic assay of the N-terminated GSK-3β cleavage product, ΔN-GSK-3β, and reported that its generation is a two step process - the first step generating the larger (40 kDa) fragment F_1, and the second step a smaller (30 kDa) fragment F_2. Accordingly, we model the two step GSK-3β truncation process by writing the chemical reactions as,

$$\mathrm{Cal_A} + \text{GSK-3}\beta \underset{k^G_{-1}}{\overset{k^G_1}{\rightleftharpoons}} \mathrm{F_1}$$

$$\mathrm{Cal_A} + \mathrm{F_1} \underset{k^G_{-2}}{\overset{k^G_2}{\rightleftharpoons}} \mathrm{F_2}$$

where k^G_1 (k^G_{-1}) and k^G_2 (k^G_{-2}) are the forward (reverse) reaction constants for the formation of truncation products F_1 and F_2 respectively. The rate equations for GSK-3β, F_1 and F_2 based on the above chemical reactions are,

$$\begin{aligned}
\frac{d\mathcal{X}_G}{dt} &= -k^G_1[Cal_A]\mathcal{X}_G + k^G_{-1}\mathcal{X}_{F1} \\
\frac{d\mathcal{X}_{F1}}{dt} &= k^G_1[Cal_A]\mathcal{X}_G - \left\{k^G_{-1} + k^G_2[Cal_A]\right\}\mathcal{X}_{F1} + k^G_{-2}\mathcal{X}_{F2} \\
\frac{d\mathcal{X}_{F2}}{dt} &= k^G_2[Cal_A]\mathcal{X}_{F1} - k^G_{-2}\mathcal{X}_{F2}
\end{aligned} \tag{4.3}$$

where, χ_G = [GSK-3β]/G_0, $\chi_{F1} = [F_1]/G_0$ and $\chi_{F2} = [F_2]/G_0$ respectively represent the relative fractions of the instantaneous concentrations of full length GSK-3β, and its fragments F_1 and F_2 with respect to G_0, the initial concentration of GSK-3β. Equation (4.3) predicts the time dependent generation of the N-truncated GSK-3β fragments (ΔN-GSK-3β) if the time dependent concentration of activated calpain is known. Reports suggest that GSK-3β in human brain extracts can be cleaved at N-terminal and/or at the C-terminal upon exposure to calcium (Goñi-Oliver *et al.*, 2007; Ma *et al.*, 2012; Jin *et al.*,

2015). Analogous to ΔN-GSK-3β, the truncation products ΔC-GSK-3β, and ΔN/ΔC-GSK-3β too show an increased activity and significantly contribute in tau phosphorylation. But our model (equations (4.3)) is solely based on ΔN-GSK-3β fragmentation due to lack of availability of kinetic data on generation of ΔC-GSK-3β, and ΔN/ΔC-GSK-3β fragments.

4.3 Tau Phosphorylation/Dephosphorylation

Tau proteins have around 30 phosphorylable sites, of which about 10 sites are known to be hyperphosphorylated in vivo by GSK-3β (Gong *et al.*, 2005; Liu *et al.*, 2006; Jin *et al.*, 2015; Stepanov *et al.*, 2018). In the post-mortem AD brain NFT P-tau aggregates, in all only 5-9 moles of phosphate per mole of P-tau are seen (Ksiezak-Reding *et al.*, 1992; Köpke *et al.*, 1993; Iqbal *et al.*, 2009), suggesting that not all of the available sites may be phosphorylated. In other words, of 2^{10} possible combinations of tau phosphorylation states, around 200 possible states are usually seen in an AD affected brain. These observations indicate a massively combinatorial nature of the phosphorylation/dephosphorylation phenomena which an explicit and deterministic model will most likely be inadequate to capture. Indeed, rule based approaches like agent based modeling have been used in literature to simulate such biological interactions, primarily at the scale of few tau proteins. For instance, Stepanov *et al.* (2018) developed a probablistic model for tau phosphorylation/dephosphorylation assuming mutual independence at the sites of interest. However extrapolation of these stochastic models to the scale of MT bundle is not straightforward. A single 4 μm long MT bundle in an axon can have 10-100 MTs arranged with a tau protein spacing of $\sim$ 20 nm (Peter and Mofrad, 2012; Ahmadzadeh *et al.*, 2014) leading to a total of around 10000 tau proteins. Instead of a probabilistic study of such a huge sample space, we propose a simplified averaged model by making an additional assumption that *the phosphorylation at each distinct site of tau protein follows the same average kinetics*. We assert that a numerically averaged kinetics over all the phosphorylation sites can be found experimentally despite the known site specific kinetics for both phosphorylation and dephosphorylation (Liu *et al.*, 2005, 2006; Jin *et al.*, 2015). Thus, instead of observing how many tau proteins are being phosphorylated, we study the phosphorylation/dephosphorylation occurring at any individual site, and compute the average number of sites of tau which are being phosphorylated/dephosphorylated. We do so by consider-

ing the phosphorylation at any single site of tau by full length GSK-3β, initial and final truncation products F_1 and F_2 through the following reactions respectively,

$$\text{GSK-3}\beta + \mathbb{P} \xrightarrow{k_f^\tau} \mathbf{P},$$
$$\text{F}_1 + \mathbb{P} \xrightarrow{k_f^\tau} \mathbf{P},$$
$$\text{F}_2 + \mathbb{P} \xrightarrow{k_t^\tau} \mathbf{P},$$

In these reactions, as well as elsewhere in the article, '$\mathbb{P}$' and '**P**' denote an unphosphorylated (vacant) and phosphorylated (occupied) site respectively. The symbols above the arrow indicates the reaction rate for each of the reaction. The reaction rate constant for the first two reactions is assumed to be same for the lack of enough data and to limit the number of parameters in the model. The final truncated kinase product F_2 has a higher phosphorylation activity towards tau as compared to the full length kinase.

If $\mathcal{S}$ and $\mathcal{N}$ signify the total number of sites and average number of occupied sites per tau protein and $[\text{tau}]_0$ corresponds to the total concentration of all tau protein whether phosphorylated or not, then the total number of phosphorylated $\text{N}_\mathbf{P}$ and unphosphorylated $\text{N}_\mathbb{P}$ sites in the system per unit volume are,

$$\text{N}_\mathbf{P} = \mathcal{N} \cdot [\text{tau}]_0, \qquad \text{N}_\mathbb{P} = (\mathcal{S} - \mathcal{N}) \cdot [\text{tau}]_0 \tag{4.4}$$

Based on the phosphorylation reactions and equation (4.4), rate of increase in the average number of occupied sites is,

$$\left(\frac{d\mathcal{N}}{dt}\right)_+ = k_f^\tau G_0 \left\{ \mathcal{X}_G + \mathcal{X}_{F1} + \frac{k_t^\tau}{k_f^\tau}\mathcal{X}_{F2} \right\} (\mathcal{S} - \mathcal{N}) \tag{4.5}$$

where G_0 is the initial concentration of GSK-3β kinase in the system.

The dephosphorylation phenomena of tau proteins by phosphatases like PP2A have been experimentally observed to follow a Micheles Menten kinetics with a Hill's coefficient of 1 (Liu *et al.*, 2005) given as,

$$\frac{d\text{N}_\mathbf{P}}{dt} = -\frac{V_{max}\text{N}_\mathbf{P}}{K_m + \text{N}_\mathbf{P}} \tag{4.6}$$

where V_{max} is the maximal rate of phosphorylation and K_m is the average site occupancy at which a half maximal phosphorylation rate is attained. Using equation (4.4), equation (4.6) can be rewritten to obtain the rate of decrease in average number of occupied sites as,

$$\left(\frac{d\mathcal{N}}{dt}\right)_{-} = -\frac{V_{de}\mathcal{N}}{K_{de} + \mathcal{N}} \tag{4.7}$$

where, $V_{de} = V_{max}/[tau]_0$ and $K_{de} = K_m/[tau]_0$. The overall rate at which the average number of occupied sites per tau protein changes due to the combined action of phosphorylation by GSK-3β and its truncated products (equation 4.5) as well as dephosphorylation by PP2A (equation 4.7), is,

$$\frac{d\mathcal{N}}{dt} = k_f^{\tau} G_0 \left\{ \mathcal{X}_G + \mathcal{X}_{F1} + \frac{k_t^{\tau}}{k_f^{\tau}} \mathcal{X}_{F2} \right\} (\mathcal{S} - \mathcal{N}) - \frac{V_{de}\mathcal{N}}{K_{de} + \mathcal{N}} \tag{4.8}$$

Through the set of equations (2.1-2.5, 4.2, 4.3, 4.8) we have built a mathematical framework that allows us to predict the local intracellular Ca^{2+} evolution, the resulting calpain activation, GSK-3β truncation and tau phosphorylation behaviour, if the evolution of local hydrostatic stress at any point of interest is known.

4.4 Estimation of parameters

Equation (4.2) governing the calcium mediated calpain activation demands the knowledge of parameters n, $K_{1/2}$ and k_f. The reasoning behind the selection of values listed in Table 4.1 is as follows: Out of the two kinds of calpain, Calpain-II is reported to bind Ca^{2+} with a Hill's coeffiecient of 5 (Dutt *et al.*, 2000). As discussed in the section **"Calpain Activation"**, Calpain-I is known to possess at least 6 Ca^{2+} binding sites with a very high degree of cooperativity. In fact, a Hill's coefficient of 1.8 has been reported for the non EF hand site of Calpain-I towards Ca^{2+} (Moldoveanu *et al.*, 2002, 2004). Based on these observations and qualitative similarity in functioning and structures of Calpain-I and II, we assume a common value of n = 5 as Hill's coefficient for binding Ca^{2+}.

The autolysis of calpain-I occurring in parallel to its activation, and additional presence of phospholipids reduce the in vivo requirement of Ca^{2+} for half maximal calpain activity ($K_{1/2}$) below the observed in vitro value. Hence based on the reported range of 0.6-2 μM (Cong *et al.*, 1989; Andrea *et al.*, 1996), we assume Ca^{2+} requirement for half maximal activation to be 1.5 μM. Equation (4.2) reveals the time constant τ_{calp} for calpain activation to be, $1\Big/\left\{k_f\left(c_{i,hom}^n + K_{1/2}^n\right)\right\}$. Since calpain mediated breakdown products from different protein substrates are seen within 2-10 minutes of calcium infusion (Andrea *et al.*, 1996; Zhao *et al.*, 1998; Büki *et al.*, 1999; Czogalla and Sikorski, 2005) τ_{calp} is

Table 4.1: Value of Parameters

	Parameter	Definition	Value
Calpain Activation	$K_{1/2}$	c_i for half maximal activation	1.5μM
	n	Hill Coefficient	5
	k_f	Forward Rate Constant for activation	$4.3896 \times 10^{-4}\mu\text{M}^{-5}\text{s}^{-1}$
	$[Calp]_0$	Homeostatic Calpain concentration	0.1μM
GSK-3β Truncation	k_1^G	Forward rate constant for truncation step 1	$3.312\mu\text{M}^{-1}\text{s}^{-1}$
	k_{-1}^G	Reverse rate constant for truncation step 1	0.0086s^{-1}
	k_2^G	Forward rate constant for truncation step 2	$1.121\mu\text{M}^{-1}\text{s}^{-1}$
	k_{-2}^G	Reverse rate constant for truncation step 2	0.0035s^{-1}
Tau Phosphorylation/ Dephosphorylation	k_f^τ	Reaction Rate for Tau Phosphorylation by full length [GSK-3β]$_0$	$k_f^\tau G_0 = 9.6282 \times 10^{-5}\text{s}^{-1}$
	G_0	Homeostatic concentration of GSK-3β	
	k_t^τ	Reaction Rate for Tau Phosphorylation by truncated product F_2	$k_t^\tau / k_f^\tau = 29.292$
	V_{de}	Maximal tau dephosphorylation rate	$3.2615 \times 10^{-3}\text{s}^{-1}$
	K_m	Total tau concentration for half maximal dephosphorylation	11.6μM
	$[tau]_0$	Total tau concentration in neuron	4.36μM
	$\mathcal{S}$	Number of sites on each tau protein	10

assumed to be 5 minutes leading to the forward rate constant $k_f = 4.3896 \times 10^{-4}\ \mu\text{M}^{-5}\text{s}^{-1}$. The values used for the kinetic constants involved in calpain activation are listed in Table 4.1.

An experimental time evolution of calpain activation from a kinetic assay study would be ideal to validate the model. In absence of any such data in literature, to the best of our knowledge, the correctness of the kinetic parameters chosen for calpain activation in Eq. (4.2) is assessed through two checks. Firstly, Eq. (4.2) yields the fraction of calpain activated under homeostatic condition as $c^n_{i,hom} \Big/ \left\{c^n_{i,hom} + K^n_{1/2}\right\} \sim 10^{-6}$, which concurs with the inactivity exhibited by calpain under an undisturbed homeostatic condition (Andrea *et al.*, 1996; Ono and Sorimachi, 2012). The second check involves the time span of the presence of activated calpain and its peak value due to loading incurred during TBI. In conformation with the repeated impulse loads of millisecond duration felt by brain during TBI (Maneshi *et al.*, 2015; Nusholtz *et al.*, 1984), we consider an idealized load of 5 repeated stress impulses, each of magnitude 10 kPa and duration of 10 ms and a resting period of 50 ms between each successive impulse (see the inset of Fig. 4.1a) as input to our model. Fig. 4.1a shows the evolution of intracellular Ca^{2+} (shown using red colored solid line) and the time course of calpain activation (shown using blue colored dashed line) based on the solution of the calcium kinetics (Equations 2.1-2.3,2.5) along with the calpain activation kinetics (Equation (4.2)) for the parameters listed in Table 2.1 and Table 4.1. As seen in Fig. 4.1a, calpain-I activity is significant only for ~ 20-30 minutes after the application of load, in agreement with the experimental observations of notable increase in the activation of calpain-I and formation of calpain specific proteolysis products within 15 minutes (Kampfl *et al.*, 1996; Büki *et al.*, 1999) and 30 minutes (Büki *et al.*, 1999; Serbest *et al.*, 2007) of injury respectively. Considering homeostatic calpain concentration $[Calp]_0$ as 0.1 μM (Kilinc, 2008; Palecek *et al.*, 1999), the peak value of activated calpain $[Cal_A]$ noted from Fig. 4.1a is approximately 1.7 nM which falls within the range 1-20 nM generally adopted as calpain concentration in the experiments involving in vivo calpain activities (Frangié *et al.*, 2006; Goñi-Oliver *et al.*, 2007; Jin *et al.*, 2015).

The kinetic parameters involved in the GSK-3β truncation model (Equation (4.3)) are obtained by benchmarking the model prediction against the experimental data of Goñi-Oliver *et al.* (2007) who studied the N-terminal truncation of GSK-3β by calpain and reported the relative concentrations of the full length (GSK-3β) and the truncated products (Fragment 1, Fragment 2) with respect to the time allowed for calpain treatment.

The experiments made use of 0.2 units/ml (~13.4 nM[1])) of calpain in presence of 5 mM $CaCl_2$ to achieve an immediate and total activation of calpain allowing us to circumvent the evolution of calpain activation and assume that activated calpain concentration stays constant throughout the process. The correctness of the finalized parameters listed in Table 4.1 can be gauged through the excellent comparison between the model prediction and experiments of Goñi-Oliver *et al.* (2007) as displayed in Figure 4.1b.

The kinetic parameter $k_f^\tau G_0$ in equation (4.5) associated with GSK mediated tau phosphorylation is decided based on the experiment of Liu *et al.* (2006) which report the time dependent increase in tau phosphorylation levels of PKA prephosphorylated tau upon subsequent phosphorylation by untruncated GSK. The in vivo increase in susceptibility of tau to GSK mediated phosphorylation in the presence of PKA (Wang *et al.*, 1998; Liu *et al.*, 2004) is captured tacitly through the term $k_f^\tau G_0$ in our model. For its value listed in Table 4.1, the comparison between the prediction based on equation (4.5) and experimental data of Liu *et al.* (2006) is shown in Fig. 4.1c. The parameter k_t^τ/k_f^τ in equation (4.5) is calibrated by employing the work of Jin *et al.* (2015), where the phosphorylation of individual tau sites by GSK-3β and its truncated products. As our model and equation (4.5) assumes same average kinetics to hold at all sites, we extrapolate the site-specific result of Jin *et al.* (2015) for the site Ser-199 to hold good in an average sense and represent overall tau protein phosphorylation. We are aware of the approximation but persist with it owing to lack of additional experiments to obtain a suitable average kinetics. Ser-199 in particular is chosen as it is always found to be phosphorylated by GSK-3β and its truncation products, as well as dephosphorylated by PP2A (Liu *et al.*, 2004; Jin *et al.*, 2015; Liu *et al.*, 2005). Following Jin *et al.* (2015), 2 nM activated calpain is allowed to truncate GSK for 10 minutes through GSK truncation kinetics equation (4.3). The resultant concentration of GSK-3β and its truncation products are fed as input to equation (4.5) and the parameter k_t^τ/k_f^τ is sought to ensure a good match between the model result and observations of Jin *et al.* (2015). The comparison can be seen in Fig. 4.1d and the corresponding value of k_t^τ/k_f^τ is noted in Table 4.1. It may be noted that in this procedure the in vivo homeostatic concentration of GSK-3β (G_0) is a parameter not readily available, hence we have combined $k_f^\tau G_0$ as a single parameter. It should also be pointed out that we are using the in vitro kinetics to calibrate the in vivo kinetics parameters. However, the use of recombinant GSK obtained from lyzed HEK-293FT cells in the experiments, with

[1]Based on specific activity of calpain used by Goñi-Oliver *et al.* (2007) (Merck, catalogue# 208718)

concentrations within physiological range allow us to do so as a first approximation.

The correctness of parameters associated with Equation (4.5) is checked against another set of studies by Jin *et al.* (2015) where the GSK-3β truncation by 1nM calpain-I is allowed to proceed for different times and the subsequent kinase activity is recorded. The same study is carried in silico using equations (4.3) and (4.5) of our model and parameters listed in Table 4.1 to generate the time variation of relative kinase activity between the full length kinase, and its truncation products. The result predicted by model and plotted in Fig. 4.1e is qualitatively similar to the result of Jin *et al.* (2015) and succeeds in capturing the increase in the kinase activity post truncation. However the experiments predict that the relative activity doubles in ~30 min (Jin *et al.*, 2015) while our model predicts that it will triple in ~20 min. The quantitative dissimilarity can be attributed to the fact that the model calibration made use of the work of Goñi-Oliver *et al.* (2007) based on N-truncation of GSK-3β while the work of Jin *et al.* (2015) which forms the basis of Fig. 4.1e is based on C-terminal truncation of GSK-3β.

The parameters V_{de} and K_{de} in Equation (4.7) associated with tau dephosphorylation via phosphates like PP2A are extracted through the in silico simulation of experiments of Liu *et al.* (2005). The parameter K_m is chosen equal to 34.8 based on the result of Liu *et al.* (2005) where in-vitro half maximal PP2A mediated dephsphorylation of tau proteins containing 3 occupied sites occurs at a tau concentration of 11.6 μM. The parameter V_{de} is calibrated by matching the prediction of Equation (4.7) with the kinetic assay of percentage tau dephosphorylation at Ser-199 with time, as reported by Liu *et al.* (2005). The comparison is shown in Fig. 4.1f and the corresponding value of V_{de} is mentioned in Table 4.1. Following the experiment by Liu *et al.* (2005), $[\tau_0] = 4.36\mu$M (Table 4.1) is adopted during the calibration procedure which is quite reasonable as it falls within the physiological range 2-10μM (Liu *et al.*, 2005; Iqbal *et al.*, 2009). We would like to reiterate the usage of site specific experimental data for calibration of site independent model, assuming the average phosphorylation kinetics at all the sites. Lastly, we would like to point out that the parameter estimation carried out in this section is specific to the currently available experimental results against which calibration or validation was carried out. In order to validate the parameter estimation procedure, the sensitivity of the model to the parameters is carried out in Appendix D.

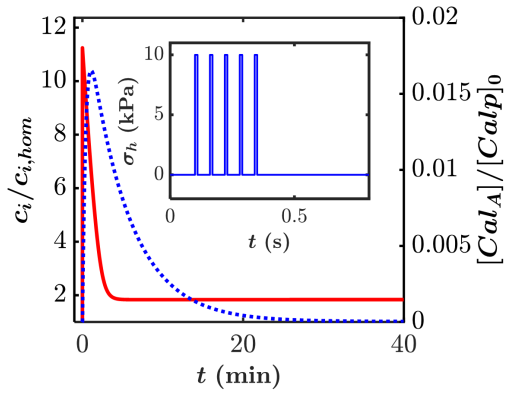
$c_i/c_{i,hom}$
$[Cal_A]/[Calp]_0$
σ_h (kPa)
t (s)
t (min)

(a)

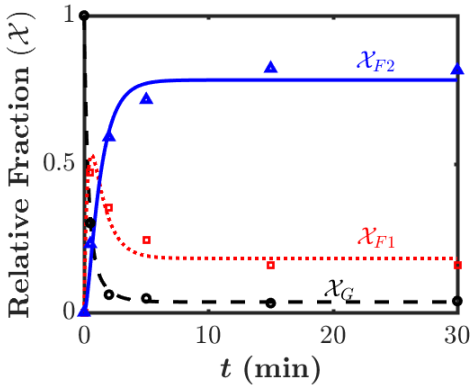
Relative Fraction ($\mathcal{X}$)
$\mathcal{X}_{F2}$
$\mathcal{X}_{F1}$
$\mathcal{X}_G$
t (min)

(b)

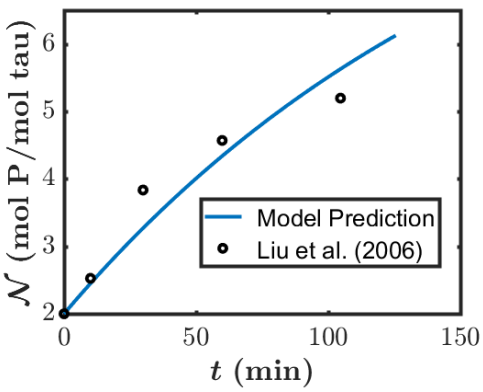
$\mathcal{N}$ (mol P/mol tau)
Model Prediction
Liu et al. (2006)
t (min)

(c)

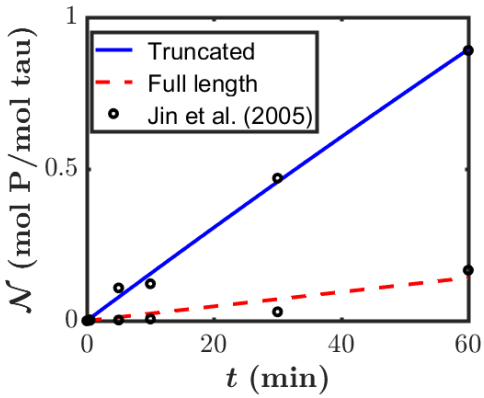
$\mathcal{N}$ (mol P/mol tau)
Truncated
Full length
Jin et al. (2005)
t (min)

(d)

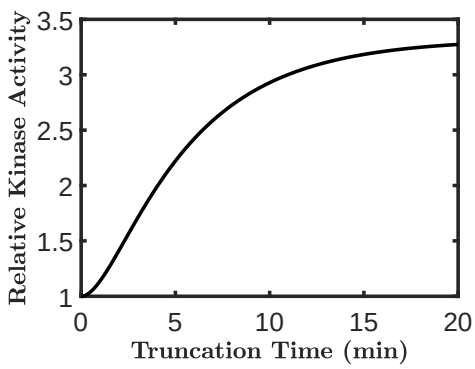
Relative Kinase Activity
Truncation Time (min)

(e)

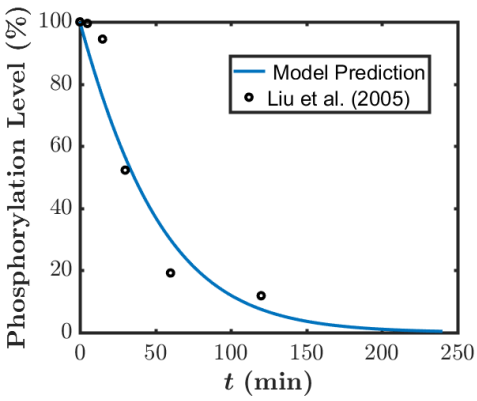
Phosphorylation Level (%)
Model Prediction
Liu et al. (2005)
t (min)

(f)

Figure 4.1: The parameters involved in equations (4.2,4.3 and 4.8) are estimated by calibrating the model to experiments reported in literature. (a) The time dependent evolution of normalized Ca^{2+} concentration ($c_i/c_{i,hom}$) in red solid line, and fraction of calpain activated ($[Cal_A]/[Calp]_0$) in blue dashed line, when a repeated stress impulse as shown in the inset is applied. (b) Comparison of the evolution of relative fractions of GSK-3β and its truncation products F_1 and F_2 using the calibrated values of kinetic parameters (noted in Table 4.1) in Equation (4.3) with the experimental observations of Goñi-Oliver *et al.* (2007) denoted by markers. (c) Comparison of the evolution of GSK-3β mediated phosphorylation of PKA prephosphorylated tau predicted by equation (4.5) using the calibrated value of $k_f^\tau G_0$ (noted in Table 4.1) with the values reported by Liu *et al.* (2006). (d) Comparison of the extent of phosphorylation by full length and truncated GSK-3β predicted via equation (4.5) using the calibrated value k_t^τ/k_f^τ (noted in Table 4.1) with the experimental values reported by Jin *et al.* (2015). (e) Relative increase in the GSK-3β phosphorylation activity towards tau based on Equations (4.3) and (4.5) after the truncation of in-silico incubation with 1nM calpain-I at various times (f) Comparison of the temporal decay of tau dephosphorylation by PP2A computed through equation (4.7) using the calibrated values of parameters V_{de}, K_{de} (noted in Table 4.1) with the corresponding experimental result of Liu *et al.* (2005).

4.5 Results And Discussion

4.5.1 Homeostatic Behavior

In our discussion on the linear stability of the non spatial calcium kinetics model (Section 2.2) we have established that in absence of any external mechanical stress, the calcium kinetics model (Eqs. (2.1-2.3)) is inherently stable, such that there is no net Ca^{2+} transport across either the PM or ER membranes. Therefore no Ca^{2+} accumulation occurs in absence of any external mechanical stress, and homeostasis is maintained. The calpain kinetics parameters have also been estimated so as to permit a negligible calpain activation unless Ca^{2+} accumulation occurs. As discussed in Section 4.4, under a homeostatic Ca^{2+} concentration, the fraction of calpain activated is only $\sim 10^{-6}$. Following a negligible calpain activation, equation (4.3) and the associated GSK-3β truncation kinetics parameters listed in table 4.1 ensure that a negligible fraction ($\sim 10^{-9}$) of GSK-3β is truncated, allowing it to remain as a full length kinase. Under homeostatic conditions there is some phosphorylation of tau which allows it to promote MT assembly (Iqbal *et al.*, 2009). Post mortem analysis on a normal human brain reveals an average phosphorylation levels

of 2-3 moles of phosphate per mole of tau (Köpke *et al.*, 1993; Gong *et al.*, 2005; Liu *et al.*, 2006; Iqbal *et al.*, 2009). The activities of kinase and phosphatases are balanced in vivo to maintain the homeostatic phosphorylation levels, according to which the phosphorylation/dephosphorylation kinetics model (equation (4.8), implies $d\mathcal{N}/dt = 0$. The average number of occupied sites per mole of total tau at homeostasis $\mathcal{N}_h$ is thus obtained as the root of the following quadratic equation in terms of kinetic parameters governing tau phosphorylation and dephosphorylation,

$$\mathcal{N}_h^2 + \left(\frac{V_{de}}{k_f^\tau G_0} + K_{de} - \mathcal{S}\right)\mathcal{N}_h - K_{de}\mathcal{S} = 0. \tag{4.9}$$

Substituting the parameter values listed in table 4.1 in equation (4.9), the computed phsophorylation level $\mathcal{N}_h = 2.33$ is well within the range of 2-3 mol phosphates per mole of tau observed in human brain (Köpke *et al.*, 1993; Gong *et al.*, 2005; Liu *et al.*, 2006; Iqbal *et al.*, 2009). The reasonable value of $\mathcal{N}_h$ vindicates the calibration procedure and appropriateness of parameter values.

In absence of any external mechanical loads, the model response is summarized as follows,

- homeostatic intracellular Ca^{2+} concentration is maintained,
- negligible calpain activation occurs,
- GSK-3β exists in its full length form without getting truncated.
- The tau phosphorylation is maintained at a homeostatic level of $\mathcal{N}_h = 2.33$ molP/mol total tau.

The next section analyzes the response of our model to an external load.

4.5.2 Behavior Under Mechanical Loading

Following a TBI, different parts of the human brain experience a series of stress/strain impulses of varying magnitudes and duration until they dissipate due to the viscous nature of the brain tissue. For the purpose of experiments on brain tissue samples, such loads have been idealised in the form of single or repeated rectangular pressure impulses (Geddes and Cargill, 2001; Geddes-Klein *et al.*, 2006; Maneshi *et al.*, 2015). Due to the

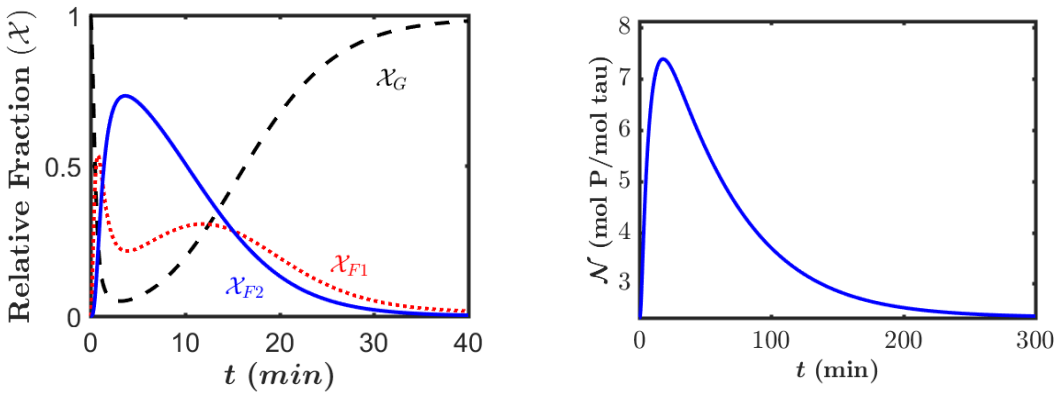

(a) **(b)**

Figure 4.2: The time evolution of (a) GSK-3β kinase truncation by activated calpain, and (b) tau phosphorylation levels, upon application of a repleated impusle comprising of 5 rectangular impulses each of magnitude 10 kPa, and duration of 10 ms, as shown in the inset of Fig 4.1a.

smallness of the experimental samples, the state of stress is almost homogeneous and the spatial dimension is inconsequential. Hence as shown in Chapter 3, a non spatial model is sufficient to capture the neurochemical kinetics observed in tissue level experiments. Consequently as a first step, we consider an idealized mechanical load comprising of 5 repeated rectangular pressure impulses, with each impulse of magnitude 10 kPa, duration 10 ms, and a resting period of 50 ms between each successive impulse, as shown in the inset of Fig. 4.1a to be the input hydrostatic stress σ_h for non-spatial version of our model. We numerically solved equations (Eqs. 2.1-2.3,2.5, 4.2, 4.3, and 4.8) for time dependent changes in Ca^{2+} concentration, calpain activation, GSK-3β truncation and tau phosphorylation/dephosphorylation adopting the parameters listed in tables 2.1 - 4.1. The resultant intracellular Ca^{2+} evolution and the time dependent activation of calpain-I are shown using solid and dotted lines respectively in Fig. 4.1a. The intracellular Ca^{2+} concentration is seen to increase to approximately 11 times the homeostatic value immediately after the action of the pressure impulses. The increased Ca^{2+} results in a calpain activation albeit with a small delay, permitting a peak activated calpain fraction of 0.0167 ($[Cal_A]_{peak} = 1.67\times10^{-3}\mu$M) approximately 2 minutes after the application of mechanical load as shown in Fig. 4.1a. The increased calpain activation is sustained up to $\sim$ 30 min after the load application. Activated calpain in turn leads to truncation of GSK-3β kinase progressively into fragments F_1 and F_2. Figure 4.2a shows the evolution of relative frac-

Table 4.2: Value of kinematic parameters for the applied impulse (Nusholtz *et al.*, 1984)

Case No.	Peak Linear Velocity (m/s)	Peak Angular Velocity (rad/s)	Peak Linear Acceleration (m/s^2)	Peak Angular Acceleration (rad/s^2)	Impulse time (ms)
1	4.5	30	420	3900	25
2	7	28	1900	7250	10
3	3.8	30	1350	7500	12

tions of full length kinase and its truncation products F_1 and F_2 with time. In early stage the fraction of truncated products increases with time due to ready availability of activated calpain. However once the activated calpain becomes limited, the formation of truncation products can no longer be sustained and the full length kinase stays untruncated. It can be noted that the GSK-3β truncation follows a similar time scale as calpain activation. This is expected due to the similar time scales in the experimental observations of Goñi-Oliver *et al.* (2007) which as noted earlier is the basis for the parameters deciding the time scale in the GSK-3β truncation equation (4.3). It is possible that in the case of a C-terminal truncation not dealt here the time scale may differ. The fragmented kinase available in the short time span interacts with tau proteins resulting in a higher level of phosphorylation as shown in Fig. 4.2b. It can be seen that the average number of occupied sites per mole of total tau ($\mathcal{N}$) increases from its homeostatic value ($\mathcal{N}_h = 2.33$) to a peak value $\mathcal{N}_{peak}$. With the progression of time, as the availability of the more active truncation products decreases, the dephosphorylation effects of PP2A phosphatase dominates and reduces $\mathcal{N}$ back to $\mathcal{N}_h$. This restoration occurs slowely and higher levels of phosphorylated tau sites are seen till ~200 min (3.5 hours) after the applied pressure load. Thus we note that the time scale of tau phosphorylation/dephosphorylation is much higher as compared to the time scales of calpain activation and kinase truncation, a fact also ascertained by the experimental observations of Liu *et al.* (2005, 2006); Jin *et al.* (2015).

In order to introduce spatial dependence in the present work, analogous to our discussion in section 3.2.6, we assume that the neurochemical kinetics equation are applicable at every material point of a continuum. Depending upon the temporal variation of hydrostatic stress at any material point, the Ca^{2+}, calpain, GSK-3β truncation and tau phosphorylation would proceed according to equations (Eqs. 2.1-2.3,2.5, 4.2, 4.3, and 4.8). A spatial model allows us to assess the effect of inhomogeneous stress distribution while accounting for realistic loading, geometry and material response on the secondary dam-

Table 4.3: Calpain Activation and Tau phosphorylation for the points experiencing maximum, minimum and intermediate hydrostatic stress for the three loading cases shown in Table 4.2

Case No.	Point of interest	$c_i^{peak}/c_{i,hom}$	$[Cal_A]^{peak}$ (nM)	$\mathcal{N}^{peak}$ (mol P/mol tau)
1	1Max	11.7781	2.215	3.2870
	1Int	12.2314	2.853	3.7153
	1Min	1.4057	1.582×10^{-4}	2.3345
2	2Max	12.6977	4.092	4.5590
	2Int	6.4205	0.047	2.3351
	2Min	1.17688	1.144×10^{-4}	2.3345
3	3Max	10.7455	1.191	2.6693
	3Int	7.4364	0.112	2.3379
	3Min	1.2136	1.46×10^{-4}	2.3345

age. To test our present model, we have taken recourse to the experiments of Nusholtz *et al.* (1984), where kinematic response of human brain was recorded. We have simulated the experiment by creating a 2D finite element method (FEM) based structural model of a human brain with linear viscoelastic properties, on which we applied the kinematic load in the form of translation and/or rotational acceleration/deceleration (See section 3.2.6 for more details). In table 4.2 we have listed the translational/rotational acceleration/velocities and their time durations as observed by Nusholtz *et al.* (1984) for three of the kinematic loading conditions. For each loading case we obtain the hydrostatic stress evolution throughout the brain geometry using FEM (see section 3.2.6). In each of the loading case, we identify three locations of interest where the peak stress is maximum, minimum and intermediary. They are denoted as Max, Min and Int respectively. For each of the 9 stress evolution cases, we use our current model to predict the extent of calpain activation and tau phosphorylation. Table 4.3 shows the peak calcium concentration, peak activated calpain concentration and the peak value of $\mathcal{N}$ ($\mathcal{N}_{peak}$) for each case at the three locations.

It can be observed from the values listed in table 4.3 that the peak levels of tau phosphorylation are higher if the peak Ca^{2+} concentration $\left(c_i^{peak}\right)$ reaches a higher value. However, the relationship between c_i^{peak} and $\mathcal{N}_{peak}$ is not linear. For c_i^{peak} comparable to homeostatic value $c_{i,\text{hom}}$, the peak tau phosphorylation levels $\mathcal{N}_{peak}$ does not deviate significantly from the homeostatic value $\mathcal{N}_h = 2.33$ as seen from the 'Min' location in each of the case. On the other hand at locations faraway from homeostatis e.g. 'Max' location in each case, the tau phopshorylation levels see major increase as compared to $\mathcal{N}_h$. Table 4.3 indicates that an intracellular Ca^{2+} accumulation even upto ~8 times the homeostatic Ca^{2+} levels, does not increase the tau phosphorylation level much over their homeostatic value ($\mathcal{N}_h = 2.3345$). However once the intracellular Ca^{2+} reaches ~ 10 times the homeostatic levels, the increase in tau phosphorylation levels are appreciable, and continue to rise faster as the Ca^{2+} accumulation increases. The variable sensitivity exhibited by $\mathcal{N}_h$ to the extent of deviation of Ca^{2+} concentration from homeostatic value provides an interesting insight into the toxicity of accumulated intracellular Ca^{2+} i.e. a limited increase in the Ca^{2+} concentration should not be threatening as it may not directly result in an increased tau phosphorylation. These observations clearly point to the fact that intracellular Ca^{2+} accumulation is not always the best indicator of the extent of secondary injury involving damage to the MT bundles in an axon, instead tau phosphorylation levels should also be monitored. However, it must be cautioned that other observed secondary injuries such as mitochondrial damage mediated cytotoxicity and cleavage of essential proteins are not solely dependent upon the tau phosphorylation levels and hence not within the purview of the current model. An investigation into the intermediate step responsible for the variable sensitivity discussed here is carried out in the Appendix D. A second observation that we can make from the tau phosphorylation levels listed in table 4.3 is that for the loading cases dealt in here, the highest value of $\mathcal{N}_{peak}$ is less than observed in vivo phosphorylation levels post fatal tauopathies (Iqbal *et al.*, 2009; Ksiezak-Reding *et al.*, 1992). Thus, a single mild TBI may not be sufficient to cause a pathologically significant increase in tau phosphorylation. This is consistent with the clinical findings that risks of long lasting neurological dysfunctions are significantly higher only for repetitive mild TBIs occuring over the years resulting in CTE and similar neurodegenerative tauopathies (McKee *et al.*, 2009; Blennow *et al.*, 2016).

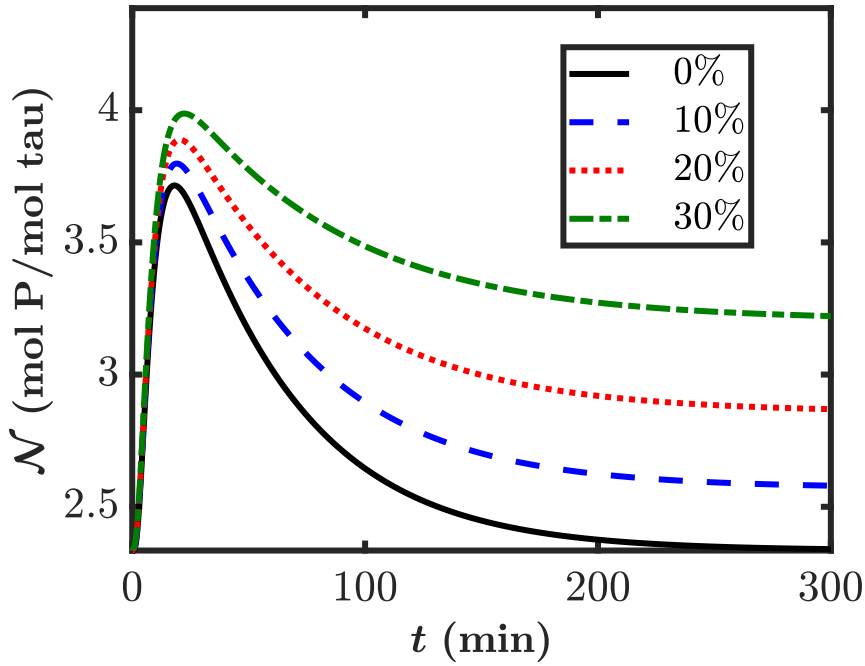

Figure 4.3: The effect of reducing the activity of PP2A on the evolution of tau phosphorylation levels. The loading case used here is CASE 1Int from table 4.3. The reduction in the activity of PP2A phosphatase is simulated in our model via decrease in V_{de} value by 10, 20 and 30% as compared to its calibrated value noted in table 4.1.

4.5.3 Effects of PP2A Dephosphorylation

From Fig. 4.2b we observe that although the tau phosphorylation levels exceed $\mathcal{N}_h$ after the incidence of mechanical loading, eventually after a finite time it returns to the homeostatic state. The recovery to homeostatis occurs due to dephosphorylation activity of phosphatase PP2A (equation (4.7)). In reality, a reduced PP2A activity due to increased presence of inhibitors has been reported in post AD human brain (Iqbal *et al.*, 2009) and brains of patients afflicted with severe TBI (Yang *et al.*, 2017). However owing to lack of precise knowledge of mechanisms leading to the reduction of PP2A activities after a TBI prevents us from including its effects in our mathematical model. However the consequence of reduced PP2A activity can be phenomenologically simulated by artificially reducing the kinetic parameter V_{max} and consequently $V_{de} = V_{\max}/[tau]_0$ in our model (equations (4.6-4.7)) which signifies the maximal activity of the phosphatases towards phosphorylated tau. As a representative example, for this simulation we chose the load-

ing case 1 listed in table 4.2, and further select the point where the peak stresses are in an intermediate range (CASE 1Int in table 4.3). We repeat our previous simulation with a reduction of the parameter V_{de} by 10%, 20% and 30% with respect to its values listed in table 4.1. Figure 4.3 shows the effect of reduction of V_{de} on the temporal variation of tau phosphorylation as compared to the baseline result shown through solid line (0% curve). Although the qualitative nature of the curve remains the same but the reduced PP2A activity simulated via reduced value of the parameter V_{de} prevents the tau phosphorylation level ($\mathcal{N}$) to restore to its homeostatic value ($\mathcal{N}_h$) even after a sufficiently long time. Figure 4.3 also shows that more the V_{de} deviation from its calibrated value (Table 4.1), the more is the residual tau phosphorylation level and so also the peak $\mathcal{N}$ value. The residual phosphorylation level of tau may be treated as an indicator of the irreversible phosphorylation of some tau protiens. Any future TBIs will only lead to higher tau hyperphosphorylation levels, as is seen in neurodegenerative taupathies like CTE (McKee *et al.*, 2009; Blennow *et al.*, 2016). Once the mechanisms governing the reduction in PP2A activities are identified, more rigorous mathematical model can replace the artificial reduction model being used here.

4.5.4 A Speculative Interpretation for Future Scope

Our model predicts the level of phosphorylation $\mathcal{N}$ defined as the average number of phosphorylated sites per tau protein upon the action of external mechanical load incurred during incidences like TBIs. Physiologically the effects of tau phosphorylation are seen in the form of reduced affinity of hyperphosphorylated tau towards the MT bundles, thereby disrupting the MT assembly, leading to formation of axonal varicosities (Smith and Meaney, 2000; Tang-Schomer *et al.*, 2012; Blennow *et al.*, 2016). The intensity of physiologically observed secondary injuries might be quantified in terms of the number of hyperphosphorylated tau proteins. As pointed earlier, the present work sidesteps the stochastic nature of the tau phosphorylation process and offers an average prediction. A means to rectify this limitation is through an assumed probability distribution of the phosphorylation level amongst all the tau proteins, such that the mean of the probability distribution corresponds to $\mathcal{N}$, the average occupancy per tau protein as predicted by our model at any time. Given a probability density function PDF ($\mathcal{N}_x$) over the randomly distributed phosphorylation levels $\mathcal{N}_x$, we can calculate the fraction of tau proteins hyperphosphorylated by introducing a threshold value of $\mathcal{N}$, such that tau proteins with phosphorylation levels above this

threshold value, say $\mathcal{N}_{th}$, are considered to be hyperphosphorylated. Amongst the many possible forms for the probability distribution function (PDF), the one that is selected should be in sync with the problem at hand. As a first approximation, we choose the widely applied PDF *log-normal distribution* which is skewed, usually used in situations involving low mean values, large variances, non-negative value of the random variable (Limpert *et al.*, 2001). The estimation of the variance of the PDF may be feasible using experimental measurement of the phosphorylation levels of in-vitro brain tissue specimens undergoing a simulated injury.

For a log-normal PDF,

$$\text{PDF}(\mathcal{N}_x) = \frac{1}{\mathcal{N}_x v\sqrt{2\pi}} e^{-\frac{(log(\mathcal{N}_x)-m)^2}{2\times v^2}} \tag{4.10}$$

the fraction of hyperphosphorylated tau proteins are given as,

$$\frac{[\text{P-tau}]}{[\text{tau}]_0} = \int_{\mathcal{N}_{th}}^{\infty} \left\{ \frac{1}{\mathcal{N}_x v\sqrt{2\pi}} e^{-\frac{(log(\mathcal{N}_x)-m)^2}{2\times v^2}} \right\} d\mathcal{N}_x \tag{4.11}$$

where, m and v are parameters of the probability distribution governing its median and skewness respectively. We consider a log normal PDF with mean at $\mathcal{N} = 3$ and assume for the sake of calculations $v = \log(1.5) = 0.4$, a value typically observed in a variety of medical and epidemiological observations (Limpert *et al.*, 2001). Further we decide that hyperphosphorylation of tau occurs over a threshold level $\mathcal{N}_{th} = 6$ mol P/ mol tau, based on the lower limit of phosphorylation levels observed in AD P-tau (Köpke *et al.*, 1993; Iqbal *et al.*, 2009). Through equation (4.11), we predict that when the phosphorylation levels reach peak value $\sim 7\%$ tau would be hyperphosphorylated. The reduction in MT assembly stability post tau removal due to hyperphosphorylation has been previously studied, though without a motivation for the number of tau proteins being removed (Sendek *et al.*, 2014). A mathematical framework, motivated by our speculative discussions in this section, permits the prediction of the number of hyperphosphorylated tau proteins, thus bridging an important gap. It goes without saying that experimentally supported parameter values and PDF would yield a better prediction of the fraction of hyperphosphorylated tau.

4.6 Conclusion

We have developed a kinetics based non-spatial model to predict the extent of secondary insult following a TBI. While the primary insult after the occurrence of a TBI, can result in a significant mechanical stress in the brain tissue, the physiological effects which characterize a TBI are typically an outcome of biochemical disturbances involved in the secondary insult phase. Initiated by an accumulation of excess intracellular Ca^{2+}, secondary insults in the axonal region of the neuron are associated with disruption of MT assembly due to dysfunction of tubulin binding tau proteins. Apart from the mechanical failure in the dimeric binding of tau proteins caused due to high stretch rates (Ahmadzadeh *et al.*, 2015), MT dissassembly can also occur due to the multiple posttranslational modifications of tau proteins. In the current work, we have focussed on one such posttranslational modification, the hyperphosphorylation of tau protein which apart from CTE resulting from repetitive occurrence of mild or severe TBI is also common to many other neurogenerative tauopathies like AD, frontotemporal dementia.

We believe our model provides a firm mathematical framework with a rich scope for further development. Either due to simplifying assumptions or due to lack of experimental data, the current model has a few limitations that could form the basis of any future work in this direction. Calpain mediated breakdown of other proteins such as spectrin could be incorporated in the model. The PM permeability is known to be altered due to spectrin breakdown. By carefully integrating an experimental evidence based functional dependence of membrane permeability on spectrin breakdown, the model can be enabled to capture a biphasic calcium accumulation leading to a sustained calpain mediated tau damage. Although we have incorporated the effect of reduction in the PP2A activity through parameter modification, an experimental investigation into the mechanism of PP2A inhibition after TBI is required to enhance the fidelity of the model. Finally, to predict the extent of tau phosphorylation, we calculate the average number of occupied sites per tau proteins, considering all tau proteins whether phosphorylated or not. Establishing a relationship between this term and the number of tau proteins actually being phosphorylated will allow a better prediction of tau hyperphosphorylation. Since the neurochemical changes captured in the current model for TBI are common to many other neurodegenerative diseases, we believe that similar kinetic models could prove useful in simulating such diseases.

Chapter 5

Summary and Future Plans

5.1 Summary

In this work we have focussed on the mechanisms of damage involved in a neurological tissue following a TBI, and their prediction via the development of a mathematical model which captures not just the mechanical insult but also some of its neurochemical consequences. We begin by proposing a non spatial phenomenological model which captures the intracellular Ca^{2+} accumulation in a neuron in presence of an external hydrostatic pressure impulse. To the best of our knowledge, this work is the first effort to incorporate the mechanical effects of TBI into the calcium kinetics in a neuron. We have shown that in the absence of external mechanical loads, the model is stable to any disturbance in the intracellular concentration from the homeostatic value and regains its homeostatic state in a short span of time. Furthermore when subjected to isolated and repeated impulse loads in a manner reported by in vitro test on cells like neurons and astrocytes, the model successfully captures the effect of magnitude and duration of the impulse on the intracellular Ca^{2+} concentration observed experimentally (LaPlaca *et al.*, 1997; Geddes and Cargill, 2001; Geddes-Klein *et al.*, 2006; Maneshi *et al.*, 2015). The predictions of the mathematical model are qualitatively consistent with the key features of the experimental observations, as follows:

- When subjected to an impulse loading, the typical profile of the intracellular concentration shows an initial rapid increase followed by a gradual fall to a non homeostatic residual value over a period of settling time t_s.

- For a severe injury, i.e. for a higher magnitude or duration of the impulse, t_s is higher.
- Increasing the severity of the external impulse through either its magnitude, duration or loading rate, increases both the peak c_i^{peak} as well as the residual c_i^{res} concentrations.
- Repeated impulse is more harmful than a single impulse load since both the peak as well as the residual concentration increases with the number of loading cycles.
- The smaller the time interval between the loading cycles, higher is the peak intracellular concentration. However, increasing the time interval, t_i beyond t_s, has no effect on the peak intracellular concentration.

Next we extend the non-spatial calcium kinetics model by introducing a spatial dimension. We do this by coupling the non spatial model to the FEM based mechanistic models and assuming that the calcium kinetics at any location is influenced only by the local hydrostatic stress in that region alone. The resulting spatial model combines the advantages of both the calcium kinetics model as well as the FEM based mechanistic models into a single mathematical framework which can now be used to predict both primary as well as the secondary injuries. The coupled spatialised calcium kinetics model presents the following advantages over the older non spatial model:

- Firstly, a TBI occurs due to either an external force or an inertial force due to sudden acceleration/deceleration. The new model provides a systematic pathway to determine the intracellular Ca^{2+} accumulation based on either of these external stimuli parameters rather than an internal parameter like local hydrostatic stress.
- The spatial model reveals the intracellular Ca^{2+} concentration distribution throughout the brain, rather than one localised hypothetical point.
- Finally, the new model provides a means to incorporate the constitutive properties of the brain in our analysis, thus taking into consideration the transient peaks in the local stress due to transient pressure waves in the brain.

The results of the coupled spatialised calcium kinetics model allow us to arrive at the following conclusions:

- Although the calcium evolution obtained is qualitatively similar to the results for the non spatial case, incorporating the dynamic effects of the constitutive properties result in a much higher calcium accumulation.
- As the geometry being analyzed becomes shorter, the results of the spatial calcium kinetics model tends to the non-spatial model solutions. We observe for the 2D case that as the dimensions of the geometry become smaller than 4 mm, the spatial variations in the local pressure as well as the intracellular Ca^{2+} concentration, become insignificant.
- We therefore suggest that when performing experiments, in order to avoid discrepancies between the applied load and local stress state due to transient stress waves, the specimen length should be smaller than 4 mm.
- Parameters obtained from purely mechanistic FEM based models may not precisely predict the locations of secondary injuries as they are unable to take into the account the durations for which peak values of these parameters last.
- At an insignificant computational cost our model blends both the peak values as the durations of these parameters to predict the intracellular calcium accumulation, which is therefore a more definitive as well as direct indicator of secondary injuries.
- Application of the model to a realistic 2D brain geometry gives a further evidence as to difference in location of peak pressures and expected critical locations of secondary injury. Given a threshold for tolerable intracellular Ca^{2+} concentration, our model can predict the exact regions where secondary injuries occur.

We believe that our coupled model can be a very useful tool for medical practitioners. Primary injuries occur usually immediately but secondary injuries are highly delayed, thereby theoretically permitting a time interval for positive therapeutic interventions which can potentially save lives. Our model presents the potential to act as an assistive tool for decision making during this period.

Following the development of the mathematical model at a cell level and its further extension to tissue level, we now focus our attention on trying to capture the intricacies of the secondary injuries at an intraneuronal level. Secondary injuries can involve a plethora of physiologies of which diffused axonal injuries, involving a slow degradation of the neurons via tau pathologies, are most common. Single such injuries might be tolerable

and recoverable, but multiple repetitions can result in lasting neurodegenerative disorders. We create a mathematical model to estimate the extent of calpain enzyme activation due to the intracellular Ca^{2+} accumulation. We assume calpain activation to be a single step reaction involving a cooperative binding of Ca^{2+} at 6 active sites. N-terminal truncation of GSK-3β kinase by activated calpain is then simulated in accordance with the experiments in the literature. Finally, we model the activity of kinase and its truncation products on tau protein, allowing us to determine the number of tau sites being phosphorylated. Additionally, we provided a probability distribution based methodology to translate our results into a quantitative value of hyperphosphorylated tau. The predictions of our model match well with the key features of experimental and clinical observations:

- In the absence of any external load, a state of homeostasis is maintained, such that no calpain is activated, no kinase is truncated, and tau phosphorylation levels stay at their homeostatic value, N_h = 2.33 mol P/mol total tau.
- The predicted in vivo activated calpain concentrations fall within the range of activated calpain used in vitro.
- The increase in GSK-3β activity towards tau due to calpain mediated truncation is seen to be qualitatively similar to the experimental reports.
- Our model predicts that a Ca^{2+} accumulation up to ~8 times the homeostatic value should not directly result in increased tau phosphorylation. However, as more and more Ca^{2+} is accumulated levels of tau phosphorylation become increasingly sensitive to it.
- Reduced PP2A phosphatase activity after TBI will result in unrecoverable tau phosphorylation levels, which makes successive TBI progressively more dangerous, as is clinically observed.
- A single mild TBI may not result in enough phosphorylation to observe any physiological symtomps. However, repeated incidences will result in an appreciable level of unrecoverable tau phosphorylation.

We have thus developed a comprehensive mathematical model to simulate the intraneuronal calcium accumulation, its distribution throughout the brain geometry and the

resulting neuronal degradation due to the involved tau pathologies. The numerical model has provided numerous insights into the multiple mechanisms of post TBI damage in the neurons. TBIs have been called a silent epidemic because the mental changes in behavorial and perceptual impairments, especially in case of mild forms of TBI, are very gradual and not readily apparent. With our model we hope to provide a definitive mathematical tool to predict such gradual non mechanistic damages in response to a mild TBI.

5.2 Future Scope

We propose that there is scope for development in this model towards making it more realistic. In our model we have assumed that the calcium kinetics parameters in the all the regions of the cerebrum are spatially homogeneous. This may not be the case in reality, and experiments can be performed on small samples (< 4 mm) of different anatomical parts of the brain, so as to calibrate the non-spatial calcium kinetics model parameters for each part of the brain. The calibration procedure, as described in section 2.4.2, can be used to obtain the value of the kinetic parameters specific to those parts of the brain. Finally, the spatial calcium kinetics model can be made much more accurate by coupling it with a more detailed 3D FEM analysis, like the ones performed by Zhang *et al.* (2001); Levchakov *et al.* (2006); Mao *et al.* (2006); Takhounts *et al.* (2008), and other similar studies. The linear viscoelastic constitutive law for brain tissue adopted in the current work can also be improved by incorporating geometric non-linearities for accurate estimates of stress and strain. Such a comprehensive mathematical tool for predicting both primary and secondary injuries after the occurrence of a TBI will be very useful in the hands of doctors, especially considering the fact that the effects of TBI manifest long after the actual occurrence of the injury.

On an intracellular level we are able to now mathematically model the intraneuronal calcium accumulation due to external mechanical impacts on the brain tissue. We are modelling the calcium ion induced microtubule degradation as the medium of predicting damage in the neuron. Other neurochemical pathways involving damage of intracellular organelles and plasma membrane proteins also play an important role in conjunction with the microtubule dysfunction and can be simulated based on appropriate experimental evidences.

Appendices

Appendix A

System Under Homeostasis

A.1 Linear Stability

In an undisturbed state (i.e. at homeostasis),

$$c_e = c_e^*; \quad c_i = c_i^*, \tag{A.1}$$

$$\left.\frac{dc_e}{dt}\right|_{(c_e^*, c_i^*)} = \left.\frac{dc_i}{dt}\right|_{(c_e^*, c_i^*)} = 0. \tag{A.2}$$

Substituting equations Eqs. (A.1-A.2) in Eq. (2.1), we obtain the following identity between the kinetic parameters,

$$\begin{aligned} K_{pm}\left(c_e^* - c_i^*\right) &= V_{pm0}\left\{\frac{{c_i^*}^{n_{pm}}}{{c_i^*}^{n_{pm}} + k_{pm}^{n_{pm}}}\right\}, \\ K_{er}\left(c_e^* - c_i^*\right) &= V_{er0}\left\{\frac{{c_i^*}^{n_{er}}}{{c_i^*}^{n_{er}} + k_{er}^{n_{er}}}\right\}. \end{aligned} \tag{A.3}$$

In order to linearize the governing equations Eqs. (2.1-2.3), it is assumed that the extracellular (c_e) and intracellular (c_i) concentrations are slightly perturbed from their homeostatic values, such that,

$$\begin{aligned} c_e &= c_e^* + \epsilon_e, \quad \text{and} \\ c_i &= c_i^* + \epsilon_i, \end{aligned} \tag{A.4}$$

where, ϵ_e and ϵ_i are the infinitesimal perturbations in the extracellular and the intracellular concentrations respectively.

Substituting Eq. (A.4), into equations Eqs. (2.1-2.3), applying Taylor series expansion to all the expressions involving the perturbed concentrations and retaining up to linear terms, and utilizing Eq. (A.3), the linearized equations are as follows,

$$\begin{aligned} \frac{d\epsilon_e}{dt} &= -\mathbb{A}\epsilon_e + \mathbb{B}\epsilon_i, \\ \frac{d\epsilon_i}{dt} &= \mathbb{A}\epsilon_e - (\mathbb{B} + \mathbb{C})\epsilon_i, \end{aligned} \tag{A.5}$$

where, $\mathbb{A}$, $\mathbb{B}$ and $\mathbb{C}$ are constants such that,

$$\begin{aligned} \mathbb{A} &= K_{pm}, \\ \mathbb{B} &= K_{pm} + V_{pm}\left\{\frac{k_{pm}^{n_{pm}} n_{pm} c_i^{*^{n_{pm}-1}}}{\left(c_i^{*^{n_{pm}}} + k_{pm}^{n_{pm}}\right)^2}\right\}, \quad \text{and} \\ \mathbb{C} &= K_{er} + V_{er}\left\{\frac{k_{er}^{n_{er}} n_{er} c_i^{*^{n_{er}-1}}}{\left(c_i^{*^{n_{er}}} + k_{er}^{n_{er}}\right)^2}\right\}. \end{aligned} \tag{A.6}$$

We obtain the eigenvalues of the linearized governing equation, Eq. (A.5), to be,

$$\begin{aligned} \lambda_1 &= \frac{1}{2}\left(-\mathbb{A} - \mathbb{B} - \mathbb{C} - \sqrt{-4\mathbb{A}\mathbb{C} + (\mathbb{A} + \mathbb{B} + \mathbb{C})^2}\right), \quad \text{and} \\ \lambda_2 &= \frac{1}{2}\left(-\mathbb{A} - \mathbb{B} - \mathbb{C} + \sqrt{-4\mathbb{A}\mathbb{C} + (\mathbb{A} + \mathbb{B} + \mathbb{C})^2}\right). \end{aligned} \tag{A.7}$$

Simplifying in terms of the constants,

$$\lambda_{1,2} = \frac{1}{2}\left(-\beta \mp \sqrt{\beta^2 - \gamma}\right) \tag{A.8}$$

where, $\beta = \mathbb{A} + \mathbb{B} + \mathbb{C}$, and $\gamma = -4\mathbb{A}\mathbb{C}$. Substituting the parameter values given in Table 2.1, we get the eigenvalues as $\lambda_1 = -0.0734$, and $\lambda_2 = -1.057 \times 10^{-6}$. Since both the eigenvalues of the linearized governing equation are negative, we are assured that the system of equations is stable under small perturbations at homeostasis.

A.2 Initial Value Problem

We solve the linearized governing equation (A.5) using the initial conditions,

$$\left.\frac{c_e}{c_i^*}\right|_{t=0} = 1 \times 10^4, \quad \text{and}$$
$$\left.\frac{c_i}{c_i^*}\right|_{t=0} = \mathcal{I} \tag{A.9}$$

We obtain the evolution of the intracellular concentration normalized with respect to the homeostatic intracellular concentration, c_i^*, as,

$$\begin{aligned}\frac{c_i(t)}{c_i^*} = 1 + \frac{(\mathcal{I}-1)}{\sqrt{-4\mathbb{A}\mathbb{C} + (\mathbb{A}+\mathbb{B}+\mathbb{C})^2}} \\ \left\{\left(-\mathbb{A}+\mathbb{B}+\mathbb{C}+\sqrt{-4\mathbb{A}\mathbb{C}+(\mathbb{A}+\mathbb{B}+\mathbb{C})^2}\right)e^{\lambda_1 t}\right. \\ \left.\left(+\mathbb{A}-\mathbb{B}-\mathbb{C}+\sqrt{-4\mathbb{A}\mathbb{C}+(\mathbb{A}+\mathbb{B}+\mathbb{C})^2}\right)e^{\lambda_2 t}\right\}.\end{aligned} \tag{A.10}$$

The solution presented in equation (A.9) offers two intrinsic time scales for the system,

$$\begin{aligned}\hat{\tau}_1 &= -\frac{1}{\lambda_1} = 2\left(\beta + \sqrt{\beta^2-\gamma}\right)^{-1} = 13.62\ s, \quad \text{and} \\ \hat{\tau}_2 &= -\frac{1}{\lambda_2} = 2\left(\beta - \sqrt{\beta^2-\gamma}\right)^{-1} = 9.5\times 10^5\ s.\end{aligned} \tag{A.11}$$

Of these two time scales, $\hat{\tau}_1$ is more reasonable as it lies within the time frame when the neurochemical changes due to secondary injuries in a TBI begin to set in. Substituting the values of $\mathbb{A}$, $\mathbb{B}$, $\mathbb{C}$, λ_1 and λ_2, using equations (A.6,A.8), we obtain the following expressions for the normalized extracellular and intracellular concentrations,

$$\begin{aligned}\frac{c_e(t)}{c_i^*} &= 1000 + 0.6406(I-1)\left\{e^{-1.0566\times10^{-6}t} - e^{-0.07343t}\right\}, \quad \text{and} \\ \frac{c_i(t)}{c_i^*} &= 1 + (I-1)\left\{0.999974e^{-0.07343t} + 0.000026e^{-1.0566\times10^{-6}t}\right\}.\end{aligned} \tag{A.12}$$

Appendix B

System Under Presence of External Loads

Similar to previous section, the process of linearization is carried out when the kinetic parameters are not constants, but rather a function of the stress measure, $\hat{s}$, through equation (2.5). In order to simulate a small deviation from homeostasis ($\sigma_h = 0$, $\hat{s} = 0$, $c_e = c_e^*$, and $c_i = c_i^*$), in addition to the perturbation to the intracellular and extracellular concentrations as done through equation (A.4), the hydrostatic stress and the stress measure are assumed as,

$$\begin{aligned} \sigma_h &= \delta\sigma_h, \quad \text{and} \\ \hat{s} &= \delta\hat{s}. \end{aligned} \tag{B.1}$$

According to equation (2.6),$\hat{s}$and σ_h are already linear with respect to each other and therefore,

$$\delta\hat{s} = \delta\sigma_h + \alpha \int_0^t \delta\sigma_h(t)dt. \tag{B.2}$$

Using the Taylor series, the terms involving ϵ_e, ϵ_i and δs, in equations (2.1-2.3,2.5) are expanded up to linear terms and in conjunction with equation (A.3) leads to,

$$\begin{aligned} \frac{d\epsilon_e}{dt} &= -\mathbb{A}\epsilon_e + \mathbb{B}\epsilon_i - \mathbb{T}_1\delta\hat{s}, \\ \frac{d\epsilon_i}{dt} &= \mathbb{A}\epsilon_e - (\mathbb{B} + \mathbb{C})\epsilon_i + (\mathbb{T}_1 + \mathbb{T}_2)\delta\hat{s}, \end{aligned} \tag{B.3}$$

where, $\mathbb{A}$, $\mathbb{B}$ and $\mathbb{C}$ are defined in equation (A.6), and $\mathbb{T}_1$ and $\mathbb{T}_2$ are given as,

$$\begin{aligned}\mathbb{T}_1 &= V_{pm0}\left\{\frac{c_i^{*^{n_{pm}}}}{c_i^{*^{n_{pm}}} + k_{er}^{n_{pm}}}\right\}\kappa\left(1+\chi_{pm}\right) = 2.6471\times 10^{-7}, \quad \text{and} \\ \mathbb{T}_2 &= V_{er0}\left\{\frac{c_i^{*^{n_{er}}}}{c_i^{*^{n_{er}}} + k_{er}^{n_{er}}}\right\}\kappa\left(1+\chi_{er}\right) = 5.6957\times 10^{-7}.\end{aligned} \tag{B.4}$$

Looking at the linearized governing equation (B.3), we can see that the eigenvalues have remained unchanged comparing to the homeostatic system of equations. This also implies that the intrinsic time scale of the system of equations stays the same.

The solution of the equation (B.3), subjected to homeostatic initial conditions, $c_e = c_e^*$, and $c_i = c_i^*$; and a constant hydrostatic loading condition of $\sigma_h = \delta\sigma_h$, is analytically quite cumbersome. Hence, the solution is evaluated using Wolfram Mathematica 11.0.

For solving the linearized equation (B.3) for an impulse loading scenario, we assume an impulse to be a superimposition of two constant loads, while additionally accounting for the stress history. The solutions obtained through this notebook for different impulse loads are directly used in the main article. Analytical solution for a series of impulses can be obtained by further extending the idea of superimposition of constant loads.

Appendix C

Analytical Solution for 1D Uniaxial Constant Load

Consider a viscoelastic bar of length L as shown in Fig. C.1, one end of which is fixed, while at the other end a constant stress of magnitude $\sigma^*(t) = \sigma^*$ is applied. The Standard Linear Solid viscoelastic relaxation law in terms of the elastic modulus for a uniaxial case can be written as,

$$\mathbf{E}(t) = \mathbf{E}_\infty + \mathbf{E}_1 e^{-\mathbf{E}_1 t/\eta}, \tag{C.1}$$

where the material constants $\mathbf{E}_\infty$, $\mathbf{E}_1$, and η are defined as,

$$\begin{gathered} \mathbf{E}_\infty = \frac{9\mathbf{G}_\infty\mathbf{K}}{3\mathbf{K}+\mathbf{G}_\infty}, \quad \mathbf{E}_1 = \frac{27\mathbf{G}_1\mathbf{K}^2}{(3\mathbf{K}+\mathbf{G}_\infty)(3\mathbf{K}+\mathbf{G}_\infty+\mathbf{G}_1)}, \quad \text{and} \\ \eta = \frac{9\mathbf{K}-\mathbf{E}_\infty}{9\mathbf{K}-\mathbf{E}_\infty-\mathbf{E}_1} \times \mathbf{E}_1\tau \end{gathered} \tag{C.2}$$

Figure C.1: Tissue modelled as 1D viscoelastic bar of length L and thickness $L/100$, constrained at end $x = 0$, and subjected to a load $\sigma^*(t)$ at the other end. The viscoelastic behaviour of the bar is represented through Eqs.(3.3-3.4) and Table 3.1.

where, $\mathbf{G}_\infty$ and $\mathbf{G}_1$ are the shear modulus corresponding to the long time and relaxation time, τ. $\mathbf{K}$ denotes the bulk modulus. For the ease of calculations, we normalize the variables as follows,

$$\begin{aligned} \mathcal{T} &= \frac{\mathbf{E}_0 t}{\eta}, \qquad \xi = \frac{\sqrt{\rho \mathbf{E}_0}}{\eta} x = M\frac{x}{L}, \qquad \Sigma = \frac{\sigma}{\sigma^*}, \\ \mathcal{U} &= \frac{\sqrt{\rho \mathbf{E}_0}}{\eta} u = M\frac{u}{L}, \quad \text{and} \qquad \epsilon = \frac{\mathbf{E}_0 \varepsilon}{\sigma^*} = \frac{\mathbf{E}_0}{\sigma^*}\frac{\partial \mathcal{U}}{\partial \xi} \end{aligned} \tag{C.3}$$

where $\mathcal{T}$, ξ, Σ, $\mathcal{U}$, ϵ are the non-dimensionalized time t, space co-ordinate x, stress σ, displacement u and strain ϵ respectively and $\mathbf{E}_0 = \mathbf{E}_\infty + \mathbf{E}_1$. The factors $\eta/\mathbf{E}_0$ and $\eta/\sqrt{\rho \mathbf{E}_0}$ used to normalize time and length respectively, represent the characteristic time and length offered by the material model. The space co-ordinate and displacement scaled by the length of the bar are related to their dimensionless counterparts ξ and $\mathcal{U}$ through non-dimensional parameter $M = L\sqrt{\rho \mathbf{E}_0}/\eta$. M compares the length of the bar to the material characteristic length.

Using Eq. (3.1-3.4, and C.3), the normalized equation of motion in the x-direction, the constitutive law, the relaxation law and the boundary conditions can be expressed as follows,

Equation of Motion: $$\frac{\partial \Sigma}{\partial \xi} = \frac{\mathbf{E}_0}{\sigma^*} \times \frac{\partial^2 \mathcal{U}}{\partial \mathcal{T}^2}, \tag{C.4}$$

Constitutive Law: $$\Sigma(\mathcal{T}) = \int_0^{\eta \mathcal{T}/\mathbf{E}_0} \mathbf{E}(\mathcal{T} - \tilde{\mathcal{T}})\dot{\epsilon}(\tilde{\mathcal{T}})d\mathcal{T}, \tag{C.5}$$

Relaxation Law: $$\mathbf{E}(\mathcal{T}) = 1 - \psi + \psi e^{-\psi \mathcal{T}}, \tag{C.6}$$

Boundary Conditions: $$\mathcal{U}(0, \mathcal{T}) = 0, \text{ and } \quad \Sigma(M, \mathcal{T}) = 1 \tag{C.7}$$

where, $\psi = \mathbf{E}_1/\mathbf{E}_0$. The wave equation given by Eq. (C.4) in conjunction with Eqs.(C.5 - C.7) can be solved analytically using Laplace transforms. In the transformed domain, the Eqs.(C.4 - C.7) can be rewritten as,

$$\frac{\partial^2 \bar{\mathcal{U}}}{\partial \xi^2} = \frac{s}{\bar{\mathbf{E}}(s)} \bar{\mathcal{U}}, \tag{C.8}$$

$$\bar{\Sigma} = s\bar{\mathbf{E}}(s)\bar{\epsilon}, \tag{C.9}$$

$$\bar{\mathbf{E}}(s) = \frac{s + \psi - \psi^2}{s(s + \psi)}, \tag{C.10}$$

$$\bar{\mathcal{U}}(0, s) = 0, \quad \text{and} \quad \bar{\Sigma}(M, s) = 1/s. \tag{C.11}$$

Following the procedure given by Christensen (1982), the general solution of Eqs.(C.8-C.11) can expressed as,

$$\bar{\mathcal{U}}(\xi, s) = \sum_{n=1}^{\infty} \bar{C}_n(s)\mathcal{U}^n(\xi) + \bar{\mathcal{V}}(\xi, s), \tag{C.12}$$

where, $\mathcal{U}^n(\xi) = sin[(2n-1)\pi\xi/2M]$ is the nth eigenvalue in the solution for an equivalent elastic bar, and $\bar{\mathcal{V}}(\xi, s) = (\sigma^*\xi)/(s^2\bar{\mathbf{E}}(s)\mathbf{E}_0)$ is the quasi-static solution for the viscoelastic bar. The coefficients $\bar{C}_n(s)$ are obtained by substituting the expression of $\bar{\mathcal{U}}(\xi, s)$ given in Eq.(C.12) into the governing equation in Eq.(C.8), and invoking the orthogonality of the elastic eigenvalues $\mathcal{U}^n(\xi)$. Combining the displacement solution with the constitutive law in Eq.(C.9) and the relaxation law in Eq.(C.10), we obtain the stress distribution over the length of the bar in Laplace domain as,

$$\bar{\Sigma}(\xi, s) = \frac{1}{s} + \frac{4}{\pi}\sum_{n=1}^{\infty}\left[\frac{(-1)^n}{(2n-1)} \times \frac{s(s+\psi)}{s^3 + \psi s^2 + \frac{(2n-1)^2\pi^2}{4M^2}s + \frac{(2n-1)^2\pi^2}{4M^2}\psi(1-\psi)} \times cos\left\{\frac{(2n-1)\pi\xi}{2M}\right\}\right] \tag{C.13}$$

Although an analytical inversion cannot be derived in a generalised fashion, by electing a specific value for M, substituting for ψ according to the material properties, and choosing to truncate the convergent infinite series after a finite number of terms enables us to invert the expression in the RHS of Eq.(C.13). We perform this operation in MAPLE for the values of M discussed in section 3.2.1, thus obtaining the stress evolution with time, plotted in Fig. 3.2 a, b and c.

Appendix D

Parametric Analysis

In this section, we study the sensitivity of the tau phosphorylation levels on each of the parameters we have estimated in section 4.4. For all the parameters except $K_{1/2}$ we note that the model is not very sensitive to modest changes in the system parameters. At even a 30% change in the parameter values, we may observe at most a 13% change in system output. Since we have fit the parameters to experimental observations, it is possible that a different set of experiments may reveal slightly different results depending on the procedures followed, or the tissue samples used. A low sensitivity of the output towards the fitted parameters is advantageous as it allows for conditional variations in the experiment.

Figure D.1 also shows the variation in the phosphorylation levels when the parameter $K_{1/2}$ is varied by ±30%. We see that the system output is very highly sensitive towards this parameter. Physically $K_{1/2}$ is the intracellular Ca^{2+} concentration required for half maximal calpain activation. As discussed in section 4.4, the exact value of this parameter is not well established in literature. The best estimates predict the value to be in the range of 0.6 - 2 μM (Cong *et al.*, 1989; Andrea *et al.*, 1996), which allows for a variation of $\sim 50\%$. Our sensitivity analysis suggests that the parameter needs to be further fine tuned by experimental investigations. However, this is easier said than done because of the complicated transport and reaction mechanisms which govern the reduced half maximal Ca^{2+} concentration in vivo.

In section 4.5.2 we discussed the predictions of the coupled chemical-mechanical model under application of varied kinematic loadings. Three cases of realistic kinematic loads as reported by Nusholtz *et al.* (1984) were simulated and the corresponding secondary insults at three different points were observed as listed in table 4.3. As per the

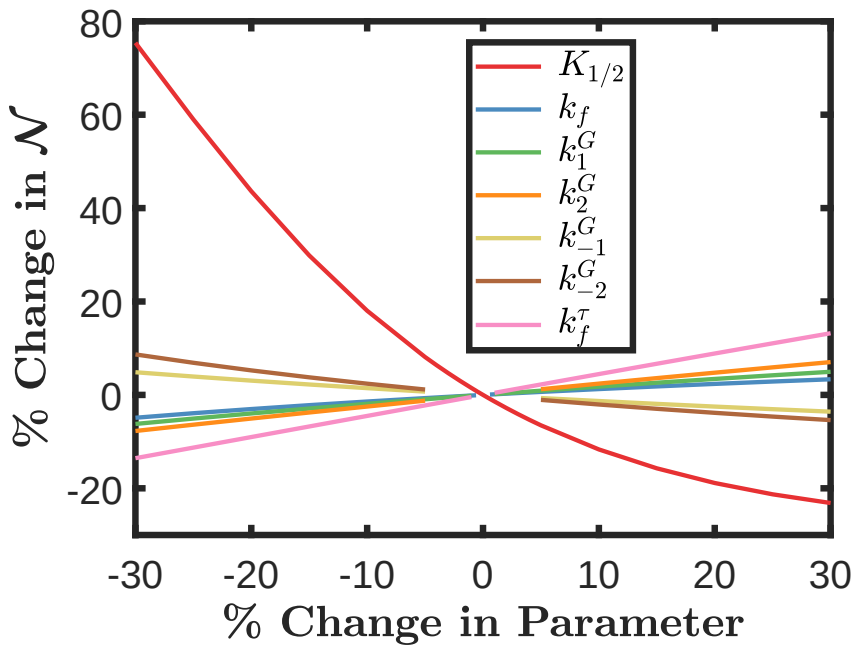

Figure D.1: Variation in the tau phosphorylation levels $\mathcal{N}$ as each of the parameter is varied by ±30%.

discussion in section 4.5.2, we saw that a limited increase in the intracellular Ca^{2+} concentration does not directly result in increased tau phosphorylation. It is only once the intracellular Ca^{2+} concentration becomes up to 10 times its homeostatic value that an appreciable increase in tau phosphorylation is seen. In order to explain the increase in tau phosphorylation sensitivity with increasing Ca^{2+} accumulation, we plot evolution of calcium accumulation, calpain activation, GSK-3β fragmentation and tau phosphorylation for each of the loading cases in figure D.2. This allows us to identify the single intermediate step which is responsible for the increased senstivity. We observe that the plots in figures D.2b - D.2d are quite similar qualitatively. The scaling of the x-axis in these figures gives us an idea of the different time scales involved at each of these steps. The qualitative similarity between these plots indicates that these steps are not the ones responsible for the increasing sensitivity of the tau phosphorylation with increasing Ca^{2+} accumulation.

On the other hand if we compare the plots in figures D.2a and D.2b we immediately see that as the peak Ca^{2+} concentration increase, the increase in peak calpain activation is increasingly more pronounced. For the cases 3Int and 2Int, while calcium accumulation

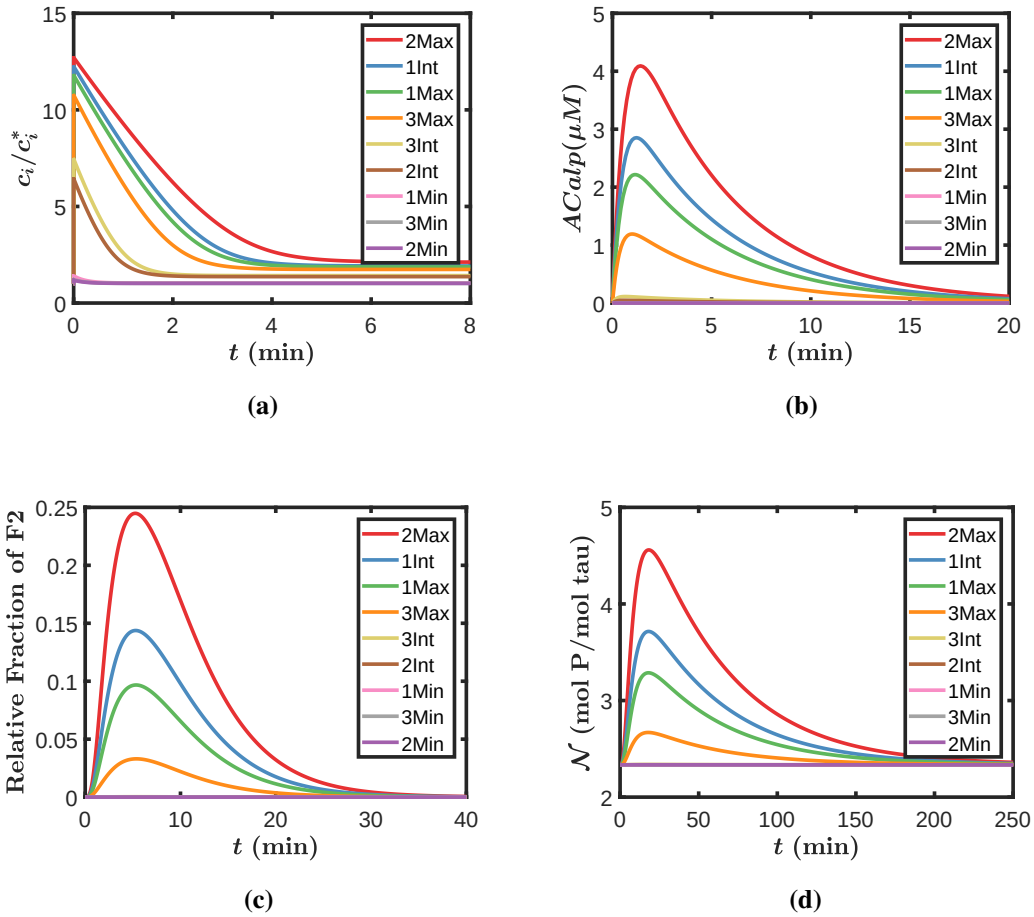

Figure D.2: For each of the kinematic loading cases at the three selected points of interests as listed in table 4.3, we plot the evolution of (a) Normalised intracellular Ca^{2+} concentration, (b) concentration of activated calpain, (c) relative fraction of the GSK fragment F2, and (d) average tau phosphorylation levels.

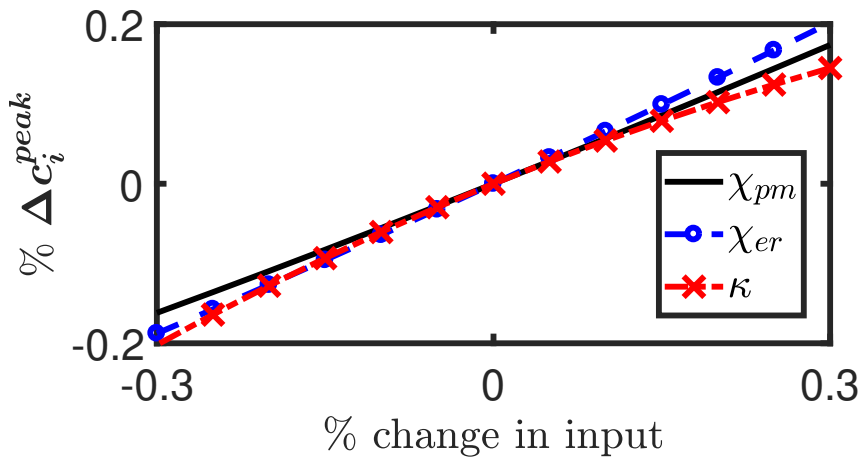

Figure D.3: Variation in the peak Ca^{2+} levels c_i^{peak} as each of the parameter is varied by ±30%.

is notable, the calpain activation is extremely low. On the other hand the calcium accumulation for the case of 2Max is just more than 1Int, but the calpain activation in the former case is much higher. This comparison indicates the increasing senstivity is an artefact of the calpain activation step, which is then inherited by the following steps. Such increase in sensitivity of calpain activation with increasing calcium accumulation can be attributed to the high degree of cooperativity of Ca^{2+} towards the binding sites on calpain. As discussed in section 4.4, the Hill coefficient for Ca^{2+} binding to calpain has been observed to be ~ 5. Mathematically, the Hill's coefficient contributes as an exponent in the equation governing the calpain activation. Therefore, at higher values of Ca^{2+} concentration even a small change can result in noticeable increase in calpain activation.

A parametric analysis for the stress dependent calcium kinetic is also performed to study the sensitivity of c_i^{peak} on the parameters χ_{PM}, χ_{ER} and κ, via equation 2.5. Figure D.3 shows the results of the sensitivity analysis. Ca^{2+} accumulation is observed to be moderately sensitive to changes in the parameters χ_{PM}, χ_{ER} and κ. It is therefore of essence that these parameters be calibrated carefully with specially designed experiments.

Bibliography

Adlard, Paul A, Carolyn E King, and James C Vickers, 2000, "The effects of taxol on the central nervous system response to physical injury," *Acta neuropathologica* **100**, 183–188

Agrawal, Amit, Sagar Galwankar, Vikas Kapil, Victor Coronado, Sridhar V Basavaraju, Lisa C McGuire, Rajnish Joshi, Syed Z Quazi, Sankalp Dwivedi, *et al.*, 2012, "Epidemiology and clinical characteristics of traumatic brain injuries in a rural setting in maharashtra, india. 2007-2009," *International journal of critical illness and injury science* **2**, 167

Ahmadzadeh, Hossein, Douglas H Smith, and Vivek B Shenoy, 2014, "Viscoelasticity of tau proteins leads to strain rate-dependent breaking of microtubules during axonal stretch injury: predictions from a mathematical model," *Biophysical journal* **106**, 1123–1133

Ahmadzadeh, Hossein, Douglas H Smith, and Vivek B Shenoy, 2015, "Mechanical effects of dynamic binding between tau proteins on microtubules during axonal injury," *Biophysical journal* **109**, 2328–2337

Alonso, Alejandra del C, Inge Grundke-Iqbal, and Khalid Iqbal, 1996, "Alzheimer's disease hyperphosphorylated tau sequesters normal tau into tangles of filaments and disassembles microtubules," *Nature medicine* **2**, 783–787

Anderson, Robert William Gerard, 2000, *A study on the biomechanics of axonal injury*, Ph.D. thesis (University of Adelaide)

Andrea, Baki, Peter Tompa, Anita Alexa, Orsolya Molnar, and Peter Friedrich, 1996, "Autolysis parallels activation of μ-calpain," *Biochemical Journal* **318**, 897–901

Baker, Helen L, Rachel J Errington, Sally C Davies, and Anthony K Campbell, 2002, "A mathematical model predicts that calreticulin interacts with the endoplasmic reticulum Ca^{2+}-ATPase," *Biophysical Journal* **82**, 582–590

Ballatore, Carlo, Amos B Smith, Virginia M-Y Lee, John Q Trojanowski, and Kurt R Brunden, 2016, "Microtubule-stabilizing agents for alzheimer's and other tauopathies," in *Alzheimer's Disease II* (Springer) pp. 159–179

Bandak, FA, AX Zhang, RE Tannous, F DiMasi, P Masiello, and Rolf H Eppinger, 2001, "Simon: a simulated injury monitor; application to head injury assessment," in *Proceedings: International Technical Conference on the Enhanced Safety of Vehicles* (National Highway Traffic Safety Administration) pp. 7–14

Baudry, Michel, and Xiaoning Bi, 2016, "Calpain-1 and calpain-2: the yin and yang of synaptic plasticity and neurodegeneration," *Trends in neurosciences* **39**, 235–245

Berridge, Michael J, Martin D Bootman, and H Llewelyn Roderick, 2003, "Calcium signalling: dynamics, homeostasis and remodelling," *Nature Reviews Molecular Cell Biology* **4**, 517–529

Blanke, M L, and A M J VanDongen, 2009, "Activation mechanisms of the nmda receptor," in *Biology of the NMDA Receptor*, edited by A M J VanDongen, Chap. 13 (Taylor & Francis, Boca Raton (FL))

Blennow, Kaj, David L Brody, Patrick M Kochanek, Harvey Levin, Ann McKee, Gerard M Ribbers, Kristine Yaffe, and Henrik Zetterberg, 2016, "Traumatic brain injuries," *Nature Reviews Disease Primers* **2**, 16084

Brini, Marisa, Tito Calì, Denis Ottolini, and Ernesto Carafoli, 2014, "Neuronal calcium signaling: function and dysfunction," *Cellular and Molecular Life Sciences* **71**, 2787–2814

Browne, Kevin D, Xiao-Han Chen, David F Meaney, and Douglas H Smith, 2011, "Mild traumatic brain injury and diffuse axonal injury in swine," *Journal of neurotrauma* **28**, 1747–1755

Büki, András, Robert Siman, John Q Trojanowski, and John T Povlishock, 1999, "The role of calpain-mediated spectrin proteolysis in traumatically induced axonal injury," *Journal of neuropathology and experimental neurology* **58**, 365–375

Chen, Shangyu, Qiankun Shi, Shuyun Zheng, Liangshen Luo, Shoutao Yuan, Xiang Wang, Zihao Cheng, and Wenhao Zhang, 2016, "Role of α-ii-spectrin breakdown products in the prediction of the severity and clinical outcome of acute traumatic brain injury," *Experimental and therapeutic medicine* **11**, 2049–2053

Chetta, Joshua, Cecilia Kye, and Sameer B Shah, 2010, "Cytoskeletal dynamics in response to tensile loading of mammalian axons," *Cytoskeleton* **67**, 650–665

Christensen, Richard, 1982, *Theory of viscoelasticity: an introduction* (Academic Press Inc., New York) ISBN 0-12-174252-0

Cong, J, DE Goll, AM Peterson, and HP Kapprell, 1989, "The role of autolysis in activity of the ca2+-dependent proteinases (mu-calpain and m-calpain).." *Journal of Biological Chemistry* **264**, 10096–10103

Corrigan, Frances, Alina Arulsamy, Jason Teng, and Lyndsey E Collins-Praino, 2017, "Pumping the brakes: neurotrophic factors for the prevention of cognitive impairment and dementia after traumatic brain injury," *Journal of neurotrauma* **34**, 971–986

Cross, Donna J, Gregory G Garwin, Marcella M Cline, Todd L Richards, Vasily Yarnykh, Pierre D Mourad, Rodney JY Ho, and Satoshi Minoshima, 2015, "Paclitaxel improves outcome from traumatic brain injury," *Brain research* **1618**, 299–308

Cullen, D Kacy, and Michelle C LaPlaca, 2006, "Neuronal response to high rate shear deformation depends on heterogeneity of the local strain field," *Journal of neurotrauma* **23**, 1304–1319

Curcio, Michele, Ivan L Salazar, Miranda Mele, Lorella MT Canzoniero, and Carlos B Duarte, 2016, "Calpains and neuronal damage in the ischemic brain: the swiss knife in synaptic injury," *Progress in neurobiology* **143**, 1–35

Czogalla, A, and AF Sikorski, 2005, "Spectrin and calpain: a 'target'and a 'sniper'in the pathology of neuronal cells," *Cellular and Molecular Life Sciences* **62**, 1913–1924

Dehmelt, Leif, and Shelley Halpain, 2005, "The map2/tau family of microtubule-associated proteins," *Genome biology* **6**, 204

Donnelly, BR, and J Medige, 1997, "Shear properties of human brain tissue," *Journal of biomechanical engineering* **119**, 423–432

Dutt, Previn, JC Simon Arthur, Pawel Grochulski, Miroslaw Cygler, *et al.*, 2000, "Roles of individual ef-hands in the activation of m-calpain by calcium," *Biochemical journal* **348**, 37–43

Duvernoy, HM, 1999, *The human brain. Surface, three-dimensional sectional anatomy with MRI, and blood supply* (Springer-Verlag Wein, New York)

Elkin, Benjamin S, and Barclay Morrison III, 2007, "Region-specific tolerance criteria for the living brain," *Stapp car crash journal* **51**, 127

Engmann, Olivia, and K Peter Giese, 2011, "Resolving the p25 controversy in alzheimer's disease," *Cognitive Sciences* **6**, 1

Falcke, Martin, 2004, "Reading the patterns in living cells—the physics of Ca^{2+} signaling," *Advances In Physics* **53**, 255–440

Farkas, O, B Polgar, J Szekeres-Bartho, T Doczi, JT Povlishock, and A Büki, 2005, "Spectrin breakdown products in the cerebrospinal fluid in severe head injury–preliminary observations," *Acta neurochirurgica* **147**, 855–861

Farkas, Orsolya, Jonathan Lifshitz, and John T Povlishock, 2006, "Mechanoporation induced by diffuse traumatic brain injury: an irreversible or reversible response to injury?." *Journal of Neuroscience* **26**, 3130–3140

Faul, M, L Xu, MM Wald, and VG Coronado, 2010, "Traumatic brain injury in the united states: emergency department visits, hospitalizations, and deaths 2002–2006," *National Center for Injury Prevention and Control*, 2002–2006

Feng, Ye, Yiyuan Xia, Guang Yu, Xiji Shu, Haoliang Ge, Kuan Zeng, Jianzhi Wang, and Xiaochuan Wang, 2013, "Cleavage of gsk-3β by calpain counteracts the inhibitory effect of ser9 phosphorylation on gsk-3β activity induced by h2o2," *Journal of neurochemistry* **126**, 234–242

Ferreira, Adriana, and Eileen H Bigio, 2011, "Calpain-mediated tau cleavage: a mechanism leading to neurodegeneration shared by multiple tauopathies," *Molecular Medicine* **17**, 676

Frangié, Carlos, Wenhui Zhang, Joëlle Perez, Yi-Chun Xu Dubois, Jean-Philippe Haymann, and Laurent Baud, 2006, "Extracellular calpains increase tubular epithelial cell mobility implications for kidney repair after ischemia," *Journal of Biological Chemistry* **281**, 26624–26632

Franklyn, Melanie, Brian Fildes, Liying Zhang, Yang King, and Laurie Sparke, 2005, "Analysis of finite element models for head injury investigation: reconstruction of four real-world impacts," *Stapp Car Crash* **49**, 1

Gaetz, Michael, 2004, "The neurophysiology of brain injury," *Clinical Neurophysiology* **115**, 4–18

Galford, James E, and James H McElhaney, 1970, "A viscoelastic study of scalp, brain, and dura," *Journal of biomechanics* **3**, 211–221

Gallo, Gianluca, 2004, "Myosin ii activity is required for severing-induced axon retraction in vitro," *Experimental neurology* **189**, 112–121

Geddes, Donna M, and Robert S Cargill, 2001, "An in vitro model of neural trauma: device characterization and calcium response to mechanical stretch," *Journal of Biomechanical Engineering* **123**, 247–255

Geddes-Klein, Donna M, Kimberly B Schiffman, and David F Meaney, 2006, "Mechanisms and consequences of neuronal stretch injury in vitro differ with the model of trauma," *Journal of Neurotrauma* **23**, 193–204

Giudice, J Sebastian, Wei Zeng, Taotao Wu, Ahmed Alshareef, Daniel F Shedd, and Matthew B Panzer, 2018, "An analytical review of the numerical methods used for finite element modeling of traumatic brain injury," *Annals of biomedical engineering*, 1–18

Giza, Christopher C, and David A Hovda, 2001, "The neurometabolic cascade of concussion," *Journal of Athletic Training* **36**, 228

Glantz, Susan B, Carol D Cianci, Rathna Iyer, Deepti Pradhan, Kevin KW Wang, and Jon S Morrow, 2007, "Sequential degradation of αii and βii spectrin by calpain in glutamate or maitotoxin-stimulated cells," *Biochemistry* **46**, 502–513

Gleichmann, Marc, and Mark P Mattson, 2011, "Neuronal calcium homeostasis and dysregulation," *Antioxidants and Redox Signaling* **14**, 1261–1273

Goll, Darrel E, Valery F Thompson, Hongqi Li, WEI Wei, and Jinyang Cong, 2003, "The calpain system," *Physiological reviews* **83**, 731–801

Gong, C-X, F Liu, I Grundke-Iqbal, and K Iqbal, 2005, "Post-translational modifications of tau protein in alzheimer's disease," *Journal of neural transmission* **112**, 813–838

Goñi-Oliver, Paloma, Jesús Avila, and Félix Hernández, 2009, "Calpain-mediated truncation of gsk-3 in post-mortem brain samples," *Journal of neuroscience research* **87**, 1156–1161

Goñi-Oliver, Paloma, Jesús Avila, and Félix Hernández, 2011, "Calpain regulates n-terminal interaction of gsk-3β with 14-3-3ζ, p53 and pkb but not with axin," *Neurochemistry international* **59**, 97–100

Goñi-Oliver, Paloma, José J Lucas, Jesús Avila, and Félix Hernández, 2007, "N-terminal cleavage of gsk-3 by calpain a new form of gsk-3 regulation," *Journal of Biological Chemistry* **282**, 22406–22413

Gururaj, G, 2013, "Epidemiology of traumatic brain injuries: Indian scenario," *Neurological research*

Harada, Kazuki, Shiro Fukuda, Manabu Kunimoto, and Ken-ichi Yoshida, 1997, "Distribution of ankyrin isoforms and their proteolysis after ischemia and reperfusion in rat brain," *Journal of neurochemistry* **69**, 371–376

Hemphill, Matthew A, Stephanie Dauth, Chung Jong Yu, Borna E Dabiri, and Kevin Kit Parker, 2015, "Traumatic brain injury and the neuronal microenvironment: a potential role for neuropathological mechanotransduction," *Neuron* **85**, 1177–1192

Hiebert, John B, Qiuhua Shen, Amanda R Thimmesch, and Janet D Pierce, 2015, "Traumatic brain injury and mitochondrial dysfunction," *The American journal of the medical sciences* **350**, 132–138

Hill, Ciaran S, Michael P Coleman, and David K Menon, 2016, "Traumatic axonal injury: mechanisms and translational opportunities," *Trends in neurosciences* **39**, 311–324

Hill, Rachel L, Indrapal N Singh, Juan A Wang, and Edward D Hall, 2017, "Time courses of post-injury mitochondrial oxidative damage and respiratory dysfunction and neuronal cytoskeletal degradation in a rat model of focal traumatic brain injury," *Neurochemistry international* **111**, 45–56

Iqbal, Khalid, Fei Liu, and Cheng-Xin Gong, 2016, "Tau and neurodegenerative disease: the story so far," *Nature Reviews Neurology* **12**, 15

Iqbal, Khalid, Fei Liu, Cheng-Xin Gong, Alejandra del C Alonso, and Inge Grundke-Iqbal, 2009, "Mechanisms of tau-induced neurodegeneration," *Acta neuropathologica* **118**, 53–69

Jin, Nana, Xiaomin Yin, Dian Yu, Maohong Cao, Cheng-Xin Gong, Khalid Iqbal, Fei Ding, Xiaosong Gu, and Fei Liu, 2015, "Truncation and activation of gsk-3β by calpain i: a molecular mechanism links to tau hyperphosphorylation in alzheimer's disease," *Scientific reports* **5**, 8187

Jog, Chandrashekhar S, 2015, *Continuum mechanics*, Vol. 1 (Cambridge University Press, Delhi, India) ISBN 978-1-107-09135-1

Kampfl, A, R Posmantur, R Nixon, F Grynspan, X Zhao, SJ Liu, JK Newcomb, GL Clifton, and RL Hayes, 1996, "μ-calpain activation and calpain-mediated cytoskeletal proteolysis following traumatic brain injury," *Journal of neurochemistry* **67**, 1575–1583

Kang, HoSung, Remy Willinger, Baye M Diaw, and Bryan Chinn, 1997, *Validation of a 3D anatomic human head model and replication of head impact in motorcycle accident by finite element modeling*, Tech. Rep. (SAE Technical Paper)

Kass, IS, and PETER Lipton, 1986, "Calcium and long-term transmission damage following anoxia in dentate gyrus and ca1 regions of the rat hippocampal slice.." *The Journal of Physiology* **378**, 313–334

Khorchid, Ahmad, and Mitsuhiko Ikura, 2002, "How calpain is activated by calcium," *Nature Structural and Molecular Biology* **9**, 239

Kilinc, Devrim, 2008, *Mechanisms and Prevention of Axonal Damage in Response to Mechanical Trauma to Cultured Neurons*, Ph.D. thesis (Drexel University)

Kimura, Taeko, Koichi Ishiguro, and Shin-ichi Hisanaga, 2014, "Physiological and pathological phosphorylation of tau by cdk5," *Frontiers in molecular neuroscience* **7**, 65

Kloda, Anna, Linda Lua, Rhonda Hall, David J Adams, and Boris Martinac, 2007, "Liposome reconstitution and modulation of recombinant n-methyl-d-aspartate receptor channels by membrane stretch," *Proceedings of the National Academy of Sciences* **104**, 1540–1545

Kobeissy, Firas H, Ming Cheng Liu, Zhihui Yang, Zhiqun Zhang, Wenrong Zheng, Olena Glushakova, Stefania Mondello, John Anagli, Ronald L Hayes, and Kevin KW Wang, 2015, "Degradation of βii-spectrin protein by calpain-2 and caspase-3 under neurotoxic and traumatic brain injury conditions," *Molecular neurobiology* **52**, 696–709

Köpke, E, Yunn-Chyn Tung, Sadia Shaikh, A del C Alonso, Khalid Iqbal, and I Grundke-Iqbal, 1993, "Microtubule-associated protein tau. abnormal phosphorylation of a non-paired helical filament pool in alzheimer disease.." *Journal of Biological Chemistry* **268**, 24374–24384

Kowalewski, Jacob M, Per Uhlén, Hiroaki Kitano, and Hjalmar Brismar, 2006, "Modeling the impact of store-operated Ca^{2+} entry on intracellular ca 2+ oscillations," *Mathematical Biosciences* **204**, 232–249

Kristián, Tibor, and Bo K Siesjö, 1998, "Calcium in ischemic cell death," *Stroke* **29**, 705–718

Ksiezak-Reding, Hanna, Wan-Kyng Liu, and Shu-Hui Yen, 1992, "Phosphate analysis and dephosphorylation of modified tau associated with paired helical filaments," *Brain research* **597**, 209–219

Kulbe, Jacqueline R, and Edward D Hall, 2017, "Chronic traumatic encephalopathy-integration of canonical traumatic brain injury secondary injury mechanisms with tau pathology," *Progress in neurobiology*

Kurbatskaya, Ksenia, Emma C Phillips, Cara L Croft, Giacomo Dentoni, Martina M Hughes, Matthew A Wade, Safa Al-Sarraj, Claire Troakes, Michael J O'Neill, Beatriz G Perez-Nievas, *et al.*, 2016, "Upregulation of calpain activity precedes tau phosphorylation and loss of synaptic proteins in alzheimer's disease brain," *Acta neuropathologica communications* **4**, 34

Kusakawa, Gen-ichi, Taro Saito, Reiko Onuki, Koichi Ishiguro, Takeo Kishimoto, and Shin-ichi Hisanaga, 2000, "Calpain-dependent proteolytic cleavage of the p35 cdk5 activator to p25," *Journal of Biological Chemistry*

LaPlaca, Michelle C, Virginia M-Y Lee, and Lawrence E Thibault, 1997, "An in vitro model of traumatic neuronal injury: loading rate-dependent changes in acute cytosolic calcium and lactate dehydrogenase release," *Journal of Neurotrauma* **14**, 355–368

Lee, Ming-sum, Young T Kwon, Mingwei Li, Junmin Peng, Robert M Friedlander, and Li-Huei Tsai, 2000, "Neurotoxicity induces cleavage of p35 to p25 by calpain," *Nature* **405**, 360

Levchakov, Anna, Eran Linder-Ganz, Ramesh Raghupathi, Susan S Margulies, and Amit Gefen, 2006, "Computational studies of strain exposures in neonate and mature rat brains during closed head impact," *Journal of Neurotrauma* **23**, 1570–1580

Lifshitz, Jonathan, Patrick G Sullivan, David A Hovda, Tadeusz Wieloch, and Tracy K McIntosh, 2004, "Mitochondrial damage and dysfunction in traumatic brain injury," *Mitochondrion* **4**, 705–713

Limpert, Eckhard, Werner A Stahel, and Markus Abbt, 2001, "Log-normal distributions across the sciences: Keys and clues: On the charms of statistics, and how mechanical models resembling gambling machines offer a link to a handy way to characterize log-normal distributions, which can provide deeper insight into variability and probability—normal or log-normal: That is the question," *AIBS Bulletin* **51**, 341–352

Liu, Fei, Inge Grundke-Iqbal, Khalid Iqbal, and Cheng-Xin Gong, 2005, "Contributions of protein phosphatases pp1, pp2a, pp2b and pp5 to the regulation of tau phosphorylation," *European Journal of Neuroscience* **22**, 1942–1950

Liu, Fei, Zhihou Liang, Jianhua Shi, Dongmei Yin, Ezzat El-Akkad, Inge Grundke-Iqbal, Khalid Iqbal, and Cheng-Xin Gong, 2006, "Pka modulates gsk-3β-and cdk5-catalyzed phosphorylation of tau in site-and kinase-specific manners," *FEBS letters* **580**, 6269–6274

Liu, Shi Jie, Jia Yu Zhang, Hong Lian Li, Zheng Yu Fang, Qun Wang, Heng Mei Deng, Cheng Xin Gong, Inge Grundke-Iqbal, Khalid Iqbal, and Jian Zhi Wang, 2004, "Tau becomes a more favorable substrate for gsk-3 when it is prephosphorylated by pka in rat brain," *Journal of Biological Chemistry* **279**, 50078–50088

Lu, Wennan, Farraj Albalawi, Jonathan M Beckel, Jason C Lim, Alan M Laties, and Claire H Mitchell, 2017, "The p2x7 receptor links mechanical strain to cytokine il-6 up-regulation and release in neurons and astrocytes," *Journal of neurochemistry* **141**, 436–448

Lusardi, Theresa A, Jeff Rangan, David Sun, Douglas H Smith, and David F Meaney, 2004, "A device to study the initiation and propagation of calcium transients in cultured neurons after mechanical stretch," *Annals of Biomedical Engineering* **32**, 1546–1559

Lytton, Jonathan, Marisa Westlin, Scott E Burk, Gary E Shull, and David H MacLennan, 1992, "Functional comparisons between isoforms of the sarcoplasmic or endoplasmic reticulum family of calcium pumps.." *Journal of Biological Chemistry* **267**, 14483–14489

Ma, Shanshan, Shaojun Liu, Qiaoying Huang, Bo Xie, Bingquan Lai, Chong Wang, Bin Song, and Mingtao Li, 2012, "Site-specific phosphorylation protects gsk-3β from calpain-mediated truncation of its n-and c-termini," *Journal of Biological Chemistry*, jbc–M111

Madhukar, Amit, and Martin Ostoja-Starzewski, 2019, "Finite element methods in human head impact simulations: a review," *Annals of biomedical engineering*, 1–23

Maneshi, Mohammad Mehdi, Bruce Maki, Radhakrishnan Gnanasambandam, Sophie Belin, Gabriela K Popescu, Frederick Sachs, and Susan Z Hua, 2017, "Mechanical stress activates nmda receptors in the absence of agonists," *Scientific reports* **7**, 39610

Maneshi, Mohammad Mehdi, Frederick Sachs, and Susan Z Hua, 2015, "A threshold shear force for calcium influx in an astrocyte model of traumatic brain injury," *J. Neurotrauma* **32**, 1020–1029

Mao, Haojie, Liying Zhang, King H Yang, and Albert I King, 2006, "Application of a finite element model of the brain to study traumatic brain injury mechanisms in the rat," *Stapp Car Crash* **50**, 583

Margulies, Susan Sheps, and Lawrence E Thibault, 1992, "A proposed tolerance criterion for diffuse axonal injury in man," *Journal of biomechanics* **25**, 917–923

Maxwell, William L, Aisha Domleo, Gillian McColl, Saeed S Jafari, and David I Graham, 2003, "Post-acute alterations in the axonal cytoskeleton after traumatic axonal injury," *Journal of neurotrauma* **20**, 151–168

McKee, Ann C, Robert C Cantu, Christopher J Nowinski, E Tessa Hedley-Whyte, Brandon E Gavett, Andrew E Budson, Veronica E Santini, Hyo-Soon Lee, Caroline A Kubilus, and Robert A Stern, 2009, "Chronic traumatic encephalopathy in athletes: progressive tauopathy after repetitive head injury," *Journal of Neuropathology & Experimental Neurology* **68**, 709–735

Meaney, David F, and Douglas H Smith, 2011, "Biomechanics of concussion," *Clin Sports Med* **30**, 19–31

Mendis, KK, RL Stalnaker, and SH Advani, 1995, "A constitutive relationship for large deformation finite element modeling of brain tissue," *Journal of Biomechanical Engineering* **117**, 279–285

Miller, Karol, and Kiyoyuki Chinzei, 1997, "Constitutive modelling of brain tissue: experiment and theory," *Journal of biomechanics* **30**, 1115–1121

Moldoveanu, Tudor, Christopher M Hosfield, Daniel Lim, John S Elce, Zongchao Jia, and Peter L Davies, 2002, "A Ca^{2+} switch aligns the active site of calpain," *Cell* **108**, 649–660

Moldoveanu, Tudor, Zongchao Jia, and Peter L Davies, 2004, "Calpain activation by cooperative Ca^{2+} binding at two non-ef-hand sites," *Journal of Biological Chemistry* **279**, 6106–6114

Morrison III, Barclay, Heather L Cater, Christopher CB Wang, Fay C Thomas, *et al.*, 2003, "A tissue level tolerance criterion for living brain developed with an in vitro model of traumatic mechanical loading," *Stapp Car Crash Journal* **47**, 93

Myburgh, John A, D James Cooper, Simon R Finfer, Balasubramanian Venkatesh, Daryl Jones, Alisa Higgins, Nicole Bishop, Tracey Higlett, Australasian Traumatic Brain Injury Study (ATBIS) Investigators for the Australian, *et al.*, 2008, "Epidemiology and 12-month outcomes from traumatic brain injury in australia and new zealand," *Journal of Trauma and Acute Care Surgery* **64**, 854–862

Namjoshi, Dhananjay R, Craig Good, Wai Hang Cheng, William Panenka, Darrin Richards, Peter A Cripton, and Cheryl L Wellington, 2013, "Towards clinical management of traumatic brain injury: a review of models and mechanisms from a biomechanical perspective," *Dis Model Mech* **6**, 1325–1338

Nath, Rathna, Megan Davis, Albert W Probert, Nancy C Kupina, Xiaodong Ren, Gerald P Schielke, and Kevin KW Wang, 2000, "Processing of cdk5 activator p35 to its truncated form (p25) by calpain in acutely injured neuronal cells," *Biochemical and biophysical research communications* **274**, 16–21

Nilsson, P, L Hillered, Y Olsson, MJ Sheardown, and AJ Hansen, 1993, "Regional changes in interstitial k+ and ca2+ levels following cortical compression contusion trauma in rats," *Journal of Cerebral Blood Flow & Metabolism* **13**, 183–192

Nusholtz, Guy S, Paula Lux, Patricia Kaiker, and Miles A Janicki, 1984, *Head impact response—Skull deformation and angular accelerations*, Tech. Rep. (SAE Technical Paper)

Ommaya, Ayub K, and TA Gennarelli, 1974, "Cerebral concussion and traumatic unconsciousness: correlation of experimental and clinical observations on blunt head injuries," *Brain* **97**, 633–654

Ono, Yasuko, and Hiroyuki Sorimachi, 2012, "Calpains—an elaborate proteolytic system," *Biochimica et Biophysica Acta (BBA)-Proteins and Proteomics* **1824**, 224–236

Palecek, Sean P, Alan F Horwitz, and Douglas A Lauffenburger, 1999, "Kinetic model for integrin-mediated adhesion release during cell migration," *Annals of biomedical engineering* **27**, 219–235

Palmer, Alan M, Donald W Marion, Michelle L Botscheller, David M Bowen, and Steven T DeKosky, 1994, "Increased transmitter amino acid concentration in human ventricular csf after brain trauma.." *Neuroreport* **6**, 153–156

Patrick, Gentry N, Lawrence Zukerberg, Margareta Nikolic, Suzanne de La Monte, Pieter Dikkes, and Li-Huei Tsai, 1999, "Conversion of p35 to p25 deregulates cdk5 activity and promotes neurodegeneration," *Nature* **402**, 615

Pena, A, JD Pickard, D Stiller, NG Harris, and MU Schuhmann, 2005, "Brain tissue biomechanics in cortical contusion injury: a finite element analysis," in *Intracranial Pressure and Brain Monitoring XII* (Springer) pp. 333–336

Peter, Stephen J, and Mohammad RK Mofrad, 2012, "Computational modeling of axonal microtubule bundles under tension," *Biophysical journal* **102**, 749–757

Pike, Brian R, Jeremy Flint, Satavisha Dutta, Erik Johnson, Kevin KW Wang, and Ronald L Hayes, 2001, "Accumulation of non-erythroid αii-spectrin and calpain-cleaved αii-spectrin breakdown products in cerebrospinal fluid after traumatic brain injury in rats," *Journal of neurochemistry* **78**, 1297–1306

Pike, BRIAN R, XIURONG ZHAO, JENNIFER K NEWCOMB, CHRISTOPHER C GLENN, DOUGLAS K ANDERSON, and RONALD L HAYES, 2000, "Stretch injury causes calpain and caspase-3 activation and necrotic and apoptotic cell death in septo-hippocampal cell cultures," *Journal of neurotrauma* **17**, 283–298

Pineda, Jose A, Stephen B Lewis, Alex B Valadka, Linda Papa, H Julia Hannay, Shelley C Heaton, Jason A Demery, Ming Cheng Liu, Jada M Aikman, Veronica Akle, *et al.*, 2007, "Clinical significance of α ii-spectrin breakdown products in cerebrospinal fluid after severe traumatic brain injury," *Journal of neurotrauma* **24**, 354–366

Prange, Michael T, and Susan S Margulies, 2002, "Regional, directional, and age-dependent properties of the brain undergoing large deformation," *Journal of biomechanical engineering* **124**, 244–252

Prins, Mayumi, Tiffany Greco, Daya Alexander, and Christopher C Giza, 2013, "The pathophysiology of traumatic brain injury at a glance," *Disease Models & Mechanisms* **6**, 1307–1315

Rashid, Badar, Michel Destrade, and Michael D Gilchrist, 2013, "Mechanical characterization of brain tissue in simple shear at dynamic strain rates," *Journal of the mechanical behavior of biomedical materials* **28**, 71–85

Reeves, Thomas M, John E Greer, Andrew S Vanderveer, and Linda L Phillips, 2010, "Proteolysis of submembrane cytoskeletal proteins ankyrin-g and αii-spectrin following diffuse brain injury: A role in white matter vulnerability at nodes of ranvier," *Brain Pathology* **20**, 1055–1068

Rohatgi, Ankit, 2018, "Webplotdigitizer," https://automeris.io/WebPlotDigitizer

Roozenbeek, Bob, Andrew IR Maas, and David K Menon, 2013, "Changing patterns in the epidemiology of traumatic brain injury," *Nat. Rev. Neurol.* **9**, 231–236

Rowson, Steven, Stefan M Duma, Jonathan G Beckwith, Jeffrey J Chu, Richard M Greenwald, Joseph J Crisco, P Gunnar Brolinson, Ann-Christine Duhaime, Thomas W McAllister, and Arthur C Maerlender, 2012, "Rotational head kinematics in football impacts: an injury risk function for concussion," *Annals of biomedical engineering* **40**, 1–13

Rzigalinski, BA, JT Weber, KA Willoughby, and EF Ellis, 1998, "Intracellular free calcium dynamics in stretch-injured astrocytes," *Journal of neurochemistry* **70**, 2377–2385

Rzigalinski, Beverly A, Shi Liang, Jerry S McKinney, Karen A Willoughby, and Earl F Ellis, 1997, "Effect of ca2+ on in vitro astrocyte injury," *Journal of neurochemistry* **68**, 289–296

Sendek, Austin, Henry R Fuller, N Robert Hayre, Rajiv RP Singh, and Daniel L Cox, 2014, "Simulated cytoskeletal collapse via tau degradation," *PloS one* **9**, e104965

Serbest, Gulyeter, Matthew F Burkhardt, Robert Siman, Ramesh Raghupathi, and Kathryn E Saatman, 2007, "Temporal profiles of cytoskeletal protein loss following traumatic axonal injury in mice," *Neurochemical research* **32**, 2006–2014

Shuck, LZ, and SH Advani, 1972, "Rheological response of human brain tissue in shear," *Journal of basic engineering* **94**, 905–911

Siedler, Declan G, Meng Inn Chuah, Matthew TK Kirkcaldie, James C Vickers, and Anna E King, 2014, "Diffuse axonal injury in brain trauma: insights from alterations in neurofilaments," *Frontiers in cellular neuroscience* **8**, 429

Slepchenko, Boris M, James C Schaff, John H Carson, and Leslie M Loew, 2002, "Computational cell biology: spatiotemporal simulation of cellular events," *Annual Review of Biophysics and Biomolecular Structures* **31**, 423–441

Smith, Douglas H, and David F Meaney, 2000, "Axonal damage in traumatic brain injury," *The neuroscientist* **6**, 483–495

Sneyd, J, J Keizer, and MJ Sanderson, 1995, "Mechanisms of calcium oscillations and waves: a quantitative analysis.." *The FASEB Journal* **9**, 1463–1472

Stepanov, Alexander, Tatiana Karelina, Nikolai Markevich, Oleg Demin, and Timothy Nicholas, 2018, "A mathematical model of multisite phosphorylation of tau protein," *PloS one* **13**, e0192519

Suzuki, Koichi, Shoji Hata, Yukiko Kawabata, and Hiroyuki Sorimachi, 2004, "Structure, activation, and biology of calpain," *Diabetes* **53**, S12–S18

Takhounts, Erik G, Rolf H Eppinger, J Quinn Campbell, Rabih E Tannous, *et al.*, 2003, "On the development of the simon finite element head model," *Stapp Car C* **47**, 107

Takhounts, Erik G, Stephen A Ridella, Vikas Hasija, Rabih E Tannous, J Quinn Campbell, Dan Malone, Kerry Danelson, Joel Stitzel, Steve Rowson, and Stefan Duma, 2008, "Investigation of traumatic brain injuries using the next generation of simulated injury monitor (simon) finite element head model," *Stapp Car C* **52**, 1

Tang-Schomer, Min D, Victoria E Johnson, Peter W Baas, William Stewart, and Douglas H Smith, 2012, "Partial interruption of axonal transport due to microtubule breakage accounts for the formation of periodic varicosities after traumatic axonal injury," *Experimental neurology* **233**, 364–372

Tang-Schomer, Min D, Ankur R Patel, Peter W Baas, and Douglas H Smith, 2010, "Mechanical breaking of microtubules in axons during dynamic stretch injury underlies delayed elasticity, microtubule disassembly, and axon degeneration," *The FASEB Journal* **24**, 1401–1410

Wang, Jian-zhi, Qiongli Wu, Alan Smith, Inge Grundke-Iqbal, and Khalid Iqbal, 1998, "τ is phosphorylated by gsk-3 at several sites found in alzheimer disease and its biological activity markedly inhibited only after it is prephosphorylated by a-kinase," *FEBS letters* **436**, 28–34

Weber, John T, 2004, "Calcium homeostasis following traumatic neuronal injury," *Current Neurovascular Research* **1**, 151–171

Weber, John Thomas, 2012, "Altered calcium signaling following traumatic brain injury," *Frontiers in Pharmacology* **3**, 60

Werner, C, and K Engelhard, 2007, "Pathophysiology of traumatic brain injury," *British Journal of Anaesthesia* **99**, 4–9

Williams, Philip R, Bogdan-Nicolae Marincu, Catherine D Sorbara, Christoph F Mahler, Adrian-Minh Schumacher, Oliver Griesbeck, Martin Kerschensteiner, and Thomas Misgeld, 2014, "A recoverable state of axon injury persists for hours after spinal cord contusion in vivo," *Nature Communications* **5**

Wojda, Urszula, Elzbieta Salinska, and Jacek Kuznicki, 2008, "Calcium ions in neuronal degeneration," *IUBMB Life* **60**, 575–590

Wolf, John A, Peter K Stys, Theresa Lusardi, David Meaney, and Douglas H Smith, 2001, "Traumatic axonal injury induces calcium influx modulated by tetrodotoxin-sensitive sodium channels," *Journal of Neuroscience* **21**, 1923–1930

Woodcock, Thomas, and Cristina Morganti-Kossmann, 2013, "The role of markers of inflammation in traumatic brain injury," *Frontiers in neurology* **4**, 18

Yamada, Ryuji X, Takuya Sasaki, Junya Ichikawa, Ryuta Koyama, Norio Matsuki, and Yuji Ikegaya, 2008, "Long-range axonal calcium sweep induces axon retraction," *Journal of Neuroscience* **28**, 4613–4618

Yang, W-J, W Chen, L Chen, Y-J Guo, J-S Zeng, G-Y Li, and W-S Tong, 2017, "Involvement of tau phosphorylation in traumatic brain injury patients," *Acta Neurologica Scandinavica* **135**, 622–627

Zhang, Liying, King H Yang, Ramesh Dwarampudi, Kiyoshi Omori, Tieliang Li, Kun Chang, Warren N Hardy, Tom B Khalil, and Albert I King, 2001, "Recent advances in brain injury research: a new human head model development and validation," *Stapp Car Crash* **45**, 369–394

Zhang, Liying, King H Yang, and Albert I King, 2004, "A proposed injury threshold for mild traumatic brain injury," *Joournal of Biomechanical Engineering* **126**, 226–236

Zhao, Xiurong, Rand Posmantur, Andreas Kampfl, Shi-Jie Liu, Kevin KW Wang, Jennifer K Newcomb, Brian R Pike, Guy L Clifton, and Ronald L Hayes, 1998, "Subcellular localization and duration of μ-calpain and m-calpain activity after traumatic brain injury in the rat: a casein zymography study," *Journal of Cerebral Blood Flow & Metabolism* **18**, 161–167

Zheng, James Q, and Mu-ming Poo, 2007, "Calcium signaling in neuronal motility," *Annu. Rev. Cell Dev. Biol.* **23**, 375–404

Zink, Brian J, 2001, "Traumatic brain injury outcome: concepts for emergency care," *Annals of emergency medicine* **37**, 318–332